TARGETED DELIVERY OF A-MANGOSTIN TO PROSTATE CANCER CELLS UTILIZING RECONSTITUTED HIGH-DENSITY LIPOPROTEIN NANOPARTICLES

THESIS

Presented to the Council of the

School of Biomedical Sciences

University of North Texas

Health and Science Center at Fort Worth

In Partial Fulfillment of the Requirements

For the Degree of

MASTER OF SCIENCE

By

Ammar Kapic, B.S.

Fort Worth, Texas

June 2022

Acknowledgments

This project is my most remarkable undertaking thus far. I was pleased to work with many individuals in different fields who supported and guided my project. I want to give a special thanks to my mentor Dr. Rafal Fudala for pushing me to reach my full potential and (especially) for his patience. He exposed me to the importance of discussion and the nuances in communication that can make or break a scientist. I will always carry these lessons with me and am thankful for our shared experiences.

I thank my committee members, Dr. Riyaz Basha and Dr. Amalendu Ranjan, for lending their expertise. Additionally, I would like to thank my university member, Dr. Raghu Krishnamoorthy, for his comments and genuine interest in the project. Our discussions during the committee meetings helped me fill in the gaps in my knowledge and focus on this project.

A large portion of my project was made possible because of the assistance and advice I received from my lab members. First, I would like to thank Dr. Nirupama Sabnis for her deep knowledge and experience with the rHDL. Next, I want to thank my colleagues Akpedje Serena Dossou and Roland Max Petty for our daily discussions, training, and advice and for being great friends. The lab truly felt like my home away from home. Next, I thank my collaborators from Texas Christian University (TCU), who lent their expertise to this project. Then, I want to thank Luca Ceresa and Jose Chavez from the lab of Dr. Karol Gryczynski for helping us acquire the fluorescence lifetime data. Additionally from TCU, I would like to thank Will Burnett from the lab of Dr. Jeff Coffer for imaging our rHDL nanoparticle samples. Finally, I would like to thank my parents, my brother, and my fiancée Alma for their wisdom and emotional (and sometimes financial) support. They helped me through my most difficult times and gave me the confidence to reach my goals.

Table of Contents

List of Tables

List of Illustrations

Chapter 1

Introduction

1.1. Prostate Cancer

1.1.1. Epidemiology of Prostate Cancer

In 1853, Dr. John Adams's reported that an asymmetrical growth was found on the prostate of a fifty-nine-year-old male during an autopsy. The individual previously suffered from difficulties urinating and had an enlarged prostate. After death, there were signs of metastasis in the surrounding bone and lymph nodes, suggesting that the tumor contributed to the individual's death (Copland, 1853). This report was the first official description of prostate cancer (PCa), considered a rare disease at the time. Over 170 years later, however, PCa has become the second most common cancer and the second leading cause of cancer-related death in men in the United States (CDC, 2020). In the United States, over 250,000 men will be diagnosed with PCa, nearly 34,000 succumbing to the disease in 2022 alone (ACS, 2022b). Age is a primary risk factor for PCa development. Those above the age of 65 are considered high-risk, with nearly 60% of cases PCa diagnosed in individuals older than 65 (ACS, 2022b). However, not all racial/ethnic groups are affected equally. Non-Hispanic African Americans are more likely to develop aggressive variants than other racial groups (Figure 1 (Deka et al., 2020; Taitt, 2018). Studies suggest this health disparity could be due to genetic predisposition in those of African descent and limited access to healthcare (Rapiti et al., 2009; Yadav et al., 2020). Annual screenings for PCa are recommended after 40 using physical examinations and blood Prostate Specific Antigen (PSA) measurements.

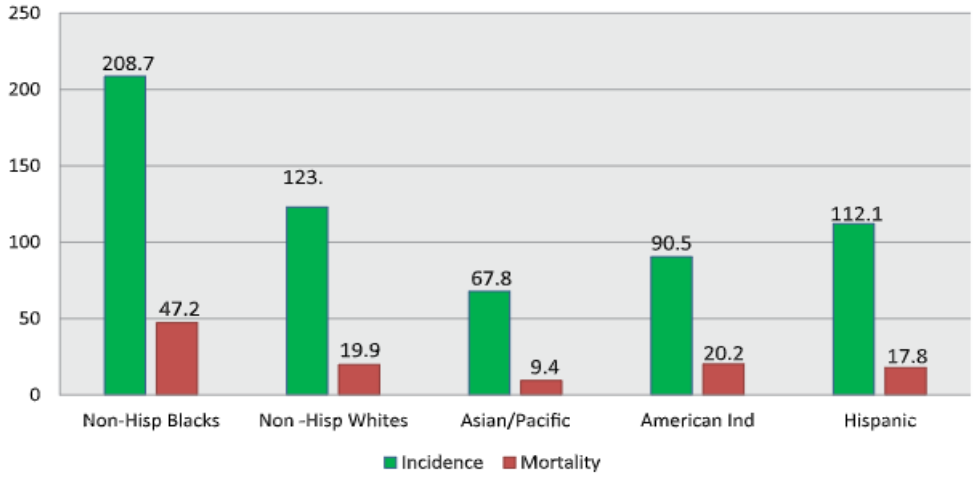

Figure 1. *Incidence and Mortality statistics of prostate cancer between racial groups in the United States per 100,000 individuals (Taitt 2018).*

However, there may be reduced access to these facilities in regions of lower socioeconomic development, resulting in undiagnosed individuals developing more aggressive variants, as summarized in Figure 1 (Cai et al., 2020). The other significant risk of PCa is often associated with high-fat diets; however, there is difficulty distinguishing if these effects are due to the consumption of dietary fats or due to obesity itself. Studies have shown that the intake of certain types of fats, such as cholesterol and saturated fats, may contribute to the risk of the disease, as shown in both observational studies and mouse models (Di Sebastiano & Mourtzakis, 2014; Pelser et al., 2013). In addition, there is a correlation between obesity and the aggressiveness of the PCa, suggesting that lifestyle plays some role in PCa development (Freedland & Aronson, 2004). Finally, false positives are common due to the limitations of current screening methods, which will be discussed in later sections that can further complicate the incidence and mortality for PCa patients. With an increasingly older population and rising rates of obesity, it is projected that rates of PCa incidence will continue to rise globally (Cai et al., 2020; Weir et al., 2021). Countries with higher socioeconomic development are expected to have higher incidence rates due to lifestyle and more access to screening. The economic burden on global healthcare will, in turn, continue to rise. The average patient cost has tripled to an estimated $33,000 since 2006. However, patients with

higher-grade cancers had significantly higher costs nearing $200,000 (Gustavsen et al., 2020; Roehrborn & Black, 2011). Thus, PCa is a significant growing issue requiring cost-effective screening and treatments. However, the current treatments discussed in later chapters fall short of providing effective treatments for patients and, in some cases, may further exacerbate PCa progression producing more malignant variants. Furthermore, patients may experience significant reductions in their overall quality of life. Therefore, new personalized therapies are needed to reduce the mortality of later-stage variants of PCa.

1.1.2. The Prostate

The prostate is often described as a walnut-sized organ found beneath the bladder. It produces prostate-specific antigen (PSA), zinc, and citrate, three components of semen. These secretions protect and nurture the sperm cells as they journey to an unfertilized egg. The prostate is a glandular tissue comprised of 2 significant lobes and several distinct zones, including the central (CZ), transition (TZ), and peripheral zones (PZ), each with a distinct function, as shown in Figure 2 (Cohen et al., 2008). The CZ contains the ejaculatory ducts. Rarely are incidences of PCa reported within this region, possibly due to the lower glandular tissue content. The TZ is a small region comprised primarily of glandular tissue. Finally, the PZ is the largest region of glandular tissue that encapsulates both the TZ and CZ, making up the bulk of the prostate's total mass. These zones are separated by a fibrous layer of tissue creating structural domains for the prostate (Raymond, 2013). Finally, a fibromuscular component sits on the top of the prostate, providing the mechanical force required to eject the prostate secretions into the urethra (Oh WK, 2003). Most prostate cancers emerge within the PZ region. However, they have been reported to a lesser extent in the TZ and very rarely in the CZ (Cohen et al., 2008) (Figure 2).

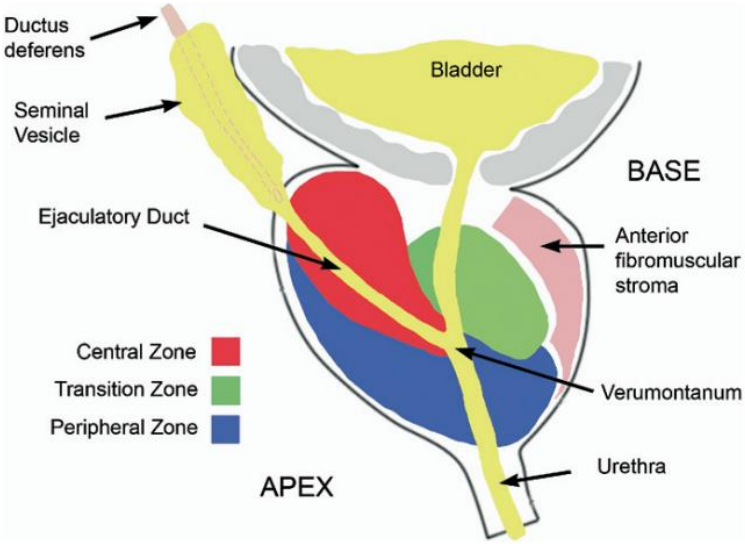

Figure 2. *Anatomy of the prostate (Cohen et al., 2008).*

Development of the prostate initially ends when an individual reaches sexual maturity. During puberty, the increasing levels of androgens such as testosterone cause a slow enlargement of its size (Aaron et al., 2016). These pro-growth signals are usually balanced by pro-apoptotic signals that inhibit and prevent excessive prostate enlargement, which could result in obstruction of urine leaving the bladder. However, as individuals reach the age of 40, there is an increased risk of dysregulation of the regulatory pathways causing a skew towards pro-growth. This enlargement may result in benign prostatic hyperplasia (BPH), which is non-cancerous. Paradoxically the prostate enlarges despite the reduction in systemic androgen level. By the age of 80, more than 80% of men will experience some form of prostate enlargement; however, this condition itself is not correlated with increased risk of PCa but instead may cause physical discomfort and urine retention (Chughtai et al., 2016; Young et al., 2000). However, the dysregulation of the pro-growth signals becomes a significant issue within the PZ, as most PCa emerges in this region.

1.1.3. Carcinogenesis of the Prostate

It is commonly accepted that PCa arises from prostatic intraepithelial neoplasia (PINs). PINs are a heterogeneous group, often originating from the ductal and acinar cells in the PZ. They are categorized by their histological appearance and potential for malignancy (Zhou, 2018). High-grade prostatic intraepithelial neoplasia (HGPIN) is a variant considered the highest risk for carcinogenesis. Studies have linked the emergence of HGPIN as a predictor for the eventual development of PCa. HGPIN can share some genetic mutations often associated with PCa (Adamczyk et al., 2014; Jung et al., 2016). Over time the further accumulation of genetic aberrations such as the loss of PTEN and DNA repair genes can enhance the transition of PIN towards PCa (Geybels et al., 2017; Mateo et al., 2017). The accumulation of these various mutations creates a complex web of dysregulation that eventually transition the PINs into PCa. Additional environmental effects such as exposure, diet, and genetic predisposition may contribute to developing these mutations; however, as mentioned previously, further study is required to fully extrapolate the specific effects of these factors. The stages of carcinogenesis are summarized in Figure 3.

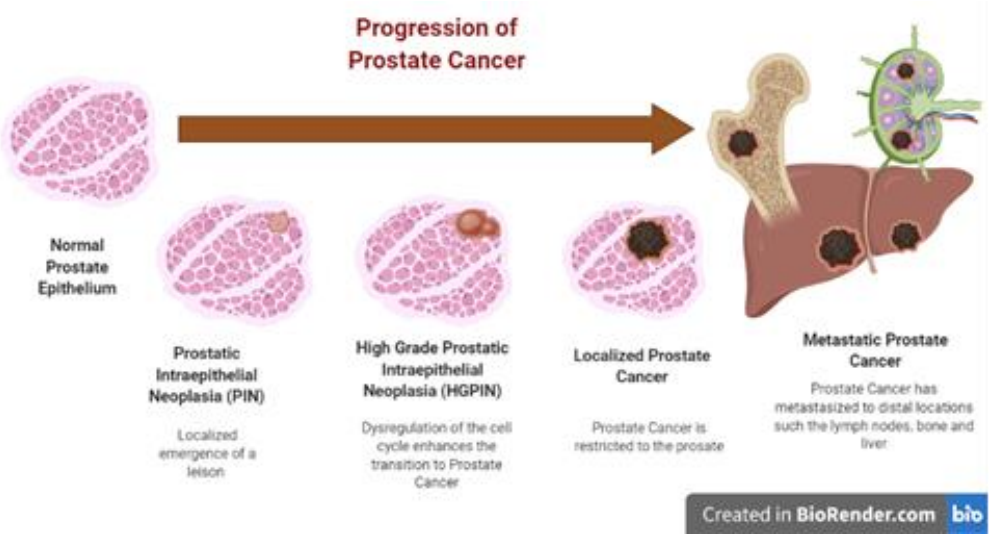

Figure 3. *Progression of prostate cancer.*

1.1.4. Androgen Receptor Axis

The most common site of dysregulation is in the androgen receptor (AR) axis. Androgens are the primary drivers for the growth of the prostate. The AR sits at the top of various signaling pathways through genomic and non-genomic functions. The AR belongs to the family of nuclear receptors composed of an N-terminal domain (NTD), ligand-binding domain (LBD), and a DNA binding domain (DBD) (Feng & He, 2019). When activated by a ligand, it dissociates from heat shock proteins, then translocated them to the nucleus to homodimerize and bind to Androgen Response Elements (ARE), initiating the transcription of pro-growth genes (Aurilio et al., 2020). The primary ligand for the activation of the AR is dihydrotestosterone (DHT) which is converted from systemic testosterone via the enzyme 5α-reductase. However, the nuclear receptor family of proteins shares many similarities in their LBD. Therefore, androgens are not the sole activators of the AR, nor is the AR exclusive to activation by androgens. Promiscuous binding of androgens to other receptors such as glucocorticoid receptors (GR) has been observed. Conversely other steroids may activate the AR. Mutations in the LBD of the AR may promote promiscuous binding with some variants enhancing the activation by other hormones and androgen blockers (Brooke et al., 2008; Duff & McEwan, 2005). The AR, when ligand-bound, can induce the activation of pathways such as the PI3K and MAPK (Ueda et al., 2002; Unni et al., 2004; Wen et al., 2000). However, in the absence of androgens, the AR can be activated independently through protein interactions. For example, AKT has been observed to phosphorylate AR, directly and indirectly, enhancing its expression (Yang et al., 2005). Figure 4 summarizes the system of maintenance and reciprocal expression that has been reported between the AR and PI3K axis. Depending on the cellular conditions, such as low androgen concentration, increased activation of mTORC1 or the AR has

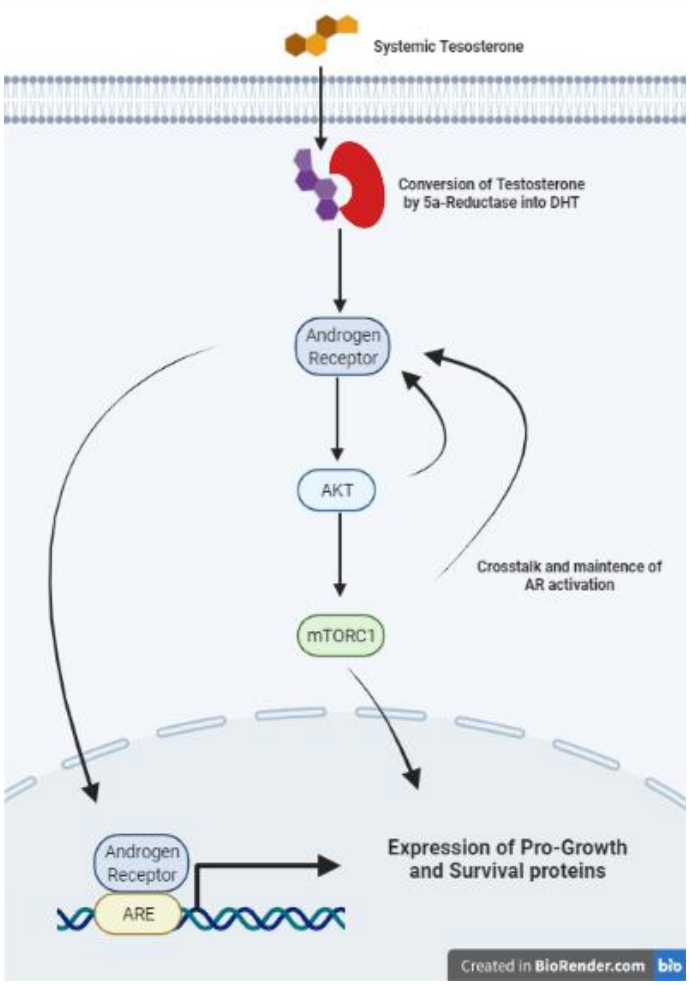

Figure 4. *Part of the Androgen Receptor axis. Crosstalk with the PI3K axis is shown.*

been observed (Wu et al., 2010). the amount of crosstalk, the AR has become the primary target for inhibition; however, AR mutants and the complex signaling crosstalk have made inhibiting the AR alone limited to temporary growth inhibition.

1.1.5. Limitations of Current Screening Techniques and Treatments

Improvements in screening techniques have increased the number of reported cases of PCa. However, false positives may lead to early treatments that can cause unnecessary intervention and worsen an individual's prognosis. Traditionally physical screenings were recommended for men over the age of 40. However, PCa screening recommendations have changed depending on family history and PSA levels (ACS, 2022a). Due to the location of the prostate, Digital Rectal

Examinations (DRE) are used by physicians to feel the prostate for asymmetry and enlargement physically. However, there is little compelling data to suggest that they are helpful for PCa detection (Naji et al., 2018). Systemic prostate-specific antigen (PSA) levels are an additional biomarker to measure PCa risk. PSA can rise with the onset of PCa and may decrease with treatment; however, these can give misleading information about a disease state (Adhyam & Gupta, 2012). Some advanced PCa has been shown to suppress levels of PSA, masking their progression during treatment (Lee et al., 2010). Furthermore, individuals with BPH often have an aberrantly shaped prostate and changes in their PSA levels, creating the risk for unnecessary intervention (Sandhu & Andriole, 2012). Age remains a barrier to modern treatments. Due to the often-slow growth of the PCa, a watch and wait approach is taken to minimize patient discomfort (Sandhu & Andriole, 2012). Patients may not be considered fit for invasive surgeries like prostatectomies; instead, hormonal therapy is often employed if deemed necessary. The current gold-standard treatment for PCa is androgen deprivation therapy (ADT) to combat the AR axis. Typically, a panel of ADT drugs is used throughout the treatment duration with higher specificity against the signaling pathway of the AR. These can target the production of systemic androgens, which effectively chemically castrates the patient, 5α-reductase, or the AR itself (Sharifi, 2005). This reduced activation of the AR theoretically reduces the growth rate of PCa; however, this procedure is not cytotoxic but rather cytostatic. In addition, ADT brings along a myriad of different side effects, including osteoporosis, metabolic disorders, and erectile dysfunction (Taylor et al., 2009). Finally, the inhibitory effect produced by ADT is only temporary as resistance and independence from systemic androgens eventually emerge.

1.1.6. Castration-Resistant Prostate Cancer

Extended periods of androgen deprivation produce a selective pressure against PCa, supporting the development of more malignant forms of PCa. Like other hormone-responsive cancers such as breast and kidney cancers, targeting these hormone-dependent signaling pathways often results in a more malignant hormone-refractory variant. Often, variants independent of systemic androgens dubbed Castration-Resistant Prostate Cancer (CrPCa) emerge throughout ADT. CrPCa remains a constant threat to individuals undergoing hormone therapy, often requiring more robust ADT drugs to extend the effectiveness of the therapy. In addition, the development of CrPCa is associated with a poorer prognosis due to higher malignancy and metastatic potential (Dutt & Gao, 2009). Depending on the specific ADT strategy and stage of cancer, estimates of CrPCa development can range from 140 months to little as 18 months (Miyake et al., 2019; Tamada et al., 2018). Escaping from the reliance on systemic androgens can emerge in several ways, including aberrations in AR regulation and enhanced de novo synthesis of androgens, summarized in Figure 5 (Imamura & Sadar, 2016).

For the AR itself, both its expression and structure can mutate to promote resistance against blockers. Sustained inhibition of the AR using antagonists can result in the AR overexpression or related transcription regulators to compensate for the inhibition. An increased 5α-reductase expression can enhance the conversion of the trace amounts of testosterone into the more potent DHT. The LBD of the AR can change to have enhanced binding affinity with androgens or for increased promiscuous binding with other steroids (Hara et al., 2003). Alternatively, the LBD can be forgone entirely with the expression of AR splice variants that remain consistently active or resistant to the inhibitory effects of blockers (Liao et al., 2020). These can require several drugs and strategies during ADT to remain effective against PCa. Classical inhibitors like Enzalutamide

may be used initially for low-risk PCa; once the more malignant variants emerge, the more specific AR targeting drugs are required, such as Niclosamide that can target AR-V7 splice variants (Keating, 2015; Liu et al., 2014). Optimal treatment is complex as constant patient surveillance is required to determine if the current therapy is still effective.

Another mechanism involves PCa tumors becoming self-sufficient with androgen synthesis. Upregulation in cholesterol synthesis and uptake has been observed and will be discussed in further detail in a later chapter (Gordon et al., 2019). Increased accumulation of cholesterol in PCa is associated with a poorer prognosis (Jamnagerwalla et al., 2018). This correlation between blood cholesterol and the risk for PCa tumor formation may be related to the increased availability of cholesterol in the blood. The increased accumulation of cholesterol provides the sterol molecules required to synthesize steroids, including androgens. The regulation of enzymes involved in androgen synthesis, such as CYP 17A1, has been observed (Cai et al., 2011). This upregulation suggests that the tumors can continue to grow without systemic androgens, rendering ADT types ineffective. Additionally, hypercholesterolemia has been reported as a side effect of ADT, suggesting that ADT may play a role in enhancing this CrPCa phenotype in the long term. The significance of cholesterol will be further discussed in section 1.3.1.

Finally, the crosstalk between the AR and other pathways has been observed, creating feedback loops that can sustain the activity of the AR. For example, as previously mentioned, the AR interacts with the mammalian Target of Rapamycin complex (mTORC1). This complex acts as a nutrient sensor for the cell and is a downstream element for the PI3K/AKT pathway (Wu et al., 2010). With the increased expression of mTOR in CrPCa and dysregulation of its upstream elements, mTOR inhibition has become an attractive target for cancer therapy (Kato et al., 2016). However, while suppression of mTOR in cell lines can elicit apoptosis, clinical trials have failed

to show favorable results using mTOR inhibitors alone in other cancers such as hepatocarcinoma (Zhang et al., 2018). In CrPCa, it has been suggested that these shortcomings could be due to additional crosstalk between the AR. Under androgen deficient cellular environments, there are reports that mTORC1 stimulates the expression of the AR, helping with the continued activity of the AR (Wu et al., 2010). In turn, this feedback loop resists inhibition and promotes the CrPCa phenotype. False positives and early employment of ADT may provide disastrous long-term

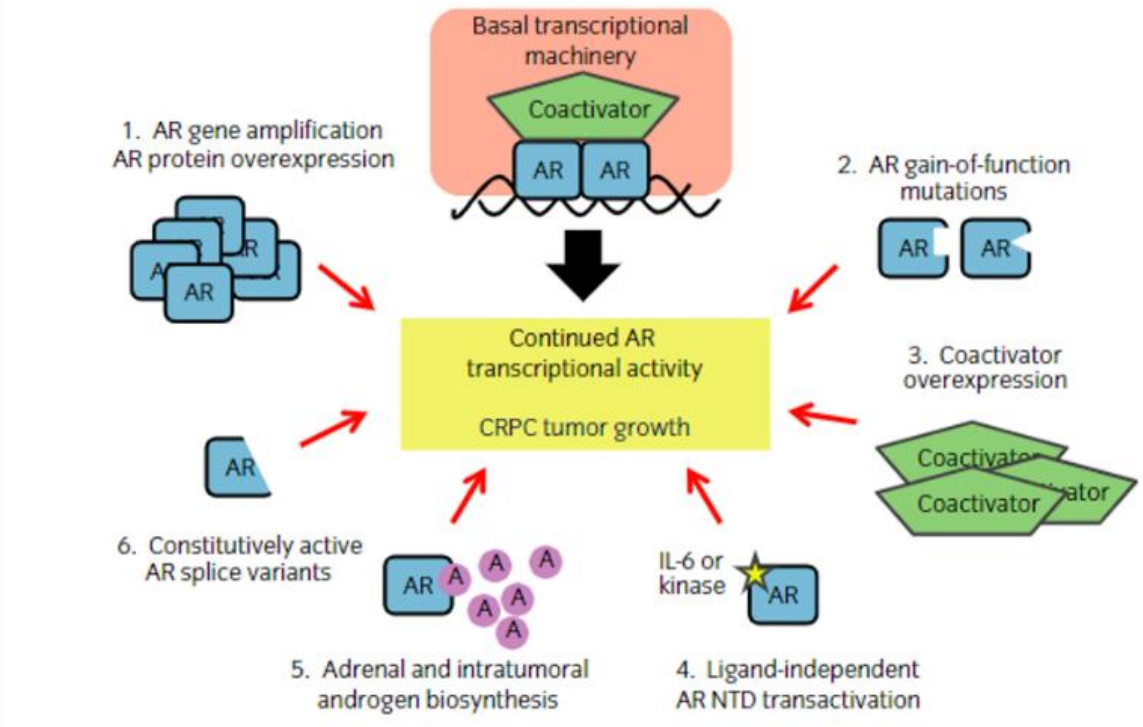

Figure 5. *The development of systemic androgen independence can occur through several different mutations reducing the effectiveness of ADT (Imamura & Sadar, 2016).*

complications by promoting this CrPCa phenotype (Sandhu & Andriole, 2012). Therefore, treatment at the CrPCa stage is limited to toxic chemotherapies such as taxanes, severely decreasing patient quality of life and only extending patient survival for a short period (Bumbaca & Li, 2018). There is a need for alternative therapies that selectively target PCa, including CrPCa, without targeting the AR due to the adoption of the castration-resistant phenotypes summarized in Figure 5.

1.2. α-Mangostin

1.2.1. Xanthones and α-Mangostin

A pharmacopeia of potent compounds remains undiscovered and underutilized within nature. Traditional medicines treat various diseases and often intersect with modern medicines. When isolated, specific compounds can transition into future therapeutics for various diseases. Endemic to southeast Asia, a striking purple fruit called the Mangosteen (*Garcinia mangostana*) has gained popularity as a health supplement and is often dubbed the "Queen of Tropical Fruits" (Aizat et al., 2019). As shown in Figure 6, the deep purple endocarp reveals a soft, white flesh described as mild in flavor. Local traditions have used the fruit to treat digestive issues, wounds, and inflammation (Pedraza-Chaverri et al., 2008). Despite its recent spotlight as "healthy" food, the fruit remains relatively rare stateside due to difficulty in growing and shipping.

Figure 6. *The Mangosteen fruit shown split open revealing its white flesh and purple pericarp (EXF, 2022).*

Various compounds have been found within the pericarp, including antioxidants and vitamins. In addition, daily consumption has been shown to provide beneficial health effects in randomized studies (Xie et al., 2015). However, a particular class of compounds called Xanthones are found in high abundance within the pericarp of the mangosteen pictured in Figure 7. Xanthones have

been shown to possess anti-bacterial, modulatory, and anti-cancer effects (Feng et al., 2020; Ibrahim et al., 2017; Kurniawan et al., 2021; Narasimhan et al., 2017). Xanthones are composed of conjugated rings that are highly modifiable and can exist within six different categories; however, plants naturally only produce simple, prenylated, and glycosylated xanthone compounds (Remali et al., 2022).

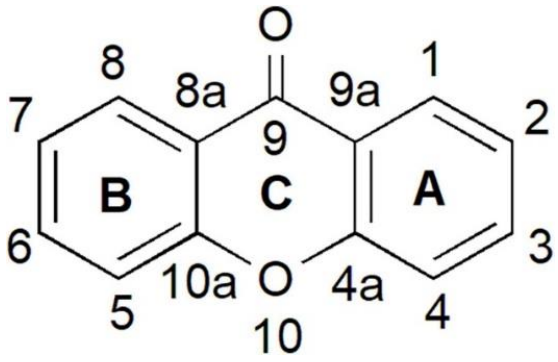

Figure 7. *Molecular structure of a Xanthone (Remali et al., 2022).*

The Mangosteen fruit has a high abundance of a prenylated family of xanthones called Mangostin that include γ-Mangostin, β-Mangostin, and, most relevant, α-Mangostin (Saraswathy et al., 2022). Particular interest has grown surrounding the bright yellow α-Mangostin for its various beneficial effects. First isolated in 1855, it took nearly a century for its structure to be revealed, as shown in Figure 8 (Schmid, 1855; Yates & Stout, 1958). Initial studies revealed its antioxidant and antimicrobial activity; however, serious interest in the compound developed after unveiling its selective anti-cancer effects (Sundaram et al., 1983; Williams et al., 1995).

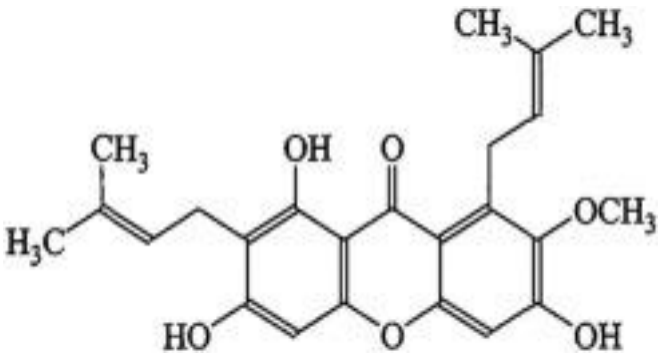

Figure 8. *Structure of α-Mangostin (Ibrahim et al., 2017).*

1.2.2. Anti-Cancer Effects of α-Mangostin

Early studies between 2003 and 2005 by Matsumoto et al. revealed that treating human leukemia and colon cancer cells resulted in the induction of apoptosis. Their initial study revealed that against human leukemia cell lines that treatment with α-Mangostin caused mitochondrial dysfunction resulting in caspase-3 and 9 activity (Matsumoto et al., 2004). At higher dosages, each of the four leukemia cell lines experienced cytotoxicity, as shown in Figure 9; however, against primary peripheral lymphocytes, α-Mangostin appeared to not negatively affect cell viability, as shown in Figure 10 (K. Matsumoto et al., 2003). This selective inhibition suggests that α-Mangostin was selective towards inducing apoptosis in cancers. The pathway α-Mangostin targeted had yet to be fully elucidated, but Matsumoto et al. reported evidence of mitochondrial disruption against this particular cell line.

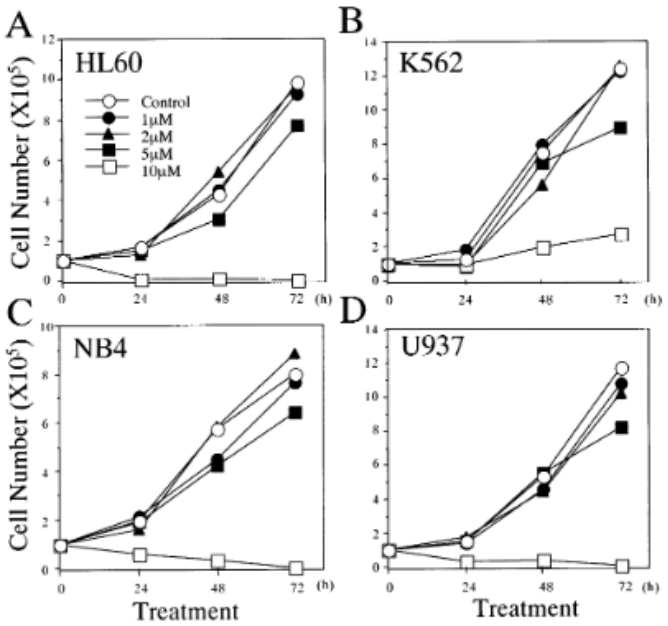

Figure 9. *Cell viability assay in response to dosages of α-Mangostin over 72 Hours. Four human leukemia cell lines cell viability curves are pictured above (K. Matsumoto et al., 2003).*

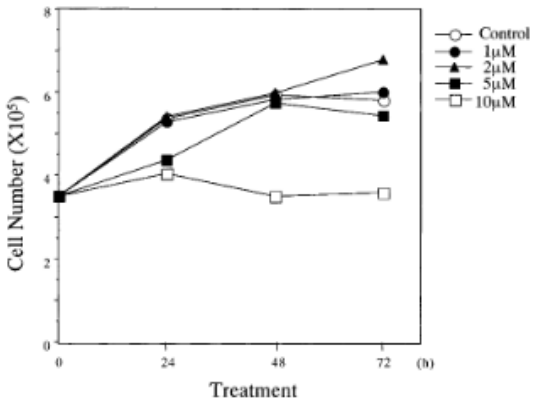

***Figure 10**. Cell Viability Assay in response to dosages of α-Mangostin over 72 Hours against primary peripheral lymphocytes (K. Matsumoto et al., 2003).*

In a follow-up study using the colon cancer cell line DLD-1, inhibition of the cell cycle was reported to prevent the cell cycle's transition (Matsumoto et al., 2005). Specifically, the DLD-1 cells were restricted to G1 through the reduced expression of cyclin D and CDK1, which are essential for cell cycle transition.

The anti-cancer effects have been reported in other cancers, summarized in Table 1, albeit through different mechanisms. For example, apoptosis through PARP cleavage has been observed in breast cancer. Additionally, the inhibition of fatty acid synthase and PI3K/AKT through the elimination of Retinoid X Receptor Alpha (Li et al., 2014; Zhu et al., 2021). Additionally, in Glioblastoma, α-Mangostin acted as an inhibitor to mTORC1 via modulation of AMPK, inducing autophagy. Finally, apoptosis, reduced AKT activation, and Cyclin D expression in pancreatic cancers was reported in addition to decreased metastatic potential (Xu et al., 2014). Together, these studies reveal a cancer-specific effect of the α-Mangostin when used against normal cells. An emerging pattern is that α-Mangostin inhibits the cell cycle in cancers through direct and indirect means. Against Prostate Cancer, apoptosis has been similarly observed with the treatment of α-Mangostin. The initial study reported by Hung et al. reported a reduction in the expression of c-jun, NF-κB, and c-fos when PC3 cells were treated with α-Mangostin. The reduction of these signaling proteins,

in turn, resulted in decreased expression of matrix metalloproteinases and urokinase-plasminogen activators, causing inhibition of metastasis (Hung et al., 2009). A follow-up experiment by Johnson et al. sought to elucidate the potential mechanism for inhibition and cancer selectivity. Treatment of several PCa cell lines with α-Mangostin, including 22RV1, PC-3, DU145, and LNCaP, resulted in caspase-3 mediated apoptosis in a dose-dependent manner. However, significant cytotoxicity was not observed in the primary epithelial cell line PrEC as shown in Figure 11 (Johnson et al., 2012). However, no IC_{50} has reported only a visual difference in the state of the cells. Again this shows the cancer selectivity that α-Mangostin possesses.

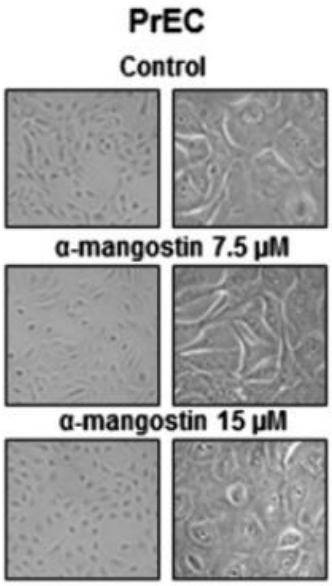

Figure 11. *After treatment with α-Mangostin the primary prostate epithelial cell PrEC did not have substantial amounts of apoptosis (Johnson et al., 2012).*

Kinase activity assays after treatment with α-Mangostin showed that only CDK4/Cyclin-D complex had significantly reduced activity. This specific decrease in activity suggested that α-Mangostin directly interacted with this kinase complex. In-silico models of the possible interaction suggest that α-Mangostin binds in a hydrophobic pocket at the ATP binding site on the CDK4/Cyclin D complex, as shown in Figure 12. The blocking of the ATP site results in the

inability to transition to the S phase of the cell cycle and, in turn, induces cellular arrest, causing apoptosis.

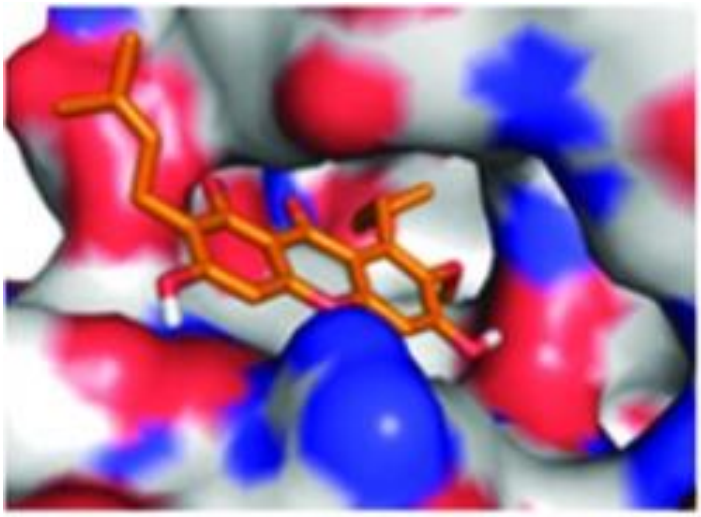

***Figure 12**. α-Mangostin blocking the ATP Binding site of CDK4 (Johnson et al., 2012).*

***Table 1.** Summary of reported anti-cancer effects of α-Mangostin.*

Mechanism For Inhibition	Cancer Type	Study
• Unspecified mitochondrial disruption	Leukemia	(Kenji Matsumoto et al., 2003; Matsumoto et al., 2004)
• Reduced expression of CDK1 and Cyclin D	Colon Cancer	(Matsumoto et al., 2005)
• Fatty Acid Synthase inhibitor • AKT inhibitor	Breast Cancer	(Li et al., 2014) (Zhu et al., 2021)
• Inhibitor of AKT and Cyclin D	Pancreatic Cancer	(Xu et al., 2014)
• AMPK Promoter	Glioblastoma	(Chao et al., 2011)
• CDK4/6 inhibitor • Inhibition of c-jun, MMP-9, fos and NF-κB	Prostate Cancer	(Johnson et al., 2012)

1.2.3. Interest Surrounding CDK4 Inhibitors.

Dysregulation of the cell cycle is an almost universal characteristic shared between cancers. Proliferation usually is gated through several cyclin-driven kinases that serve as checkpoints. If the specific criteria are met, the cell will be allowed to transition toward the next cell cycle phase. The unregulated signaling pathways such as AKT and the AR promote the transition to the next phase, and often, many of the pro-growth signals converge at these kinase checkpoints (de Brot & Mongan, 2018). For example, CDK4 regulates the transition from G1 to the S phase in response to Cyclin D. Normally; Cyclin D is produced in response to environmental and cellular states; however, it is often overexpressed in cancers by the increased activity of signaling pathways promoting the transition S phase. In addition, the Phosphate and Tensin homolog (PTEN) is often lost due to mutation. For example, it has been found that 50% of CrPCa tumors will lose PTEN, resulting in decreased regulation of Cyclin D expression (Jamaspishvili et al., 2018).

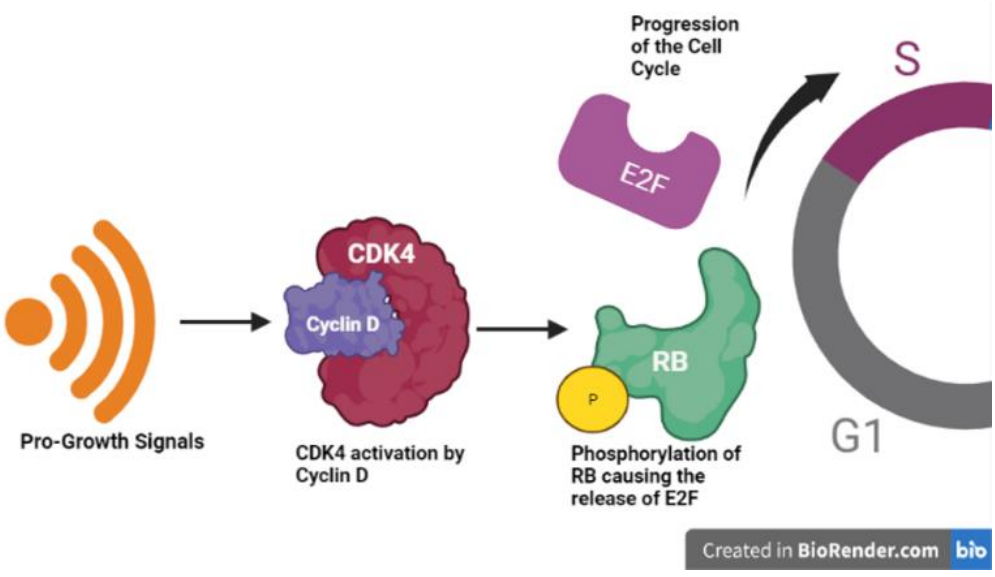

***Figure 13**. Transition from G1 to S phase requires the phosphorylation of RB by the CDK4/Cyclin D complex.*

Together, the CDK4/Cyclin D complex phosphorylates the retinoblastoma protein (RB), causing the release of a transcription factor called E2F. As shown in Figure 13, the release of E2F allows

for Cyclin E's expression and the S-Phase's progression. However, if the E2F remains bound to RB due to insufficient activity by CDK4, the cell transitions towards apoptosis. Inhibition of CDK4 theoretically allows for blocking the cascade of pro-growth signals and induces tumor regression. The CDK4/6 inhibitor Palbocicilib and Ribociclib have recently been approved for usage against breast cancers. In addition, clinical trials have shown promising results in both individual and combinational therapies (Nur Husna et al., 2018). However, these chemotherapeutics do not distinguish between normal or cancerous cells and therefore induce cell death throughout the body. The cancer-selectivity of α-Mangostin makes it unique as it may have few side effects if absorbed by normal cells and is relatively safe.

1.2.4. Limitations of α-Mangostin

Against prostate cancer, α-Mangostin has the potential to become a serious cancer chemotherapeutic. Previous studies have shown that it is a cancer-selective CDK4 inhibitor, which could be used alone or in a combinatorial therapy. In addition, the drug selectively induces apoptosis; therefore, tumor regression is possible without significant damage to normal tissue according to animal models, unlike other chemotherapies.

However, like many other naturally derived plant compounds, α-Mangostin is marred by its hydrophobicity, bio-availability, and systemic distribution. Drugs such as curcumin have seen little success as a viable treatment due to poor oral availability and insolubility. Direct systemic delivery can be inefficient or dangerous unless extensive modifications to the structure of the hydrophobic compound are made to improve its solubility, which may abrogate any beneficial effects (Kalepu & Nekkanti, 2015; Prasad et al., 2014). A standard measure of insolubility is the octanol-water partition, or XlogP, which measures a compound's relative hydrophobicity concerning polar and nonpolar solvents (Cumming & Rücker, 2017). With an XlogP of 6.3, α-Mangostin is more

hydrophobic than curcumin, which has an xLogP of 3.2 (NCBI, 2022a, 2022b). This high degree of insolubility may contribute to its poor oral bioavailability. Oral dosages for many in-vivo experiments are often high due to poor bioavailability. For example, concentrations above 100mg/kg have been safely administered to mice; however, they only resulted in relatively low blood plasma concentrations (Ramaiya et al., 2012). Tumor reduction was observed in the in-vivo xenograft models used in the Johnson et al. study using orally delivered α-Mangostin. However, these were substantial dosages of 100mg/kg over 34 days (Johnson et al., 2012). While not toxic to the mice, these large dosages are an inefficient mode of delivery to the tumor sites. Translating this to clinical trials would require patients to consume massive dosages of α-Mangostin for an extended time. In addition, the poor biodistribution of the drug may not allow for efficient penetration of the tumor microenvironment. Biodistribution studies have shown that after an oral dosage, the small intestine, liver, and pancreas have the highest concentration of α-Mangostin (Zhao et al., 2016). Additionally, the systemic delivery of α-mangostin alone may result in other problems. For example, hydrophobicity may cause aggregation, reducing its ability to disperse within the bloodstream and off-target uptake by non-target cells.

1.3. The rHDL Drug Delivery System

1.3.1. Cholesterol's Role in the Progression of Prostate Cancer

The accumulation of cholesterol is a common trait shared by many different cancers. It has been suggested that cholesterol is a driving factor for various cancers, including PCa. Early studies in the 1940s have reported significantly higher cholesterol concentrations in PCa tumor biopsies compared to normal prostate epithelial and BPH tissue (Swyer, 1942). Despite some of the shared dysregulation in growth between PCa and BPH, the accumulation of cholesterol appears to be a feature specific to PCa. Lifestyle has been reported to influence the risk of PCa, with high-fat diets

and high cholesterol levels. Studies have reported a link between hypercholesterolemia and increased morbidity due to PCa (Hirano et al., 2020; Jamnagerwalla et al., 2018). Additionally, hypercholesterolemia is one of the metabolic side effects associated with some forms of ADT, such as GnRH agonists (Choi & Kam, 2015), which may provide another driver in addition to the androgen independence from systemic androgens, thus promoting the growth of CrPCa (Jeon et al., 2016).

What benefit would increased cholesterol accumulation bring to higher grade PCa? Growing cells require cholesterol to maintain the membrane's integrity and form lipid rafts. In addition, rapidly proliferating cells require more cholesterol to ensure they can divide, increasing their appetite for cholesterol. However, cholesterol can also drive proliferation through participation in a positive feedback loop. Cholesterols are the backbones for hormones such as androgens. Increased androgen production increases the activity of the AR, but what drives this phenotype?

As described previously, one phenotype observed in CrPCa is the enhanced activity of intratumoral synthesis of androgens. These can activate the AR in a paracrine or autocrine fashion, thus promoting AR-driven tumor proliferation (Penning, 2014). However, the AR plays an additional role by modulating cholesterol homeostasis through a positive feedback loop summarized in Figure 14. The AR can inhibit the nuclear receptor liver X receptor (LXR), responsible for controlling cholesterol homeostasis through the transcription of genes to reduce cholesterol accumulation (Zhao & Dahlman-Wright, 2010). LXRs maintain cholesterol efflux and inhibit the activation of pro-survival pathways (de Boussac et al., 2013). Therefore, the AR inhibits one side of the cholesterol homeostatic regulatory mechanism and inhibits cholesterol efflux.

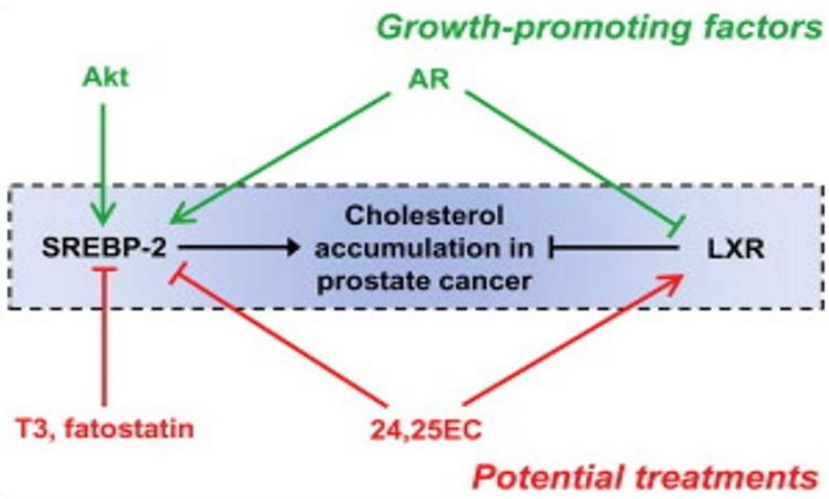

Figure 14. *The Androgen Receptor mediates the expression of LXRs and SREBPs to enhance the accumulation of cholesterol (Krycer & Brown, 2013).*

Conversely, the AR can activate sterol regulatory element-binding protein-a1 (SREBP), promoting lipogenesis. Normally sterol levels inside the cell regulate the activity of SREBP, where low levels of sterols induce activation of both exogenous and endogenous cholesterol accumulation pathways. The endogenous synthesis of cholesterol is increased through SREBP activity by enhancing the expression of the rate-limiting enzyme HMG-Reductase which can be elevated in PCa (Bengoechea-Alonso & Ericsson, 2007; Longo et al., 2019). Some studies have pointed to inhibition via statins as a potential therapeutic. However, meta-analyses between studies on statin usage have not shown promising results (Meijer et al., 2019).

To further promote cholesterol uptake, SREBP upregulation increases the expression of various lipid transporters. Because lipids are not freely circulated in the plasma due to their hydrophobicity, they require a carrier to transport lipids and isolate them from the aqueous environment of the bloodstream. Often these carriers are lipoproteins whose structures are composed of phospholipids and apolipoproteins. Cholesterol is primarily transported via these lipoproteins, which are categorized by their protein-to-lipid ratio. The 'Good" and "Bad"

cholesterol we often hear about are cholesterol levels in different types of carriers. Very Low-Density Lipoproteins (VLDL) have the lowest protein-to-lipid ratio, while High-Density Lipoproteins (HDL) have the highest protein-to-lipid ratio (Randolph & Miller, 2014). As shown in Figure 15, phospholipids form a hydrophilic exterior that can interact with a polar solvent. At the same time, the long lipid tails form a hydrophobic core that can dissolve various lipids, including esterified cholesterols and triglycerides. Apolipoproteins form and maintain the structure of the lipoproteins while serving as the ligand for their respective receptors for transport.

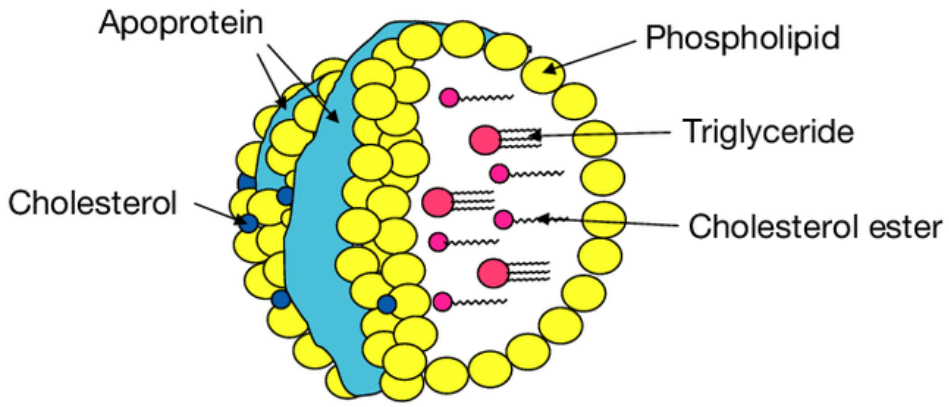

Figure 15*. General structure of lipoproteins (Chiang, 2014).*

The HDL is of note as it plays a significant role in transporting cholesterol in the reverse cholesterol transport pathway. The liver usually produces HDL to collect excess cholesterol and transport it back to the liver (Brody, 1999). The liver is the only organ capable of metabolizing cholesterol into bile acids. Therefore, the HDL plays an essential role in maintaining the cholesterol homeostasis in the body, especially in preventing the formation of plaques in the arteries due to the transformation of macrophages into foam cells; for this protective effect on cardiovascular health, they are dubbed good cholesterol. HDL concentration in the blood and PCa risk is mixed, with some studies pointing to little or no significant effects (Wolny-Rokicka et al., 2019). However, it is known that the primary receptor for HDL, the scavenger receptor class B type 1 (SR-B1), plays a significant role in the progression of CrPCa (Gordon et al., 2019). The

receptor activates the one-way non-endocytosis transfer of the HDL cargo into the cell when activated by the apolipoprotein portion of the HDL. In addition, it can activate a set of downstream signals such as c-Src and PI3K, which promote growth.

Generally, the SR-B1 is overexpressed in a wide variety of cancers, which is thought to aid in intercepting circulating HDL and converting the tumors into cholesterol sinks. The SCARB1 gene expresses the SR-B1 and its accompanying isoforms; however, the genetic regulation for the SR-B1 is not fully understood. Intracellular cholesterol levels appear to influence the upstream elements that control the expression of SR-B1. SCARB1 is partially regulated by SREBP-2, which in turn is regulated by levels of cholesterol present in the endoplasmic reticulum (Eid et al., 2017; TréGuier et al., 2004). Activated mTORC1 has been reported to decrease ER cholesterol levels, inducing steroidogenesis and cholesterol uptake (Lim et al., 2019). Furthermore, when SR-B1 is activated, PI3K is stimulated upstream to mTORC1, providing another positive feedback loop regulating intracellular cholesterol levels. Inhibition of SR-B1 expression, however, induces the shift toward endogenous cholesterol synthesis and increases the expression of HMG-Reductase (Gordon et al., 2016). Conversely, inhibiting HMG-reductase increases the exogenous scavenging of HDL by increased expression of SR-B1 (Gordon et al., 2019).

Higher grade CrPCa has been shown to overexpress the SR-B1, suggesting an adaptation to low levels of systemic androgens (Gordon et al., 2019). In addition, SR-B1 overexpression is often associated with a poorer prognosis. Enhancing steroidogenesis requires cholesterol for androgen synthesis; therefore, upregulating cholesterol uptake through HDL interception provides a readily available source of materials for proliferation. Direct targeting of these associated pathways has shown little overall success. Usage of statins has yet to show any compelling effects in treating CrPCa (Meijer et al., 2019). Direct inhibition of SR-B1 using blockers such as BLT-1 is quite

cytotoxic to cells. Furthermore, the SR-B1 is a surface receptor making targeted inhibition currently unfeasible. Nevertheless, this overexpression could provide a potential treatment target, as discussed in the following sections.

1.3.2: Nanoparticles

Limitations in drug delivery often plague the development of drugs and treatments. For example, poor solubility and toxicity can roadblock clinical studies resulting in premature termination of potentially viable drugs. Hence, due to these challenges, rise in interest in developing nanocarrier drug delivery systems. First described in 1857 by Dr. Michael Faraday with his colloidal suspension of ruby and gold nanoparticles, the field of nanotechnology has exploded in popularity these past few decades in medicine (Thompson, 2007). Generally, a drug of interest is formulated with a nanocarrier to isolate it from the surrounding aqueous environment or non-target cells. In addition, the particles' nanoscale (typically ranging from 1-100 nm) aids in navigating the vasculature, reducing aggregation or accumulation within the tissue (Park, 2013). However, nanoparticles can differ in their materials, composition, targeting potential, and drug and bio-compatibility; therefore, these carriers require intensive characterization to ensure their inclusion does not produce determinantal effects after treatment.

Using nanocarrier for cancer therapeutics to reduce the cytotoxic effects of chemotherapy drugs is an important strategic goal. Many potent chemotherapies such as taxanes are effective at killing cancer. However, they lack specificity and cause damage to cells throughout the body, including those that are healthy. A carrier can allow a once toxic or hydrophobic drug to be used in severe treatments against cancer. However, nanoparticles themselves can induce adverse effects.

Due to the body's complex nature, several vital qualities are essential for a nanoparticle to possess for systemic delivery. Firstly, the particle should remain biocompatible with the body. Injection

with non-inert materials, either organic or non-organic, can induce toxicity to tissues and organs. For example, some metal particles have been reported to induce cytotoxicity through oxidative reactions with macromolecules and organelles such as the mitochondria (Karlsson et al., 2009). Alternatively, nanoparticles produced using biosynthetic materials such as proteins from non-human species may induce significant systemic immune responses. At the same time, immunostimulation can be used to treat cancer; however, non-specific stimulation is a dangerous side effect. These, in turn, can cause the treatment to produce harsh side effects or exhibit mortality to patients regardless of the drug payload.

Secondly, the body must be able to metabolize the nanoparticles to prevent accumulation in tissue. The particles or components could induce local carcinogenic effects or inflammation if accumulation occurs. Heavy metals from tattoo dyes, for example, have already been reported to accumulate within the lymph nodes (Kürle et al., 2009). While no specific study has been done to determine if these local accumulations with tattoo ink can encourage the development of cancers, heavy metal nanoparticles are implicated in at least one case. A 25-year-old individual developed stage four lymphoma due to an accumulation of toxic metal nanoparticles within the lymph nodes to environmental exposure (Iannitti et al., 2010). Metal nanocarriers could carry these same risks under prolonged treatment if they are not processed efficiently by the body (Attarilar et al., 2020). Natural processes that metabolize the nanoparticle shell prevent bioaccumulation. However, conversely, these processes should not degrade the particles immediately after administration; otherwise, the nanoparticle will release its cargo prematurely, eliminating the benefit of using the nanocarrier.

Thirdly, the nanoparticles should retain their cargo until contact with the target cell is made. Specificity is vital for reducing off-target binding and the amount of total drug required to elicit

beneficial effects. This specificity should take advantage of a cellular feature such as a unique or overexpressed receptor. The targeting will reduce contact with non-target cells and limit activation of the nanoparticle uptake. Modifying the nanoparticle shell can improve the specificity of targeting a single cell type. For example, differential expression of surface receptors is a common feature in many different cancers and immune cells (Thienger & Rubin, 2021). However, targeting cells remains a challenge as, besides navigating the vasculature, the composition and organization of cells can affect their receptiveness to a nanoparticle. Tumors, for example, induce the formation of a tumor microenvironment (TME) that changes this region's cellular expression and extracellular matrix to suit the tumor better. Penetrating the TME may prove a challenge as, without specific targeting affinity, an insignificant dosage may reach the tumor. A meta-analysis determined only a paltry 0. 7% of the total payload of some nanoparticles reached the target cancer cells (Wilhelm et al., 2016). Often this is far below the necessary concentration required for inhibiting a tumor and thus may reflect poor results under clinical trials.

Finally, the particle size can affect both distribution and uptake of the nanoparticle. Small particle sizes may have better penetration ability than larger particles. However, they are susceptible to removal by the body. Particles below 15nm in size risk early filtration by the renal system (Choi et al., 2011). Therefore, removing the loaded nanocarrier before it can reach its target destination. However, if the particle is too large, there may be reduced capability for the particle to traverse the vasculature and initiate an immune response. Particles above 200nm may activate the complement system causing inflammation which could have disastrous effects if a large dosage is administered (Mitchell et al., 2021). Additionally, the size can affect the uptake pathway as different forms of phagocytosis can occur depending on the particle's size (Hoshyar et al., 2016). However, if a receptor-mediated process takes the nanoparticle, this may not be a significant issue. Depending

on the assembly and type of nanoparticle, there may be exclusion from some systems. Figure 16 summarizes these ideal features.

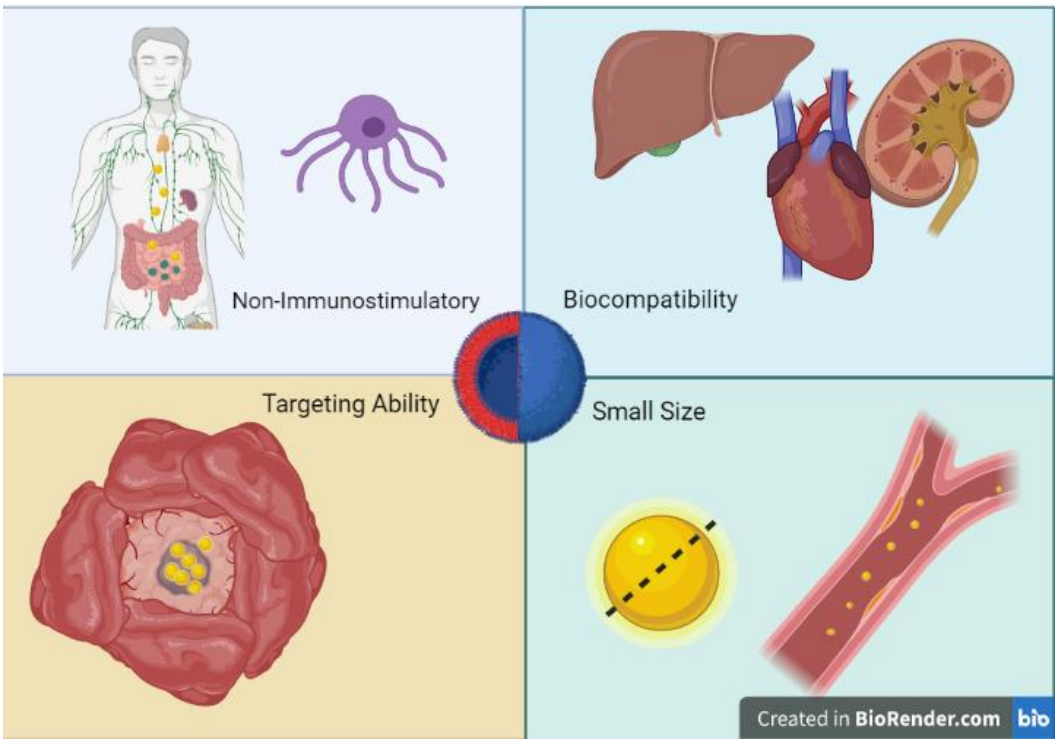

Figure 16*. Elements for an ideal nanoparticle against cancer.*

An ideal nanoparticle targeting PCa tumors should possess the following qualities. First, a small size below 100nm to navigate the body's vasculature. Second, biocompatibility prevents toxicity of the particle itself and accumulation within the body. The ability to isolate the drug from the environment and off-target binding until a target cell is reached. Together, within this narrow criterion, one nanoparticle, in particular, meets these qualities: the reconstituted High-Density Lipoprotein nanoparticle or rHDL (Lacko et al., 2015). The rHDL is a sub 100nm biocompatible nanoparticle that mimics the intrinsic HDL in the human body. This mimicry extends to its non-immunostimulatory nature and ability to be processed by the body. These features are due to the human apolipoproteins used to compose its shape depicted in Figure 17. However, the apolipoproteins also allow for the targeting of high SR-B1 expressing cells like PCa and CrPCa.

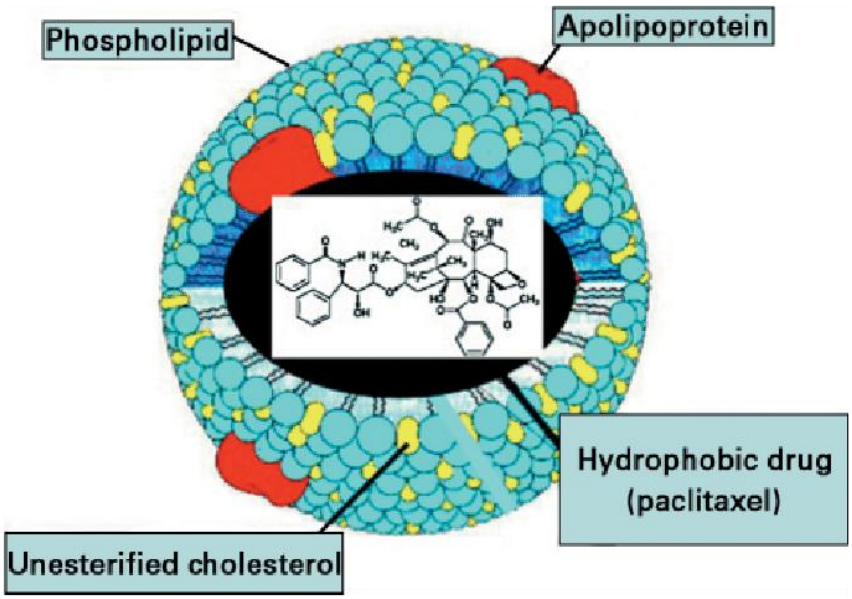

Figure 17*. Structure of the rHDL nanoparticle (Lacko et al., 2015).*

1.3.3. The rHDL

Initially, interest surrounding the HDL was through its reported protective role in heart disease. High HDL levels were correlated with decreased risk for heart disease, while conversely, higher LDL levels showed an increased risk for the development of cardiovascular disorders (Kwiterovich, 1998; Tan, 1980). Isolated apolipoprotein was discovered to retain its ability to produce HDL outside the body, allowing for the synthetic HDL. Synthesis of this early rHDL involved using apolipoproteins, esterified cholesterol, and phospholipids to mimic the intrinsic HDL present in our bodies. These rHDLs were used initially to serve as models for understanding the structure and function of the HDL (Ritter & Scanus, 1977; Rye & Barter, 1994). The utilization of the rHDL further expanded into unearthing its relationship with other lipoproteins and its role in the reverse cholesterol transport pathway (Bolin & Jonas, 1994; Rye et al., 1995). These studies revealed the protective role of the HDL against heart disease through the uptake of excess cholesterol via the SR-B1 preventing the formation of plaques. However, experimentation with

the rHDL expanded its application to include additional types of cargo, such as fluorescent probes and drugs.

Many studies have reported overexpression of the SR-B1 found in various cancers. As discussed, cholesterols and other lipids can significantly enhance the transition towards more malignant phenotypes. Increased expression of the SR-B1 can allow for enhanced uptake of these lipids through the interception of systemic HDL. Discussion of the rHDL as a drug delivery tool emerged in the early 2000s, highlighted by the flexibility of the formulation of the rHDL and the overexpression of the SR-B1 found in cancers. One of the first major studies to highlight the targeting potential of the rHDL occurred with the encapsulation and delivery of taxol by Lacko et al. The PCa cell lines DU145 and PC-3 were shown to have a high expression of the SR-B1. When treated with the rHDL-Taxol particles, there was significant uptake and cytotoxicity of these rHDL-Taxol particles (Lacko et al., 2002). The toxicity of taxol showed a possible benefit in delivering this drug to cancer cells directly and avoiding the systemic complications that arise when orally delivered. While this early study only highlighted the potential for the rHDL to incorporate taxol and suggested an SR-B1-specific uptake of the rHDL cargo, more studies were required.

Following this study, a more robust study was conducted using the chemotherapeutic Valrubicin (AD-32). Valrubicin is a modified form of anthracycline Doxorubicin. Generally, Valrubicin is described as less cardiotoxic than its parent drug (Onrust & Lamb, 1999). However, due to its hydrophobicity, it has a limited route of administration. Therefore, unlike its more toxic Doxorubicin form, Valrubicin has not been used as a significant chemotherapeutic. Its hydrophobicity made it a strong candidate for delivery via the rHDL. The rHDL enhanced the cytotoxicity of the Valrubicin against PCa and ovarian cancer cell lines. However, it revealed a

protective effect against low Sr-B1 expressing cell lines (Lacko et al., 2012). This protective feature highlights the enhanced delivery of the rHDL system as the low SR-B1 expressing cells in this 2D culture represent "normal" cells.

Later studies from other labs further experimented with the payloads of the rHDL. These include the delivery of RNAs such as miRNA inhibitors like miR-204-5p-ih and siRNA (Chen et al., 2019; Shahzad et al., 2011). With proper formulations, various materials can be encapsulated within the rHDL and be selectively delivered to high SR-B1 expressing cells. The flexibility of the rHDL has allowed it to carry several drugs with various solubilities. For a drug to be considered relatively hydrophobic, it needs an xLogP greater than 0; the higher the value, the more hydrophobic a compound is. The natural cargo for the rHDL is cholesterol esters with an xLogP of about 16.1, making them incredibly insoluble in polar solutions (NIH, 2022). However, many drugs with an xLogP far below the value of cholesterol esters have been encapsulated within the rHDL. For example, With an xLogP of 4.0, Valrubicin was delivered via the rHDL in several cancers, including ovarian and prostate (Lacko et al., 2012). Less insoluble, Amphotericin B has an xLogP of 0, making it relatively soluble in both polar and nonpolar solutions; this was encapsulated to aid in delivery for the treatment of oral thrush (Oda et al., 2006).

Table 2. *Table Summarizing some of the different materials delivered by the rHDL.*

Cargo Delivered via the rHDL	Purpose	Study
Valrubicin	• Targeted delivery of Valrubicin to cancer • Reduced cardiocytotoxicity	(Lacko et al., 2012)
Taxol	• The pilot study used to demonstrate the rHDL as a drug delivery platform	(Lacko et al., 2002)
Amphomectrin B	• Treatment for Oral Thrush	(Oda et al., 2006)

miRNA	• Targeted Delivery of miRNA	(Chen et al., 2019)
siRNA	• Pilot study for delivering anti-metastatic siRNA to colorectal and ovarian cancer	(Shahzad et al., 2011)

1.4. Utilization of Fluorescence Techniques for Nanoparticle Characterization

1.4.1. Overview

Fluorescence-based measurements have been a scientific mainstay for decades, if not centuries. From determining the concentration of a compound to its location in a system, these properties alone can tell researchers a vast amount of information. With more sophisticated detection methods, molecular phenomena such as binding, aggregation, and rotation can be determined based on the fluorescent properties. Nanoparticles' small size makes tracking and characterization challenging without specific types of equipment. Utilizing dyes and fluorescent moieties systems, one can directly monitor a nanoparticle without the destruction or loss of the nanoparticles (Wolfbeis, 2015).

If the cargo of the nanoparticle possesses intrinsic fluorescent properties, then non-intrusive methods can be utilized to characterize the particles. The particle quality, degree of encapsulation, and particle/drug location can be determined by measuring the fluorescent properties of the drug or payload. At a basic level, the excitation and emission spectra can be used to determine the concentration of the drug, particular moieties, or the scattering profile of a nanoparticle sample. However, using a wavelength within the excitation spectra causes the fluorophore to absorb photons and enter an elevated or "excited" state. This state of higher energy is not stable and eventually causes a release of the energy in the form of photons at a longer wavelength (Berezin & Achilefu, 2010). The intensity of the emitted light depends on its environment, excitation wavelength, the structure of the fluorophore, and any interactions the fluorophore has within this

environment. For example, a solvent can affect a fluorophore's emitted intensity, the length of time it remains in this excited state, and the emission spectra. Additionally, the separation of excitation and emission maxima or stoke shift can cause spectral overlap that may cause interference with reported measurements (Simonsen & Kromann, 2021).

Changes in intensity can reveal necessary information about the factors previously mentioned. For nanoparticles, these can be important for determining if encapsulation is occurring. If the characteristic emission or excitation spectra are present in the same fractions as the nanoparticle, this can suggest an association; however, if there are changes in the relative intensities of the emitted fluorophore, then an interaction between the fluorophore and some components is present in the sample. These observations may require additional studies, which will be described below. The more complex a system, the more complex the interactions a fluorophore will have in its environment. For example, the nanoparticle may contribute to its fluorescence, affecting the resulting intensity. In addition, the particle and solvent can produce their scattering, causing particle and Ramen scattering, respectively. Proper blanking procedures and environmental conditions are essential to reduce measurement interference.

1.4.2. Fluorescence Anisotropy

It is often assumed that the properties of matter remain static in all directions. However, physical properties such as absorbance and mechanical strength can differ based on the direction in that matter is observed or applied (Ostojic et al., 2007). For example, the force required to split a wooden block will differ depending on the direction you chop. These different properties based on direction are called Anisotropy, which comes from the Greek word Aniso- meaning unequal and -tropy, meaning movement (Oxford). There are many different applications for anisotropy; however, its primarily used to enhance scientific models further and determine the behavior of

matter. For example, fluorescence anisotropy (FA) applies directional effects of emitted light, allowing additional information about the fluorophore to be measured.

Steady-State FA can measure the degree of free molecular rotation of a fluorophore based on its parallel and perpendicular emitted light components. It is often used in determining protein interactions, such as binding between fluorescently tagged proteins. The value of the FA is given in a ratio between 0 and 0.4. The closer a value is to 0, the higher its uninhibited free rotation is. Conversely, a value closer to 0.4 suggests highly polarized fluorophores that may have their motion blocked due to bindings. For example, suppose a tagged ligand has a low anisotropy of 0.08 that suddenly rises to 0.25 after introducing it to a different protein. This elevation in anisotropy could suggest that binding occurs between the two proteins (Gradinaru et al., 2010). The anisotropy is highly sensitive to the temperature because of the random movement of molecules or Brownian motion, the solvent's viscosity, pH, and polarity. In addition, aggregation or interaction with other components in the solution can change the anisotropy. However, it is not directly concentration-dependent unless aggregation is an issue (Gradinaru et al., 2010).

The formula for anisotropy calculations is in Figure 18. Light from the excitation source and the light emitted from the sample can be broken up into parallel (VV) and perpendicular (VH) components using a polarizer (Shah et al., 2016).

$$r = \frac{I_W - GI_{VH}}{I_W + 2GI_{VH}}$$

Figure 18. *Anisotropy formula (Shah et al., 2016).*

In addition, the G or instrumental correction factor is calculated using the formula in Figure 19. The value G corrects the variance between the polarizer intensities (Gradinaru et al., 2010).

$$G = \frac{I_{HV}}{I_{HH}}$$

Figure 19. *The formula for the instrument correction factor (JASCO, 2022).*

It is possible to determine if encapsulation occurs between the drug and a nanoparticle using the FA. Previous studies have employed FA and other fluorescence-based measurements to characterize nanoparticles formulated with fluorescent drugs such as doxorubicin myr-5A mimetic nanoparticles (Raut et al., 2020). The anisotropy can give information about the fluorophore at the local level. If the dye is a fluorescent drug, some information about its state can be deduced from the anisotropy. For example, if encapsulation occurs, the anisotropy value will increase significantly between the free drug and the assumed drug-loaded nanoparticle. Conversely, if the anisotropy continues to decrease over time, this can suggest the leaking of the payload. The anisotropy can only suggest encapsulation, and additional studies are required to determine that encapsulation is successful entirely.

1.4.3. Fluorescence Lifetime

After a fluorophore is excited, the emitted photons are released, however not immediately. Instead, the fluorophore can stay in this excited state for some time. The time it remains excited can be anywhere from nanoseconds to picoseconds before releasing its energy (Berezin & Achilefu, 2010). However, how long a fluorophore remains excited depends on the environment and the other molecular interactions the fluorophore may have. The Fluorescence Lifetime (FLT) measures the time a fluorophore remains excited before emitting a photon and returning to its ground state. Figure 20 depicts a time-domain FLT curve. A pulse excites the sample, and the

distribution of emitted photons is plotted over time. Similar to the anisotropy, it is a concentration-independent characteristic of the fluorophore that can change in the presence of different environmental interactions. For this reason, the FLT has been to determine differences in membrane protein conformation to show changes in the local environments of amino acids (Raghuraman & Chattopadhyay, 2007).

An average amplitude fluorescence lifetime value can be calculated. Additionally, the slope of the curve and its components can tell additional information about the composition of the fluorescent signals. For example, in more complex samples utilizing additional components such as fluorescent drugs and proteins, the different make-up of the emission can be quantified, as shown in Figure 20 (Suhling et al., 2015). In addition, long and short components can be quantified and separated to give a complete picture of the emission. Furthermore, changes in the slope can be used to determine which type of quenching is occurring. Both of these features can be utilized for characterizing nanoparticles. For example, changes in the FLT may suggest the drug's aggregation inside the particles.

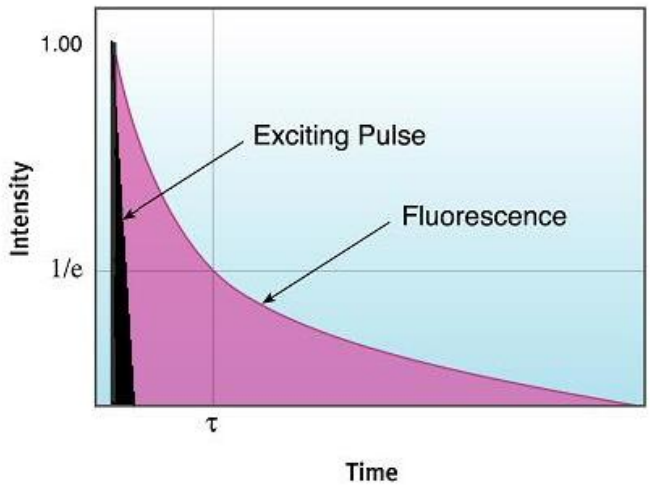

Figure 20. *Fluorsence Lifetime Curve. After an exciting pulse is administred, the intensity decay of the emission is measured and plotted as a curve (Jameson, 2005).*

Conversely, if the particles are disrupted, and the FLT returns, this can indicate that the drug was inside the particles. Additionally, the FLT can be used with fluorescence lifetime imaging (FLIM), which can visualize changes in the lifetime. For example, if a loaded nanoparticle has a short lifetime, but after delivery, the lifetime returns the value of the free drug, suggesting the particle has unloaded its cargo into the cell. Together, these fluorescent measurements can complement and further provide evidence of the successful incorporation of a fluorescent drug within a nanoparticle.

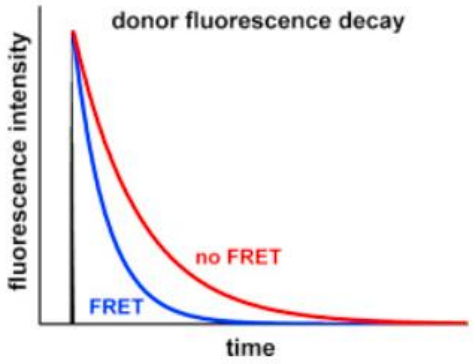

Figure 21. *Changes in the fluorophore's local environment can cause shifts in the slope such as due to presence of quencher (Suhling et al., 2015).*

Chapter 2

Project Hypothesis and Specific Aims

2.1. Project Goal and Hypothesis

As a compound, α-Mangostin has been reported to possess different selective anti-cancer effects against various cancer. However, despite its history of over 150 years, it has yet to enter any relevant clinical studies. Instead, it has been relegated to health supplements and the occasional headline. The primary limiting factors for the usage of α-Mangostin as a chemotherapeutic treatment lie in its insolubility and poor oral bioavailability (Li et al., 2011; NCBI, 2022a; Zhao et al., 2016). High dosages are often used in experiments because of the poor absorption, requiring large amounts of the drug to reach the therapeutic window (Johnson et al., 2012). While no acute toxicity has been reported, it is inefficient and unrealistic to translate these large dosages to human patients. Efforts have been made to enhance the solubility of α-Mangostin through structural modifications; however, no pharmacokinetic or extensive biological research has been conducted regarding these derivatives (Tran et al., 2021).

Furthermore, a sizeable inefficient dosage may still be required to induce cytotoxicity to tumors without a targeting system. Various nanocarriers have been formulated with α-Mangostin, such as protein and metal-based nanoparticles (Wathoni et al., 2020). However, these too often remain confined to mice studies and have yet to transition to clinical trials. In addition, issues with targeting, biocompatibility, and cytotoxicity remain a barrier to these studies (Attarilar et al., 2020; Iannitti et al., 2010). An ideal nanoparticle drug delivery system should have particles of small size, biocompatibility, exclusion from rapid filtration, and a targeting system to reduce off-target binding to healthy tissue.

The rHDL drug delivery platform falls uniquely within these criteria of a biocompatible nanoparticle that harbors a targeted delivery system. It has been previously demonstrated that the rHDL can encapsulate a variety of compounds, isolating them from the aqueous environment and preventing premature drug release. However, only until the rHDL binds explicitly to the SR-B1 will the receptor-mediated transfer of the compound to the target cell occur (Mooberry et al., 2016).

As discussed, valrubicin, a toxic hydrophobic drug, was previously loaded into the rHDL. These rHDL-Valrubicin nanoparticles displayed protective effects against non-cancerous tissue while enhancing the toxicity against a panel of cancer cells (Lacko et al., 2012). The hydrophobicity and possible fluorescent characteristics of α-Mangostin make it a candidate for encapsulation within the rHDL,

The increased cholesterol uptake found in PCa enhances progression towards more malignant variants. The enhanced expression of both endogenous synthesis and exogenous cholesterol uptake allows for increased intra-tumoral androgen synthesis. More expression of the SR-B1 allows for increased scavenging of intrinsic HDL, causing the CrPCa to become a cholesterol sink and a potential target for drug-loaded rHDL. Because of the hydrophobicity of α-Mangostin, we

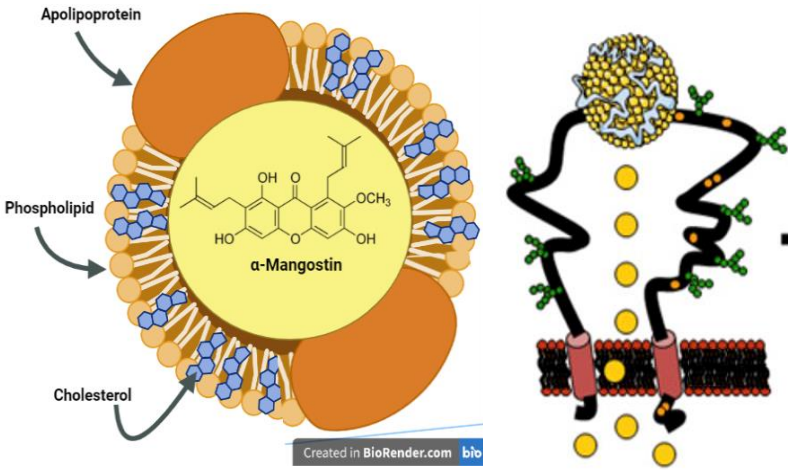

Figure 22. *(Left) Model of the rHDL-AMN Nanoparticle (Right) The SR-B1 mediated transport of the cargo from the rHDL into the cell.*

hypothesize that it can be encapsulated within the rHDL, producing stable and homogenous rHDL α-Mangostin (rHDL-AMN) nanoparticles that retain the cytotoxic effects of α-Mangostin and are delivered via the SR-B1 to the cell shown in Figure 22.

2.1.2 Specific Aims

Specific Aim 1: Determine the optimal formulation for assembly of the rHDL-AMN Nanoparticles

The first specific aim will evaluate the formulation that best encapsulates the α-Mangostin within the rHDL, forming stable and homogenous nanoparticles. Firstly, the fluorescent properties of α-Mangostin will be determined, including the excitation and emission spectra and other fluorescent properties. These properties will allow for the baselines of the free drug that will be compared with the rHDL-AMN particles. In addition, the high degree of the insolubility of α-Mangostin should support the drug's transition into the core of the rHDL and away from the aqueous environment. Next, the rHDL-NP will be characterized by its physical properties, including homogeneity, diameter, and relative stability. Next, the drug loading capacity of the rHDL-AMN will be determined using the properties of α-Mangostin to determine drug incorporation and encapsulation efficiency. Finally, fluorescent measurements, including the fluorescence lifetime and anisotropy, will be used to further characterize the rHDL-AMN particles by comparing them with the free drug. The formulation that gives the best particle qualities will be used to assess the biological effects of the rHDL-AMN.

Specific Aim 2: The therapeutic efficacy of the rHDL-NPs on 2D Prostate Cancer models.

Several cell lines have been chosen to evaluate the biological effects of the rHDL-AMN. The prostate cancer cell line DU145 represents an androgen-independent prostate cancer cell line. PZ-HPV was used to model a non-cancerous epithelial cell line. Other cell lines such as CHO-LDL-A7, H9C2, and CHO-mSRB1 were chosen as controls to characterize the relative expression of

the SR-B1. In addition, the HPC2 and LDL-A7 cell lines were used to illustrate the effects of low the SR-B1 on the rHDL-AMN. These cell lines will have their relative expression of SR-B1 determined to confirm their relative expression of the SR-B1. Cytotoxicity assays using 2D cell cultures will be conducted using varying concentrations of the rHDL-AMN and the free α-Mangostin. Together, the relative SR-B1 expression of the cells and the IC_{50} of the treatments will be compared to determine if the cytotoxic effects of the rHDL-AMN are retained. Due to the SR-B1 mediated transport of the rHDL cargo, high SR-B1 expressing cells should be affected significantly more than low SR-B1 expressing cell lines.

2.1.3. Overall Significance

Modern treatments target the Androgen Receptor (AR) signaling axis due to its influence on promoting cancer progressions. While employment of Androgen Deprivation Therapy (ADT) may confer temporary inhibition of tumor growth, eventually, it promotes the development of castration-resistant prostate cancer (CrPCa). In addition, ADT is associated with many other adverse side effects, such as metabolic disorders and promoting bone metastasis (Chen et al., 2017; Higano, 2003; Salvador et al., 2013; Zacho & Petersen, 2018). New drugs are in development that targets specific aspects of CrPCa, such as splice variants; however, these strategies only prolong ADT usage and remain cytostatic (Liao et al., 2020; Zhou et al., 2010). Outside of ADT, potent and non-specific chemotherapeutics such as taxanes are used against CrPCa tumors. However, patients are often above 65, making prolonged treatment with these agents devastating (Bumbaca & Li, 2018). Therefore, treatments are needed to reduce CrPCa tumor growth by targeting different regulatory mechanisms.

Interest in inhibiting the cell cycle is a common treatment strategy; however, many inhibitors lack specificity. The reported cancer selectivity and its inhibition of CDK4 make α-Mangostin a cancer-

specific cell cycle inhibitor. Furthermore, the inhibition of the CDK4 induces apoptosis and is independent of the AR. Therefore, AR status may not be a barrier to treatment. The FDA has approved several CDK4/6 inhibitors, such as Palbociclib, to treat hormone-refractory cancers (Eggersmann et al., 2019). However, α-Mangostin is a natural compound with the same CDK4/6 inhibition and other possible mechanisms.

The potential for α-Mangostin as a chemotherapeutic is marred by its hydrophobicity. The rHDL has proved to be a promising drug delivery platform for insoluble drugs. Converting the limitation of insolubility that α-Mangostin possesses into enhancing its ability to be delivered systemically via the rHDL. Diversifying the route of administration for α-Mangostin could provide a potent treatment against high SR-B1 expressing CrPCa without targeting the AR. A trojan horse approach can selectively target CrPCa cells while potentially reducing off-target binding with normal cells by taking advantage of this phenotype using the rHDL. As a stable and biocompatible nanoparticle, rHDL has the edge over other nanoparticles that may harbor toxicity, are immunostimulatory, and lack targeting. Because these particles mimic innate HDL, they are metabolized along the same pathways and can navigate systemically without inducing their cytotoxic effects on the body. With the completion of this project, the first steps in creating a serious systemically delivered chemotherapeutic treatment utilizing α-Mangostin will be developed.

2.2. Materials

The α-Mangostin was obtained from Selleckchem (Catalog Number: S3804), Radnor, PA, USA. Egg Yolk Phosphatidyl Choline (EYPC), Free Cholesterol, Sodium Cholate, Uranyl Acetate, and Dimethyl Sulfoxide were purchased from Sigma-Aldrich St. Louise, MO, USA. Apolipoprotein A1 (ApoA1) was received from Abionyx (was Cerenis Therapeutics?) Labege, France. 0.1 cm Quartz cuvettes were obtained from Thor Labs, Newton, NJ, USA. 20,000 MWCO Slide-A-Lyzer

Dialysis Cassettes and PD-10 Sephadex G-25 Medium Desalting Columns were purchased from Thermo-Scientific Waltham, MA, USA. Fluorescence Filters were obtained from Edmund Industrial Optics Barrington, NJ, USA. The Manual Polarizer was obtained from Varian Palo Alto. CA, USA. Keratinocyte Media Promocell Heidelberg, Germany. Corning Costar 96-well plates were purchased from Fischer scientific. Cytiva Fetal Bovine Serum, Gibco DMEM, RPMI, Penicillin-Streptomycin antibiotics, ATCC EMEM, Promocell Keratinocyte Growth Media, DU145, LDL-A7, CHO-mSRB1, PZ-HPV, and H9C2, were purchased from ATCC Manassas, VA, USA. PZ-HPV. Formvar Carbon coated 200 Mesh Copper TEM grids were obtained from SPI West Chester, PA, USA. Malvern Zetasizer 1070 Capillary Cells were purchased from Malvern, Malvern, United Kingdom.

2.3. Methods

2.3.1. Fluorescent Characterization of α-Mangostin

Solution of α-Mangostin was prepared using DMSO, producing a 25 mg/ml stock. For the fluorescent characterization of the free α-Mangostin, aliquots of different concentrations were prepared in 0.1 cm quartz cuvettes. All measurements were conducted at room temperature after the drug was fully thawed. The excitation spectra were measured using the Cary UV-60 spectrophotometer after blanking using only DMSO. The emission spectra were measured using the Cary Eclipse system. The anisotropy was determined by measuring the polarized intensity of the samples. The formula used for the anisotropy is shown in the following formula: $r = ((VV - (G*VH))/((VV + (G*2*VH))$. Finally, the fluorescence lifetime was determined using the Fluoro-Time 300 system (Picoquant, Germany). The samples were excited using a 375nm diode laser (Picoquant, Germany, and the observation wavelength was set to 520nm. The fluorometer was equipped with an ultrafast microchannel plater detecter (MCP) from Hammatsu,

Inc. The fluorescence lifetimes were measured in the magic angle condition, and data were analyzed using the FluoroFit4 Program from PicoQuant, Inc (German) using the multi-exponential fitting model.

2.3.2. Preparation of rHDL α-Mangostin rHDL Particles

A previously established protocol was the basis for formulating the rHDL α-Mangostin nanoparticles (rHDL-AMN). The lipid portion of the rHDL was prepared first by mixing Egg Yolk phosphatidylcholine (EYPC) and free cholesterol dissolved in chloroform. They were evaporated under nitrogen gas and carefully rotated to form a light film of the lipids at the bottom and sides of the glass vial. Sodium cholate was added, and the solution was vortexed until no visible residue was present on the vial walls. Next, α-Mangostin dissolved in DMSO was added directly to the solubilized lipid mixture. For the empty nanoparticle, this step was omitted. Next, the samples were sonicated for five rounds. They were sonicated for 30 seconds and placed on ice for 2 minutes to rest. The sonicator was set to 80 Amps and washed with ethanol and distilled water between each round of sonication. The drugless samples were sonicated first to ensure no cross-contamination with samples containing α-Mangostin.

After sonication, the samples were left on ice until they settled. Next, a magnetic stir bar was added, placed on a magnetic hotplate, and stirred. Dropwise, ApoA1 was added slowly to the mixture with pauses to reduce aggregation and enhance rHDL formation. After the ApoA1 addition, the samples were left to incubate overnight. After incubation, the particles were purified utilizing either the PD-10 column or dialysis in 1X PBS. For purification by the PD-10 column, the sample was passed through the column using distilled water. For dialysis, 1 liter of 1X PBS was used as the solvent; the samples were loaded via syringe into dialysis cassettes. The samples were placed in the 1X PBS for 48 hours. After purification, the samples were centrifuged at 12,000

RPM for 1 hour at 4 degrees Celsius. The samples were then filtered using 0.22 um cellulose syringe filters. These final products were kept in the refrigerator at 4 degrees Celsius until characterization. Figure 23 summarizes the overall formulation schematic.

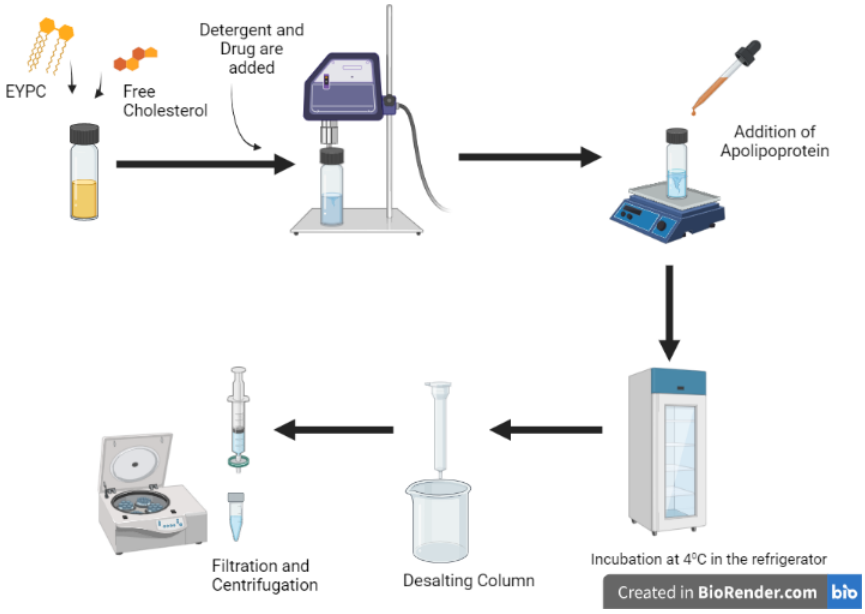

Figure 23. *Preparation schematic for the rHDL.*

2.3.3. Characterization of Physical Properties of rHDL α-Mangostin rHDL Particles

The physical characteristics of the rHDL-AMN were determined using dynamic light scattering (DLS). The Malvern Zetasizer Ultra Particle Analyzer determined the particles' size, homogeneity, and relative stability. Differences in Brownian motion between particles are used to determine the particle's hydrodynamic diameter according to the equation in Figure 24. This size distribution is then reported as the Z-Average; however, the Malvern reports the volume, number, and intensity distributions (Malvern, 2014). Next, the homogeneity or polydispersity index (PDI) is reported based on the standard deviation of the reported hydrodynamic diameters, as seen in Figure 25. A PDI value below 0.2 is considered relatively homogenous under the standards of the FDA.

$$d(H) = \frac{kT}{3\pi\eta D}$$

where:-

$d(H)$ = hydrodynamic diameter

D = translational diffusion coefficient

k = Boltzmann's constant

T = absolute temperature

η = viscosity

Figure 24. *The Formula for the calculation of the hydrodynamic diameter.*

$$\mathrm{PDI} = \left(\frac{\sigma}{R_\mathrm{d}}\right)^2$$

Figure 25. *The Formula for the calculation of the Polydispersity Index. The standard deviation of the average hydrodynamic diameter is divided by the average diameter.*

However, it is acceptable to have a PDI value below 0.3 for lipid-based nanoparticles due to their tendency to aggregate (Danaei et al., 2018). The PDI can indirectly measure a particle sample's stability while assessing the particles' quality and preparation. Changes in the PDI can suggest that particle samples are degrading, fusing, or aggregating. Finally, the zeta potential can give information on the relative stability of the particle in its current solvent. The zeta potential is measured by the charge difference between the particle's surface and the solvent, as seen in Figure 26 (Kumar & Dixit, 2017). More specifically, the surface of a nanoparticle displays some degree of charge that attracts the opposing charges from the aqueous solvent, forming a layer called the Stern layer. The difference in charge between the Stern layer and the solvent is measured as the zeta potential in voltage. A higher magnitude of the zeta potential confers stronger repelling forces and, therefore, a reduced affinity for aggregation. A particle with a zeta potential below +/- 25 mV will eventually aggregate, while above +/- 30 mV is considered stable for nanoparticles. However, these measurements depend on the solvent conditions; therefore, careful considerations must be

made when preparing the samples for measurements. Salt, concentration, and pH are all factors that may skew the values of the zeta potential (Kumar & Dixit, 2017).

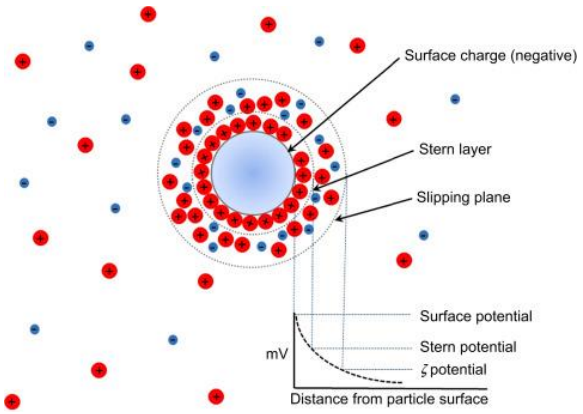

Figure 26. *The Zeta Potential is the relative difference in charge between the stern layer and the surrounding solvent (JASCO, 2022; Pate & Safier, 2016).*

Measurements of the rHDL-AMN and Empty rHDL samples were conducted using plastic cuvettes. Samples were filtered using 0.2 um filters and diluted to 1:15 using Di water before measuring their properties. Samples were measured only at room temperature. The same dilutions were prepared for the zeta potential; however, Malvern 1070 folded capillary cartridges were used.

2.3.4. Transmission Electron Microscopy

The Transmission Electron Microscope (TEM) was used in addition to the DLS to image and directly report the sizes of the rHDL samples. Samples were prepared on carbon-silicon TEM 200 grids using a 1% uranyl acetate staining protocol. The samples were initially diluted to 1:100; however, the second trial used a more extensive 1:1000 dilution. Next, several microliters of the samples were added to the grid to cover the entire surface. After 5 minutes, the samples were stained using the 1% Uranyl acetate and left to dry overnight. Finally, the prepared grids were imaged using the JEM 200 TEM at 200 kV.

2.3.5. Fluorescent Characterization of rHDL-AMN

The rHDL particles were characterized using the identical 0.1cm quartz cuvettes from Thor Labs. A standard curve was prepared using the known concentration of the stock solution and to record their absorbances at 375nm. The rHDL-AMN samples were diluted by 1:10 using 1X PBS, and their absorbance values at 375nm were recorded. Empty rHDL particles were used to remove the scattering profile of the particles from the rHDL-AMN measurements producing the correct spectra. An inflated value for the drug concentration may be reported without removing the scattering profile, thus affecting biological studies. The concentration of the rHDL-AMN would then be calculated using the standard curve once the dilution factor was considered. The encapsulation efficiency was determined by dividing the concentration of α-Mangostin present in the rHDL-AMN sample by the micromolar concentration of α-Mangostin initially added to the formulation, as shown in Figure 27.

A set of filters were employed to reduce signal noise. A 495 long-pass filter was placed near the detector, and a 400 short-pass filter was placed at the excitation lamp. Due to the additive properties of fluorescence, the emission of the empty rHDL was used to correct the spectra of the rHDL-AMN. The scattering profiles between the rHDL-AMN and the empty rHDL were matched before reading the emission intensities at 520nm.

The fluorescence lifetime (FLT) measurements of the rHDL samples were measured using Fluor-Time 300 with the same conditions, equipment, and set-up as the α-Mangostin characterization. The intensity decay was fit using a tail fitting on the Origin software. The rHDL-AMN sample was split by volume into two glass vials for the disruption experiment. Both samples were

$$\text{Encapsulation efficiency}\left(\text{EE}\right)=\frac{\text{amount of total loaded drug}}{\text{total amount of drug}}\times 100$$

Figure 27. *The Formula for the calculation of the Encapsulation Efficiency (Pu et al., 2020).*

lyophilized using the Labconcno Freezone12 Lypholizer. The samples were placed at -80 Degrees overnight and then were lyophilized for 24 hours. The samples were resuspended in either Di-water or DMSO before the measurements. After adding the solvent, the samples were vortexed until no residue was visible on the vial walls before being measured by the Fluoro-Time 300.

2.3.6. Cell Lines

The cell line DU145 was chosen as the 2D cancer model to model later-stage prostate cancers. In addition, the immortalized prostate epithelial cell line PZ-HPV was selected for the control cell line. Both cell lines have been used previously for rHDL drug delivery studies (Lacko et al., 2012; Lacko et al., 2002). The DU145 and PZ-HPV were reported as relatively high and low expressions of the SR-B1. Furthermore, the DU145 is an androgen-independent cancer cell line, therefore modeling the later stage CrPCa. Therefore, additional cell lines were chosen as controls for their expression of the SR-B1. The positive controls included the liver carcinoma Hep-G2 and the transinfected overexpressor of the SR-B1 CHO-mSRB1. The negative control included CHO-LDL-A7, transinfected to express low levels of SR-B1, and the cardiomyocyte cell line H9C2. Cells were cultured and maintained in 10% FBS and 1% Pen-Strep in their respective media. The DU145, Hep-2G, CHO-LDL-A7, and CHO mSRB1 were cultured in complete EMEM. The H9C2 were cultured in complete DMEM, and the PZ-HPV were cultured in completed special Keratinocyte media with BPE and EGF purchased from Gibson and Promocell.

2.3.7. SR-B1 Expression

The relative expression of the SR-B1 was determined through the usage of the JESS automated western blot system by ProteinSimple. The 13-lane version of the detection kit for proteins between 12-230kDa was used. Pellets were collected and washed in ice-cold 1X PBS and stored under -80 degrees Celsius until the preparation of the cellular lysate. A RIPA buffer and

phosphatase inhibitor solution were prepared to process the lysate. The protein concentration of the lysates was quantified using the Pierce Bicinchoninic Acid (BCA) assay, where bovine serum albumin served as the standard. The 13-wells were loaded with the sample and reagents per the kit protocol. The SR-B1 primary antibody (EPR20190) was used at a 1:100 dilution. The actin primary antibody (A5441) was used with a dilution of 1:400. The Protein simple kit provided the secondary antibodies for anti-rabbit and mouse. The secondary antibodies were used as prepared without dilution. Data analysis was done through the usage of Compass Software. Protein normalization was done using actin concentration to determine the relative expression of SR-B1.

2.3.8. Cytotoxicity

Cells were plated in 96-plates and treated with varying dosages of the free α-Mangostin, rHDL-AMN, and Empty rHDL particles. Five thousand cells per well were plated in their complete media for 24 hours. Cells were observed under a microscope to determine if they had adequately attached to the bottom of the wells. Next, the complete media was removed, and the cells were washed with 1X PBS. Treatments of varying concentrations were prepared individually in microcentrifuge tubes using a serum-free medium before being added to each well. In addition, empty wells without cells were treated to be used as blanks to remove the absorbance values of the media and the treatment. Cells were incubated for 48 hours at 37 degrees Celsius at 5% CO_2.

Cell viability was determined using the Cell Counting Kit 8 by Dojindo (CCK-8). Cells were incubated with 10uL of the CCK-8 reagent for 2 hours. Next, the plates were placed on a rocker inside an incubator to enhance the reagent mixing in the wells. Finally, the plates were read in the Biotek Cystation 3 plate reader using a wavelength of 450nm. The IC_{50} values were fit and calculated using the AAT Bioquest online calculator.

Chapter 3

Results

3.1. Specific Aim #1

3.1.1. Characterization of the Fluorescent Properties of α-Mangostin

As of the time of the study, no published information regarding the fluorescent properties of α-Mangostin is available. However, aromatic structures typically exhibit some degree of fluorescent properties. The parent compound is a xanthone, a xanthene derivative, as shown in Figure 28. Many popular fluorescent dyes such as fluorescein, rhodamine, and rose bengal contain xanthene as their parent structures (Neckers & Valdes-Aguilera, 1993). Because both parent molecules are

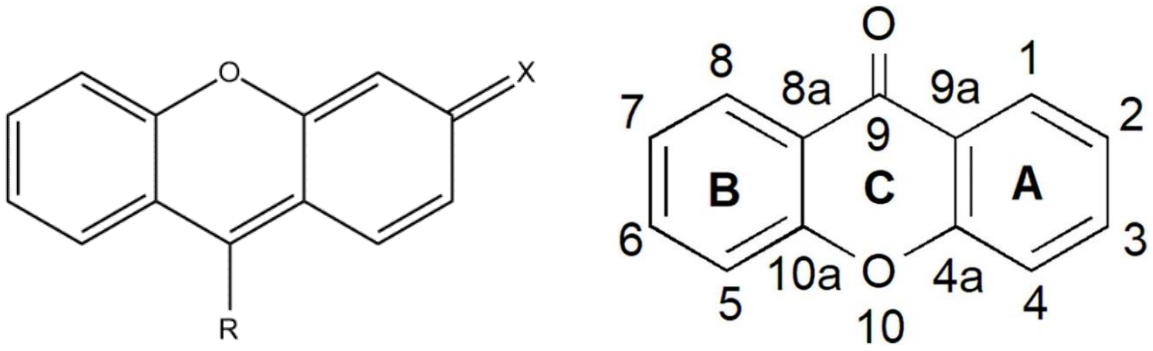

Figure 28. *(Left) Structure of Xanthenes (Imiołek, 2015)* ***Figure 7*** *(Right) Molecular structure of Xanthones (Remali et al., 2022).*

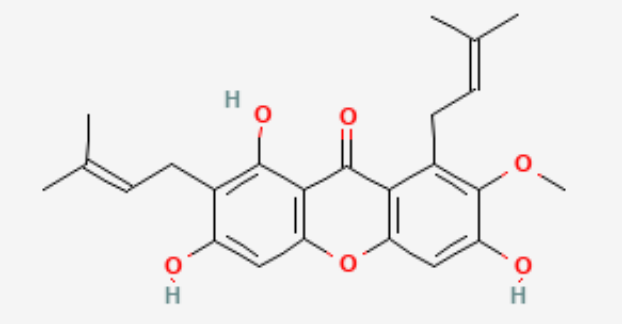

Figure 29. *The 2D Structure of α-Mangostin (NCBI, 2022a).*

enclosed in conjugated ring systems, α-Mangostin may possess fluorescent properties, as depicted in Figure 29. These characteristics could provide a wealth of information regarding the presence

and the environment. Furthermore, changes in these properties between the free and the rHDL formulations can suggest encapsulation without disrupting the particles.

Samples of α-Mangostin were prepared in DMSO and placed into a 0.1 cm quartz cuvette. First, the excitation spectra extended from 300nm to 405nm with a maximum of 320nm. Additionally, a characteristic small peak at 350nm was present. Next, using 375nm as the excitation wavelength, the emission spectra stretched from 450nm to 650nm with a maximum of 521nm. The excitation and emission spectra of the free α-Mangostin in DMSO are graphed below in Figure 30. Together these two spectra reveal a significant Stoke's shift of nearly 200nm between each maximum.

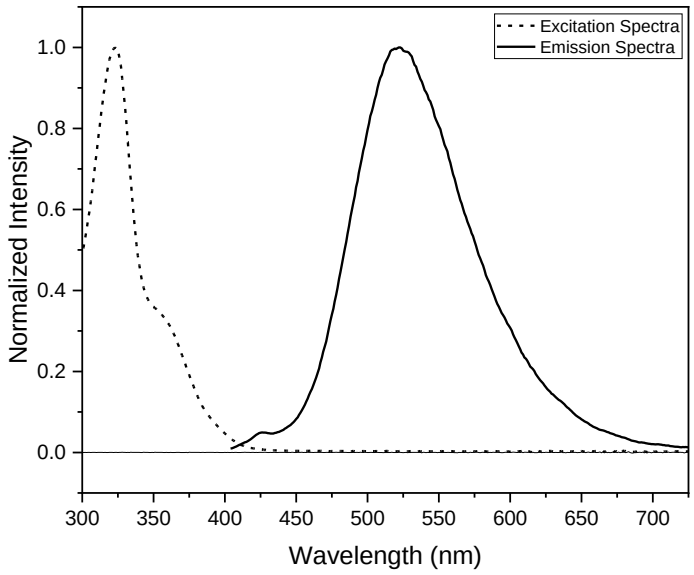

Figure 30. *The Excitation and Emission spectra of α-Mangostin in DMSO.*

Using the Cary Eclipse, the anisotropy of the α-Mangostin in DMSO was calculated using the polarized emission intensities produced when excited at 375nm. An r value of 0.06 at 520nm shows a high degree of free molecular rotation, as shown in Figure 31.

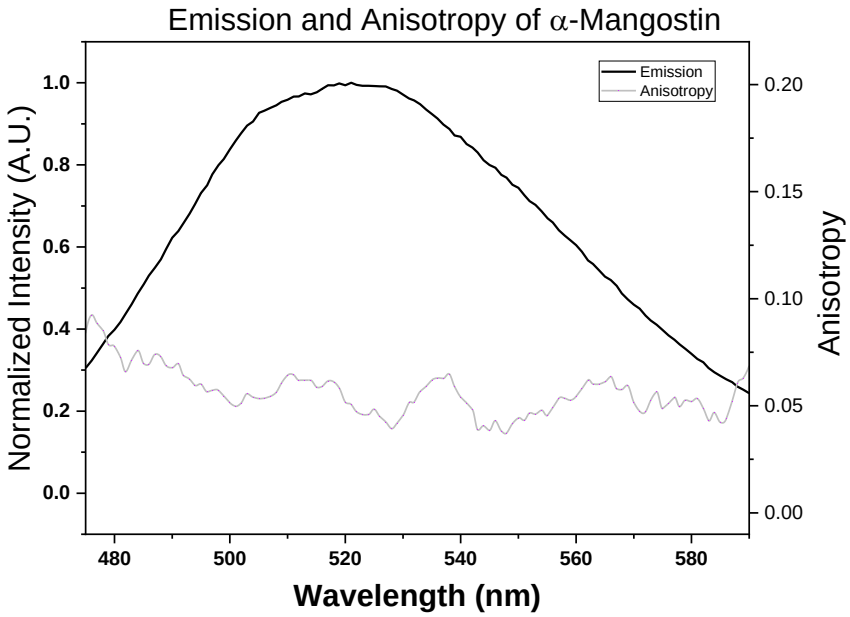

Figure 31. *The Anisotropy overlayed on the Emission spectrum.*

Finally, the Fluorescence Lifetime (FLT) amplitude for the free in DMSO α-Mangostin was 1.56ns using a two-exponential fit, as shown in Figure 32. The components of the FLT were composed primarily of a component that averaged 1.68ns and a short component of 0.35ns. Together the data on the free α-Mangostin will serve as a baseline for comparison with the rHDL-AMN samples.

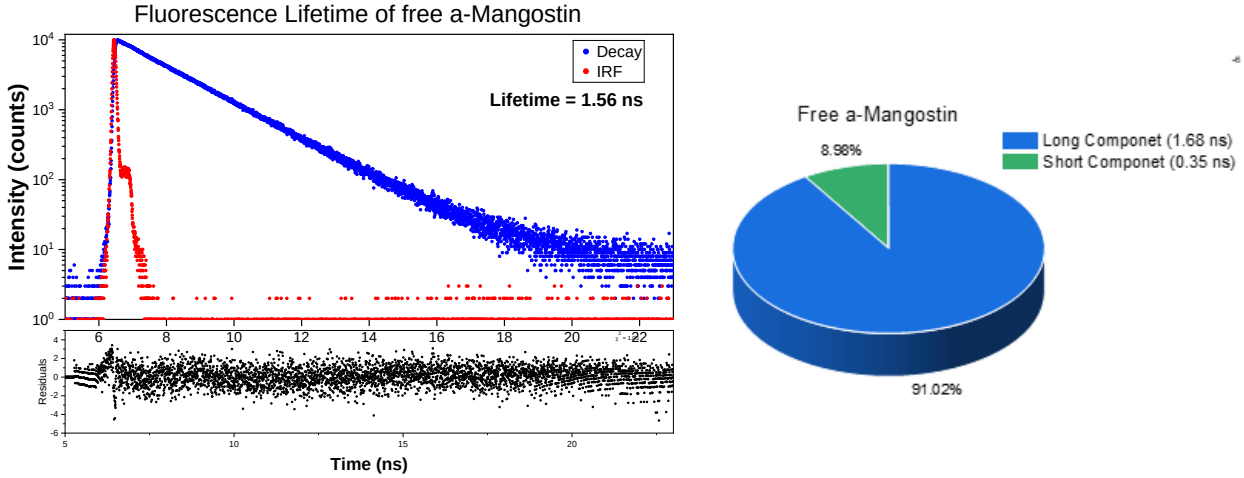

Figure 32. (Left) *The intensity decay of α-Mangostin in addition to the average fluorescence lifetime* ***(Right)*** *The pie chart depicts the composition of the lifetime curve.*

3.1.2. Physical Characterization of the rHDL-AMN Nanoparticle

A previously established protocol was used for the initial formulation as a starting point for the rHDL-AMN nanoparticles. An initial concentration of 0.5mg/ml of α-Mangostin was used to reduce the amount of drug lost during the optimization of the methods and formulation. Empty rHDL nanoparticles were produced to blank the rHDL-AMN samples, provide a quality assessment of the procedures, and serve as vehicle control in the in-vitro experiments. After the rHDL-AMN particles were assembled, they were dialyzed in 1X PBS for 48 hours at 4 degrees Celsius. The physical properties of the particles were assessed using a 1:15 dilution in Di Water. Table 3 summarizes the samples produced by the protocol that gave the most favorable physical properties.

Table 3. *Summary of the rHDL-AMN phyiscal particle characteristics.*

	PDI	Size by Intensity (nm)	Size by Number (nm)	Zeta Potential (mV)
Empty rHDL N=4	0.20 +/- 0.027	95.62 +/- 20.29	40.04 +/- 12.90	-24.43 +/- 12.5
rHDL-AMN N=7	0.19 +/- 0.016	85.14 +/- 15.08	38.99 +/- 9.43	-29.47 +/- 8.3

The PDI values for both samples fit within NIH-established guidelines for nanoparticles. Values below 0.2 are generally recommended; however, a PDI below 0.3 is acceptable for lipid-based particles like these. The intensity distribution shows larger particle diameters; however, due to these lipid nanoparticles, there could be skewed due to aggregation. The number distribution is within the range of intrinsic HDL particles. Both size distributions show similar sizes between the empty and the rHDL-AMN nanoparticles. Finally, the zeta potentials depict moderate stability and resistance to aggregation with an absolute value near 30mV.

3.1.3. Transmission Electron Microscopy

To further elucidate the physical characteristics of the rHDL samples, transmission electron microscopy (TEM) was employed to image the particles. Nanoparticles were prepared using 1% Uranyl Acetate the day prior to imaging. Both Empty rHDL, human HDL, and rHDL-AMN samples were imaged using the same settings for the JEM-2100 Electron. The first set of images was produced using fresh diluted samples to 1:100, as shown in Figure 33. With this dilution, the Empty rHDL particles were visible; however, the rHDL-AMN appeared very concentrated, making accurate determinations about the size and shape difficult. Next, the Human HDL was imaged to serve as a reference for the shape and structure of the HDL. However, it too remained very concentrated.

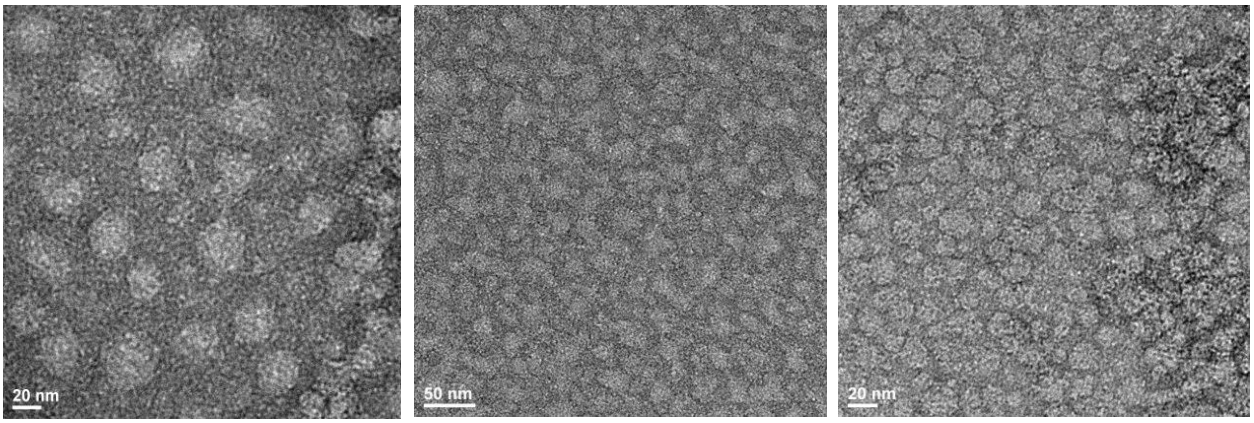

Figure 33. *TEM images of fresh rHDL Nanoparticle diluted 1:100* ***(Left)*** *Empty rHDL* ***(Middle)*** *rHDL-AMN* ***(Right)*** *Human HDL.*

A second trial used two-week-old rHDL samples with a higher dilution of 1:1000 to further improve the clarity of the particles. Again, no additional processing such as filtering or centrifugation was done before preparing the samples for the TEM. Figure 34 shows both the empty rHDL and the rHDL-AMN samples. This time, the dilution to 1:1000 improved clarity for the empty rHDL; however, the high concentration of the rHDL-AMN particles makes discerning

the shapes difficult. Figure 35 shows the lower magnification to show the shapes and structures of the empty rHDL.

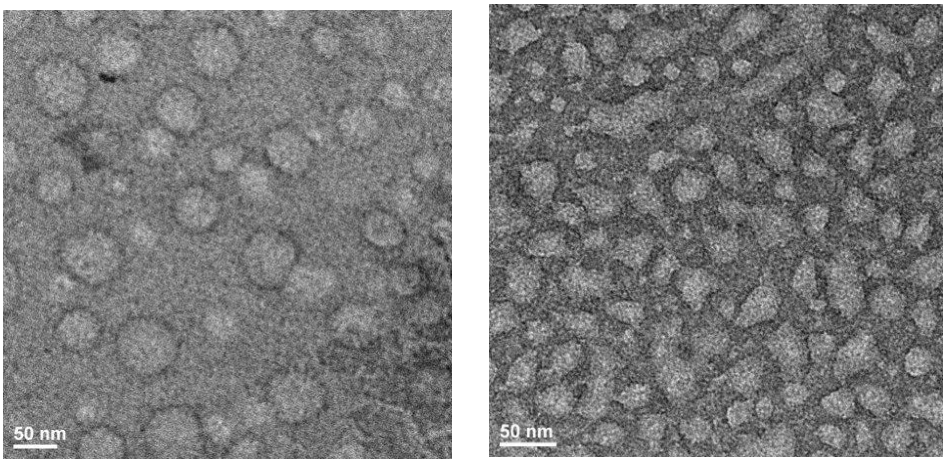

Figure 34. *Samples after two weeks* ***(Left)*** *Empty rHDL* ***(Right)*** *rHDL-AMN.*

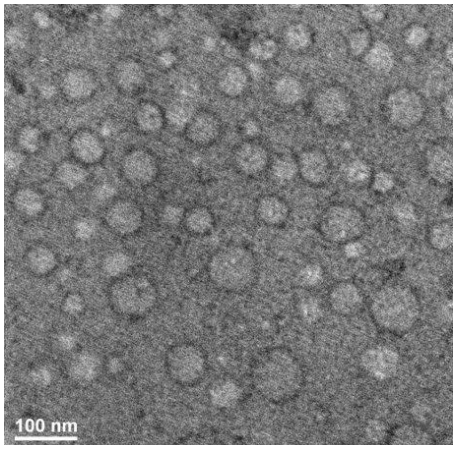

Figure 35. *Empty rHDL after two weeks. The sample was diluted to 1:1000. Note the lower resolution.*

3.1.4. Encapsulation Efficiency of the rHDL-AMN Nanoparticles

The initial addition of the α-Mangostin into the resuspended solution of phospholipids, free cholesterol, and sodium cholate caused significant precipitation of the α-Mangostin, as seen in Figure 36 (left). Vortexing this mixture resulted in large yellow aggregations that would disappear only after sonication. Figure 36 (middle) shows the sample after adding ApoA1, which caused a slight reduction in opacity. After dialysis, centrifugation, and filtering, the final result is shown in Figure 36 (right).

The concentration of the α-Mangostin within the rHDL-AMN was determined by measuring the absorbance of the samples. First, samples were diluted by 10 to reduce signal saturation. Next, the empty rHDL samples were used to remove the scattering profile of the rHDL-AMN. Next, a standard curve converted the absorbance values into micromolar concentrations. Finally, the concentration was divided by the initial addition of α-Mangostin added. These results are summarized in Table 4.

Figure 36. (Left) *Initial Addition of the α-Mangosint to the lipid solution containing Sodium cholate, Cholesterol, and phospholipids.* ***(Middle)*** *After sonication and adding ApoA1* ***(Right)*** *After dialysis, centrifugation, and filtration.*

Table 4. *Encapsulation Efficiency of the rHDL-AMN samples.*

N=6	Encapsulation Efficiency
0.5 mg/ml rHDL-AMN	44% +/- 15%

An intense spectrum that strongly resembles the excitation spectra α-Mangostin is found in the rHDL-AMN samples, as shown in Figure 37 (Top). In addition, the empty rHDL particles produced a scattering profile used to remove the scattering profile of the rHDL-AMN, as shown in Figure 37(Bottom).

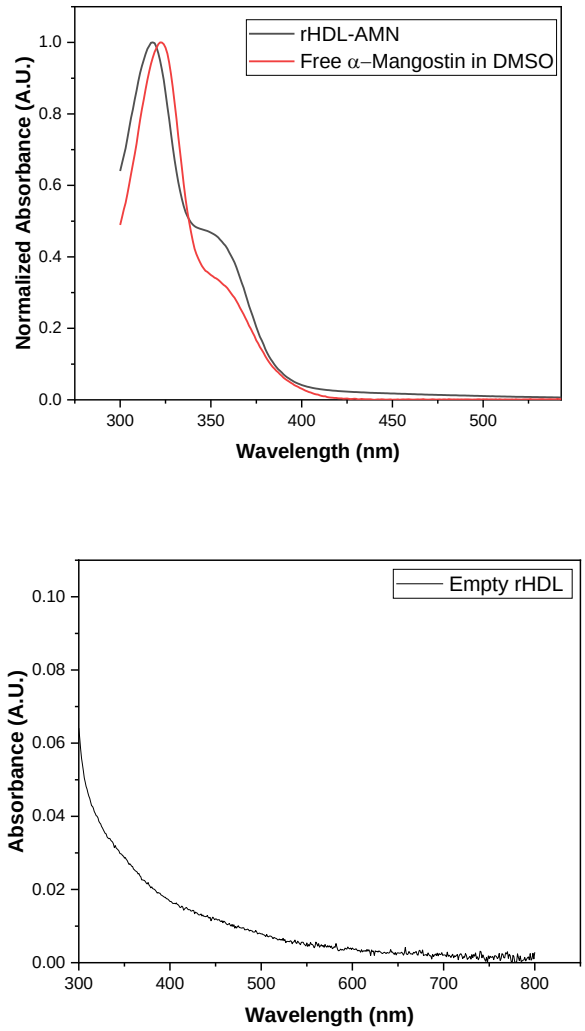

Figure 37. (Top) *Excitation spectrum of the rHDL-AMN and free α-Mangostin* ***(Bottom)*** *Excitation spectrum of the Empty rHDL particles. Note the difference in scale.*

Samples passed through the PD-10 gravity column were separated into several fractions by molecular weight. Fractions 2 and 3, according to the manufacturer, contain components of the sample with molecular weights associated with proteins. Lipid micelles and unincorporated α-Mangostin will either elute in later fractions or remain trapped in the column. Samples of the fraction were deposited into a 96-well plate and read using 375nm as the excitation source on the

BioTek Cytation 3 plate reader. Figure 38 shows the absorbance values for each of the fractions. The highest absorbance value was found in the second fraction associated with rHDL.

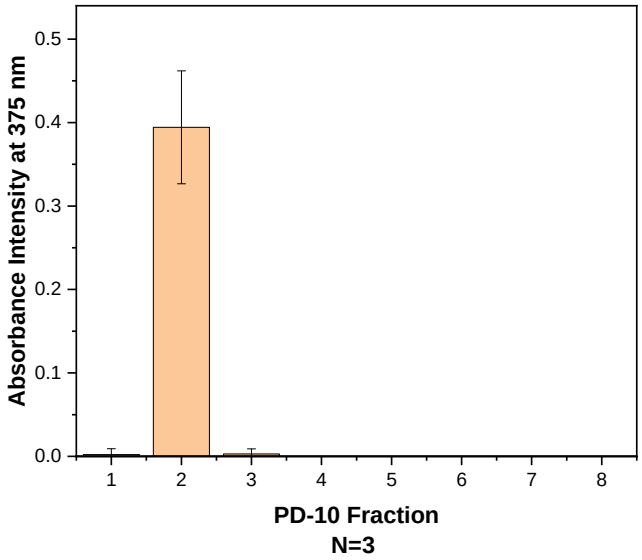

Figure 38. *The absorbance of each PD-10 Fraction using 375nm as the excitation source.*

3.1.5. Drug Loading Study

The protocol and formulation in this study were adopted from previous experiments utilizing different drugs. A recommended working range of 0.5 mg/ml was used for the initial trials; however, altering the initial concentration may affect the encapsulation of α-Mangostin and the quality of the particle. Therefore, a drug loading study was conducted to determine the maximum amount of α-Mangostin encapsulated within the rHDL. An initial concentration of 1.0 mg/ml, double the standard formulation, was used. Due to the number of samples, the PD-10 desalting column removed the unbound components and salts present in the samples. The results of this study are summarized below in Table 5.

Table 5. *Physical characterisitcs of the rHDL-AMN samples. Note that the reported size is the number distribution.*

N=3	PDI	Size (nm)	Zeta Potential (mV)	Encapsulation Efficiency
Empty rHDL	0.38 +/- 0.08	30.0 +/- 10.7	-33.7 +/- 2.4	-
0.5 mg/ml rHDL-AMN	0.25 +/- 0.04	24.1 +/- 19.9	-26.6 +/- 3.5	40% +/- 0.08%
1.0 mg/ml rHDL-AMN	0.32 +/- 0.03	9.4 +/- 2.1	-30.4 +/- 4.7	48% +/- 0.3%

3.1.6. Particle Stability

While the zeta potential indicates a relatively high degree of stability, it does not report how these physical properties may change over time. Therefore, samples of rHDL-AMN were prepared using the 0.5mg/ml formulation, dialyzed for 48 hours, and filter-sterilized. A 1:15 dilution of the samples were prepared and characterized. The remaining samples were stored at 4 degrees Celsius. After 43 days, the samples were recharacterized without filtering and re-filtered using a 0.2um filter. Together these are summarized in Table 6.

Beginning with the changes in the PDI, the rHDL-AMN samples had a higher PDI of 0.25 after 43 days shown in Figure 40. However, filtering returned the PDI to values before the sample was stored. In Figure 41, the average diameter of the rHDL-AMN decreased; however, filtering returned it to a value similar to Day 0. Finally, Figure 42 shows the changes in the zeta potential values. After 43 days, there was a notable increase in the zeta potential that remained elevated after filtering. The particle characteristics remained almost identical for the empty rHDL sample besides an increased zeta potential after 43 days. The empty and the rHDL-AMN had elevated values for the zeta potential that did not resemble the zeta potentials found during Day 0.

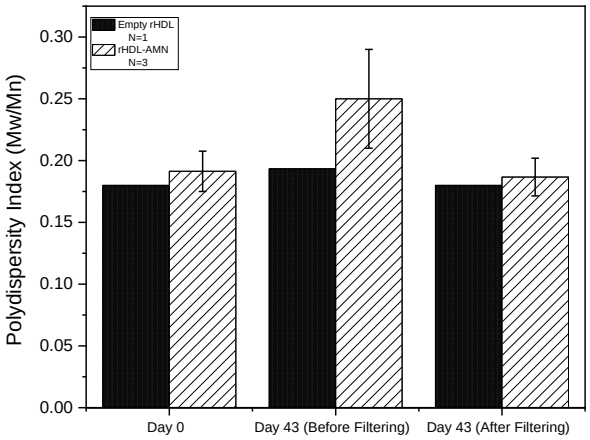

Figure 39. *Changes in the PDI after 43 days.*

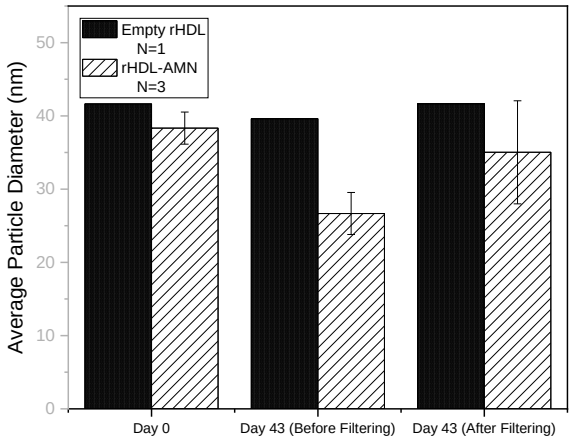

Figure 40. *Changes in the average particle diameter after 43 days.*

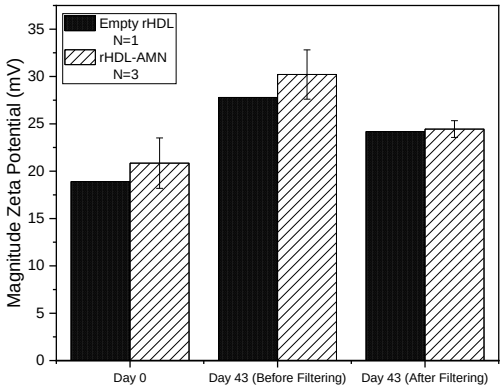

Figure 41. *Changes in the Magnitude of the Zeta Potential after 43 days.*

Table 6. *Summary of the changes in the phyiscal characteristics of the rHDL samples.*

Empty rHDL N=1	PDI	Particle Diameter (nm)	Zeta Potential (mV)
Day 0	0.18	41.64	-18.91
Day 43 (Before Filtering)	0.193	39.6	-27.79
Day 43 (After Filtering)	0.184	41.6	-24.19
rHDL-AMN N=3	PDI	Particle Diameter (nm)	Zeta Potential (mV)
Day 0	0.191 +/- 0.16	38.33 +/- 2.19	-20.85 +/- 2.67
Day 43 (Before Filtering)	0.25 +/- 0.04	26.67 +/- 2.87	-30.21 +/- 2.60
Day 43 (After Filtering)	0.187 +/- 0.02	35.03 +/- 7.03	-24.45 +/- 0.88

3.1.7. Anisotropy Measurements of the rHDL-AMN Particles

Anisotropy changes between the free α-Mangostin and the rHDL-AMN can suggest that encapsulation of α-Mangostin has occurred. The anisotropy of the free α-Mangostin was calculated previously to be 0.06 and will act as the baseline. Due to possible interference from the shell of the rHDL itself, the rHDL-AMN produced high anisotropy values. Due to the additive property of fluorescence emission, samples of empty rHDL were used to subtract the interference from the rHDL shell. The empty rHDL was matched by the scattering profiles to the rHDL-AMN, and their polarized emission intensities were recorded, leaving only the α-Mangostin. These results are summarized in Table 7.

Table 7. *Anisotropy values of the rHDL-AMN samples from the loading studies.*

N=3	Anisotropy
α-Mangostin	0.06 +/- 6E-4
0.5 mg/ml rHDL-AMN	0.32+/- 0.05
1.0 mg/ml rHDL-AMN	0.25 +/- 0.02

3.1.8: Changes in Fluorescence Lifetime and Anisotropy After Disruption

A disruption experiment was conducted to determine if any changes in the lifetime occurred due to encapsulation by rHDL. A sample was prepared following the 0.5mg/mL formulation, split by volume into halves, and then lyophilized. One of the halves was resuspended in DMSO and the other in 1X PBS. As previously determined, the Lifetime of the free α-Mangostin was determined to be about 1.56ns, as shown in Figure 42 (Top). However, the half resuspended in 1X PBS showed a markedly decreased FLT value, reduced by more than 50% to 0.72ns, and there was a different make-up of the intensity decay curve Figure 42 (Middle). The short component now dominated, while a component of 5.62ns appeared, possibly due to the protein and lipids. The other half was resuspended in DMSO, disrupting the particles and releasing the free α-Mangostin back into the solution. The FLT returned to a similar anisotropy as the free drug with a value of 1.59ns Figure 42 (Bottom). Together these are summarized in Table 8.

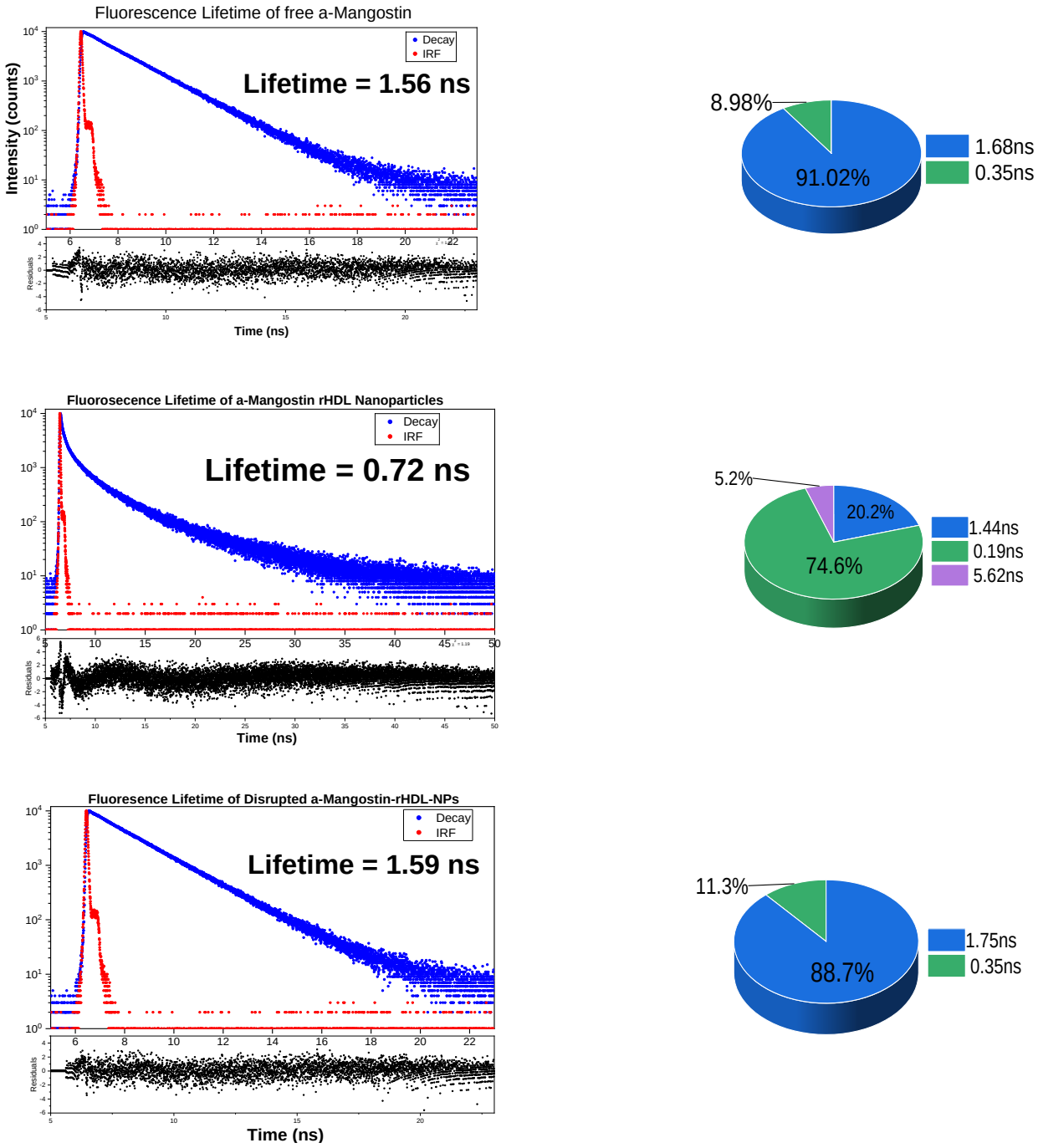

Figure 42. (Top) *Fluoresence Lifetime of the α-Mangostin.* ***(Middle)*** *The Fluorescence Lifetime of the rHDL-AMN particles.* ***(Bottom)*** *The Fluorescence Lifetime of the DMSO disrupted rHDL.*

Table 8. *Fluoresence Lifetimes of the free drug, rHDL-AMN and DMSO disrupted rHDL-AMN.*

	Fluorescence Lifetime (ns)
Free α-Mangostin	1.56
rHDL-AMN in 1X PBS	0.72
Disrupted rHDL-AMN in DMSO	1.59

After disruption, the excitation spectra of the samples were recorded. The spectra of the 1X PBS resuspended sample had the same shaped curve. However, there was an extensive scattering profile due to a lack of filtering. In addition, the disrupted rHDL-AMN in DMSO exhibited a shift in its spectra. The lipids and protein in the DMSO or the formation of adducts in the solution could cause this shift.

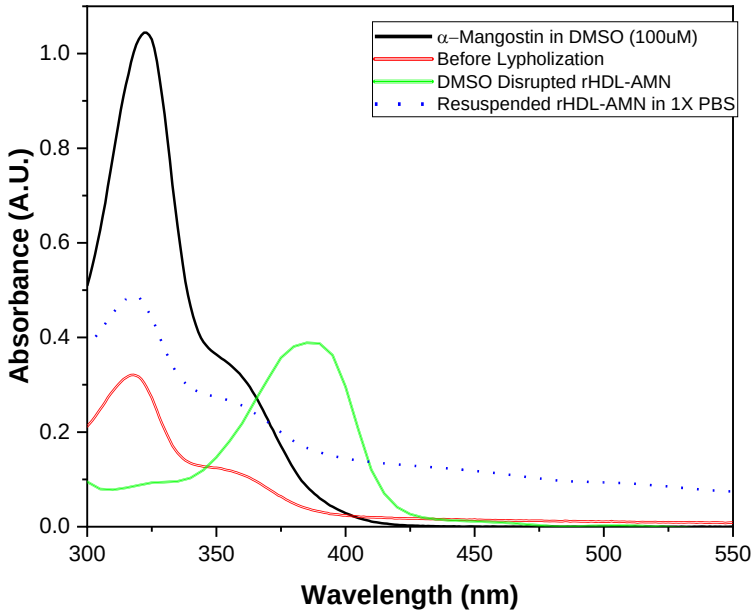

Figure 43. *Excitation spectra of the rHDL-AMN, Empty rHDL, α-Mangostin, and the disrupted rHDL nanoparticles.*

The anisotropy of the disrupted rHDL was measured to confirm that the drug was released back into the solution. The r was calculated to be 0.63, which is very close to the anisotropy of the free drug. These anisotropy values are summarized in Table 9.

Table 9. *Summary of the Anisotropy values of the free drug, rHDL-AMN and the disrupted rHDL-AMN.*

N=1	Anisotropy
α-Mangostin	0.058
rHDL-AMN (0.5mg/ml)	0.32
Disrupted rHDL-AMN	0.063

3.1.9. Summary of Specific Aim 1

In summary, for specific Aim 1, beginning with the fluorescent characteristics of α-Mangostin, fluorescent properties were determined, including the excitation and emission spectra, the anisotropy, and the fluorescence lifetime. A modified rHDL protocol based on an existing formulation was used to include α-Mangostin and produce rHDL-AMN. The rHDL-AMN samples were physically characterized by the DLS and through the fluorescent properties of α-Mangostin. The anisotropy and the FLT of the free and rHDL-AMN were measured. Additionally, the rHDL-AMN particles were disrupted and measured. Finally, a loading study was conducted to optimize the formulation and a stability study to determine the effects of storage.

3.2. Specific Aim #2

3.2.1. Characterization of SR-B1 Expression

The biological effects of the rHDL nanoparticles are dependent on the SR-B1 expression of the cell lines. High expression of the SR-B1 should lead to higher susceptibility to the loaded rHDL particles. Conversely, cells with low expression should protect the cells from the rHDL-AMN. The automated western blot system, JESS, was employed to determine the relative expression of

the SR-B1. After lysate preparation, samples of the cells were loaded based on protein concentration. After the run, the expression was normalized by dividing the intensity of the SR-B1 bands by the actin expression. Figure 43 shows the relative SR-B1 expression between the different cell lines. The Hep-G2, MDA-M8, and CHO-mSRB1 served as positive controls for significant SR-B1 expression. CHO-LDL-A7 and H9C2 served as the negative control due to the low expression of SR-B1. Interestingly, the PZ-HPV, which was chosen to represent a normal cell line, overexpresses the SR-B1. This cell line has been used previously to show the protective features of the rHDL. However, the currently characterized cells express the SR-B1 more than the PCa cell line DU145. These results are summarized in Figure 45. (If H9C2 works, add them to the graph)

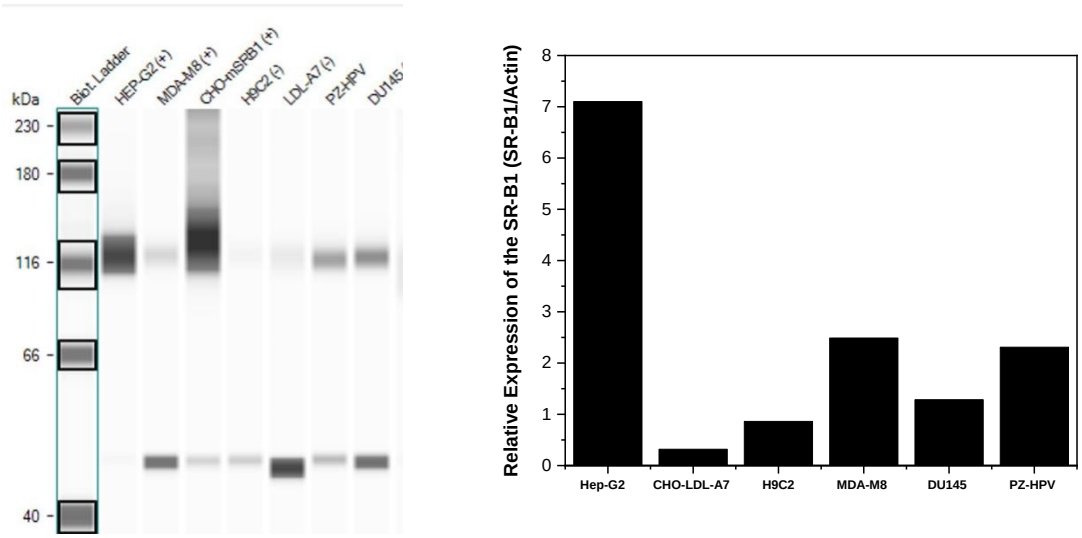

Figure 44. (Left) *Western Blot of the SR-B1 expression for each cell line.* ***(Right)*** *Relative expression of the SR-B1 normalized by actin expression. Note: CHO-mSRB1 is not shown due to a high expression.*

treatments were determined using Cytotoxicity Assays and 2D cell lines. Equimolar concentrations of the rHDL-AMN and the free α-Mangostin were administered, while a volume equal to the rHDL-AMN was used for the empty rHDL treatment. Five thousand cells were plated per well in

a 96-well plate and left to incubate in complete media for 24 hours. Afterward, the cells were inspected, washed with 1X PBS, and serum-free media containing the treatments were added. Treated cells were incubated for the specified time, and the CCK-8 Cell Viability reagent was added. After two hours, the plates were read under the BioTek Cystation 3.

Table 10 shows the IC_{50} values after 24 hours of incubating with treatments of the rHDL-AMN and the α-Mangostin. The effects of the free α-Mangostin showed immediate toxicity to the DU145. However, the rHDL-AMN had little effect initially observed. However, cytotoxicity was observed after 48 hours, as shown in Figure 46 and summarized in Table 11. The empty particles reported no cytotoxic effects even after 48 hours.

Table 10. *DU145 IC_{50} Values of the rHDL-AMN and Free α-Mangostin after 24 hours.*

Cytotoxicity 24 Hours	
N=1	**IC50**
α-Mangostin	1.41
rHDL-AMN	249.9

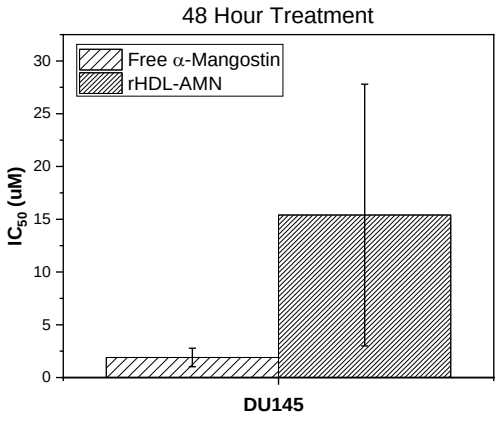

Figure 45. *DU145 IC_{50} values after 48 hours.*

Table 11. *DU145 IC_{50} values after 48 hours of treatment.*

Cytotoxicity 48 Hours	
N=3	IC50
α-Mangostin	1.9 +/- 0.88
rHDL-AMN	15.4 +/- 12.4

3.2.3: PZ-HPV Cytotoxicity

Next, the same treatments were replicated using the PZ-HPV cell lines, which were found to have a higher expression of the SR-B1. After 48 hours, there was cytotoxicity with treatments of the rHDL-AMN and free α-Mangostin; however, not with the empty rHDL particles. The IC_{50} values are found in figure 45. Despite PZ-HPV not being a cancerous cell line, the α-Mangostin showed considerable cytotoxicity similar to the DU145. The rHDL-AMN additionally showed cytotoxicity against PZ-HPV. To assess the variance between the rHDL-AMN samples, one of the trials used the same rHDL-AMN sample, revealing that a degree of variability existed between different samples accounting for the standard deviation.

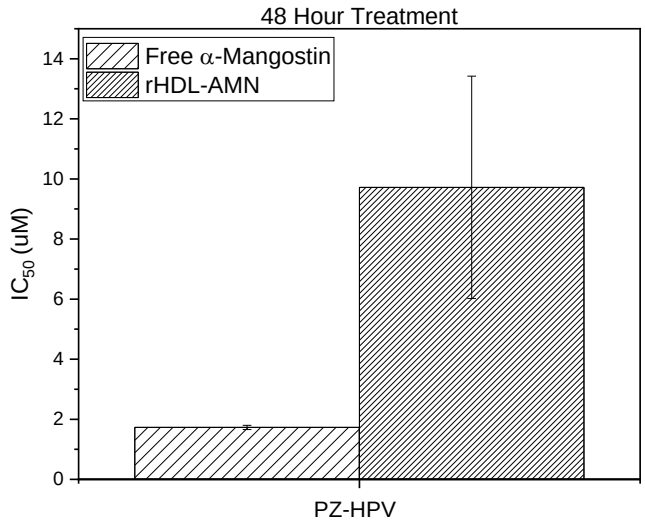

Figure 46. *PZ-HPV IC_{50} values after 48 hours.*

Table 12. *PZ-HPV IC_{50} Values after 48 Hours.*

Cytotoxicity 48 Hours	
	IC50
α-Mangostin N=2	1.73 +/- 0.07
rHDL-AMN N=3*	9.72 +/- 3.70

*The same rHDL-AMN sample was used twice

3.2.4. Low SR-B1 Expression and Cytotoxicity

Because the rHDL binds to the SR-B1, the high expression should confer vulnerability to SR-B1 expressing cells. Conversely, the low expression should reduce cytotoxicity to the rHDL-AMN. Therefore, two low SR-B1 expressing cell lines, H9C2 and LDL-A7, were used to determine if the rHDL-AMN could protect the cells from exposure to the α-Mangostin. According to the SR-B1 expression, H9C2 had a relatively lower expression of the SR-B1 compared to the DU145. The comparison of IC_{50} values is shown in Figure 48 and Table 13.

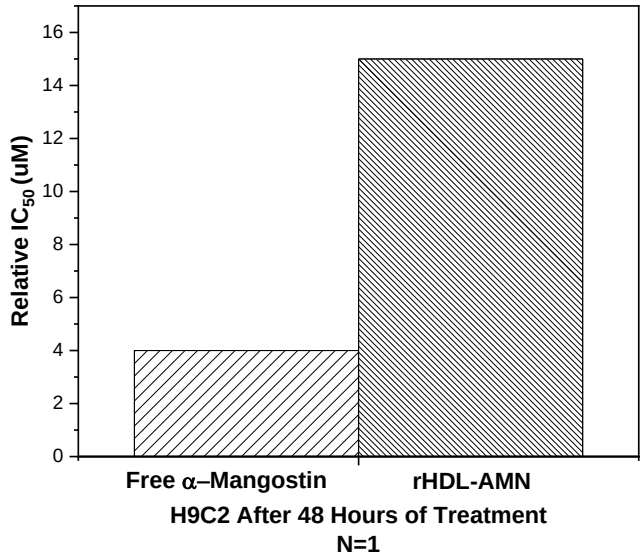

Figure 47. *H9C2 IC_{50} values after 48 hours.*

The LDL-A7 was used as a negative control for the SR-B1 expression and had the lowest relative expression of the SR-B1. The relative IC50 is shown below in Figure 49. The IC_{50} values are listed in Table 13. Finally, the empty rHDL did not induce any toxicity.

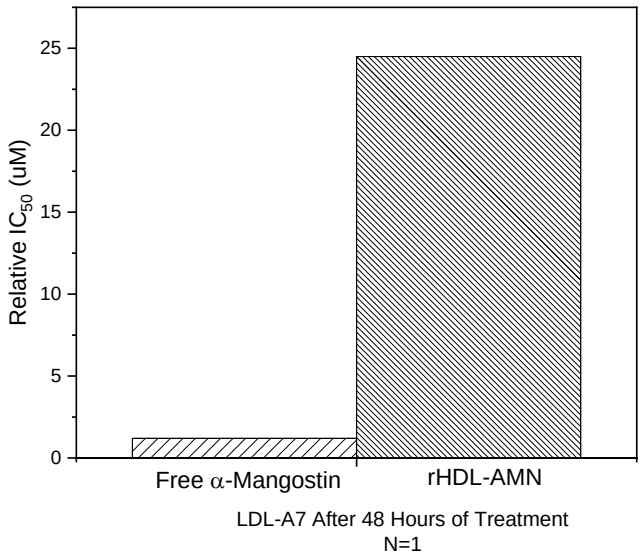

Figure 48. *LDL-A7 IC_{50} values after 48 hours.*

Table 13. *Summarized IC50 values for H9C2 and LDL-A7.*

Cytotoxicity 48 Hours		
N=1	H9C2	LDL-A7
α-Mangostin	**4.01**	**1.2**
rHDL-AMN	**15.1**	**24.5**

3.2.5. Effects of Serum Starvation

Because α-Mangostin is a CDK4 inhibitor and serum starvation induces cellular arrest, a separate cytotoxicity assay was conducted to determine if there was a synergistic effect enhancing the cytotoxicity of α-Mangostin. PZ-HPV cells were plated and incubated with different serum concentrations and α-Mangostin treatments. Figure 49 depicts the results of serum and the IC_{50} of the cells.

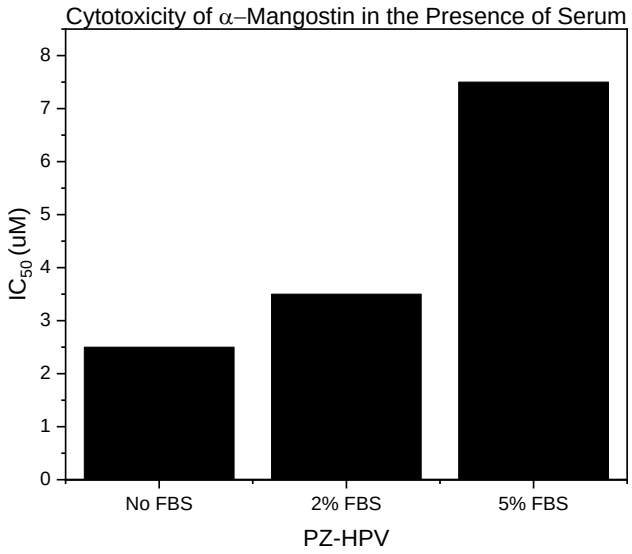

Figure 49. *PZ-HPV IC_{50} free after α-Mangostin in different serum concentrations concentrations.*

3.2.6. Summary of Specific Aim 2

In summary, this aim assessed some of the biological effects the rHDL-AMN nanoparticles possessed against the 2D cell models. First, the relative SR-B1 expression of the cell lines was determined using the JESS western blot system. Next, cytotoxicity assays were conducted using the DU145, PZ-HPV, LDL-A7, and H9C2 cells. Finally, the potential effects of the presence of serum were conducted.

Chapter 4

Discussion

The current gold-standard treatment for prostate cancer (PCa) is androgen deprivation therapy (ADT) which eventually induces the malignant castration-resistant variants (Higano, 2003). Unfortunately, treatments against CrPCa are limited to androgen deprivation therapies and harsh chemotherapies for patients who are often elderly. Therefore, is a need for new strategies that can target pathways outside of the AR and induce tumor regression.

Despite its promising therapeutic effects against various diseases, including Alzheimer's, autoimmune disorders, and cancers, the implementation of α-Mangostin as treatment remains limited (Gutierrez-Orozco et al., 2013; Wang et al., 2012; Zhou et al., 2020). The hydrophobicity of α-Mangostin may play a part in its severely low ability to absorb and transport throughout the body adequately. High oral dosages show low bioavailability and accumulation in the liver and the small intestine (Li et al., 2011; Ramaiya et al., 2012). Getting sufficient drug concentrations to the sites of tumors would be highly inefficient as large dosages would need to be administered daily without guaranteeing that the α-Mangostin would penetrate the tumor microenvironment and reach the tumor. Attempts to enhance its bioavailability have shown limited success. Pairing α-Mangostin with vegetable oil in capsules has shown enhancement in absorption. However, there is a continued accumulation of the α-Mangostin in specific organs (Zhao et al., 2016). Furthermore, α-Mangostin is still subjected to the effects of the first pass, which could further dilute its potency. In addition, a recent study modifying the structure of α-Mangostin failed to enhance the solubility of α-Mangostin. The derivatives produced had decreased cytotoxicity compared to the parent α-

Mangostin drug despite higher binding affinity to their target cholinesterase enzyme (Khaw et al., 2020).

Nevertheless, the selective anti-cancer effects of α-Mangostin could have great potential as a treatment or addition to combinatorial therapies. A targeted drug delivery system could diversify the route of administration for α-Mangostin and allow for efficient targeting of CrPCa tumors. Several different types of nanoparticles ranging from metal and protein-based, have been used to encapsulate α-Mangostin (Wathoni et al., 2020). However, many nanoparticles lack biocompatibility and targeting systems limiting their employment against tumors (Iannitti et al., 2010; Karlsson et al., 2009; Wilhelm et al., 2016). On the other hand, the reconstituted High-Density Lipoprotein (rHDL) drug delivery system possesses both a targeting feature and biocompatibility (Lacko et al., 2015). The rHDL is a nanoparticle that mimics the intrinsic HDL found in the body. It is non-immunostimulatory and processed similarly to natural HDL (Mooberry et al., 2016).

Most importantly, the rHDL retains its ability to bind to the SR-B1, allowing it to deliver its contents into the target cell. Therefore, the rHDL can take advantage of the overexpression of the SR-B1, making them the preferential targets for delivering α-Mangostin (Gordon et al., 2019; Traughber et al., 2020). In this study, the rHDL drug delivery platform was utilized to determine if α-Mangostin can be encapsulated to form rHDL-AMN nanoparticles while retaining the cytotoxic effects of α-Mangostin against PCa cells.

Despite the discovery of α-Mangostin dating back well over 150 years, there has yet to be any published data on the fluorescent characteristics of the α-Mangostin (Schmid, 1855). Nevertheless, the fluorescence properties could be used to characterize the rHDL-AMN particles further. The xanthone backbone of α-Mangostin is similar to the 9H-xanthene structure present in highly

fluorescent dyes such as fluorescein (Figure 28) (Katori et al., 2015). Beginning with the excitation spectra ranges from 300nm to 405nm. This spectrum sits in an unfavorable region; many biological compounds, such as amino acid residues like Tyrosine, which are excited at 280nm, are close to this range. For example, ApoA1found on the rHDL has tyrosine residues; therefore, there could be interference when using specific wavelengths close to the maxima of 320 nm (Didonato et al., 2014). For this reason, 375nm was chosen for many studies as it will give enough signal for the emission spectra and far enough to not produce too much interference from the other components found in the rHDL shell.

The emission spectra stretched from 450nm to about 700nm. Interestingly the emission spectrum was far from the excitation spectrum, creating a considerable distance between maxima and producing an enormous Stoke's Shift in DMSO. A large Stoke's Shift reduces spectral overlap and interference from the excitation spectra (Gao et al., 2017). In addition, the emission spectra sit within the green region of the visible spectra; therefore, this could be used for further studies such as imaging or FRET systems. Next, the anisotropy for the free α-Mangostin served as a baseline to be compared with the rHDL-AMN particles. Its anisotropy of 0.05 is extremely low, suggesting a high degree of uninhibited free rotation for the drug in DMSO. Differences in the anisotropy values depend on the fluorophore's environment, such as through aggregation and binding (Thompson, 2009). Similarly, the environment affects the fluorescence lifetime (FLT); changes in the FLT suggest aggregation, FRET, or binding. In DMSO, the free α-Mangostin had an FLT of 1.56ns (Berezin & Achilefu, 2010).

The physical characteristics reported by the DLS measurements suggest that a stable and homogenous formulation of the rHDL-AMN was produced using this current protocol. The polydispersity index (PDI) the was below the FDA-recommended PDI of 0.2. However, PDI

values below 0.3 have been considered acceptable for lipid-based nanoparticles (Xu et al., 2022). The rHDL-AMN and empty rHDL produced have a relatively high degree of homogeneity for the particles. The PDI is an excellent metric to determine sample quality as aberrant values for the PDI suggest instability or possible degradation of the particles. In addition, the TEM images have shown that the particles appear relatively homogenous for the empty particles; however, the highly concentrated rHDL-AMN particles are difficult to make out fully.

Next, the zeta potential (ZP) was within a stable range of values. For lipid-based particles, a ZP with an absolute value of 30 mV is recommended; however, a range between 20-40mV is typically reported (Samimi et al., 2019). A higher ZP suggests a lower aggregation tendency between particles due to a strong repulsive force. Conversely, a ZP close to zero could suggest that particles are undergoing degradation. Additionally, the value for the ZP is negatively charged. It has been reported that a strongly negative charge for lipid-based nanoparticles may encourage filtration by the kidneys (Samimi et al., 2019). However, because the rHDL contains the ApoA1, the rHDL should remain excluded from expulsion by the urinary system.

The particle diameter is an important metric to determine the relative particle size. The reports by the DLS system give both a number and intensity distribution. According to Malvern, the company that produced this DLS system, the intensity distribution should be the reported diameter. However, the DLSS reports the hydrodynamic diameter of the particles and not necessarily the actual diameter, illustrated in Figure 51. The intensity distribution is highly dependent on the characteristics of the particles. Aggregating particles will cause the skewing of the intensity distribution to larger values, thus giving diameter estimates not representative of the particles. For example, a study utilizing non-aggregating silicon particles and heavily aggregating iron nanoparticles reported intense skewing depending on the particles' surface characteristics. The

silicon particles had a Z-average reflective of their diameter measured from transmission electron

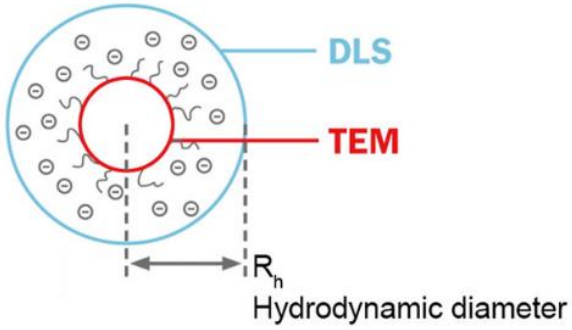

Figure 51. *Differences in the reported diameter between DLS and TEM imaging (Paluga, 2022).*

microscope (TEM) images. For the iron nanoparticles, their diameter, according to the TEM, was

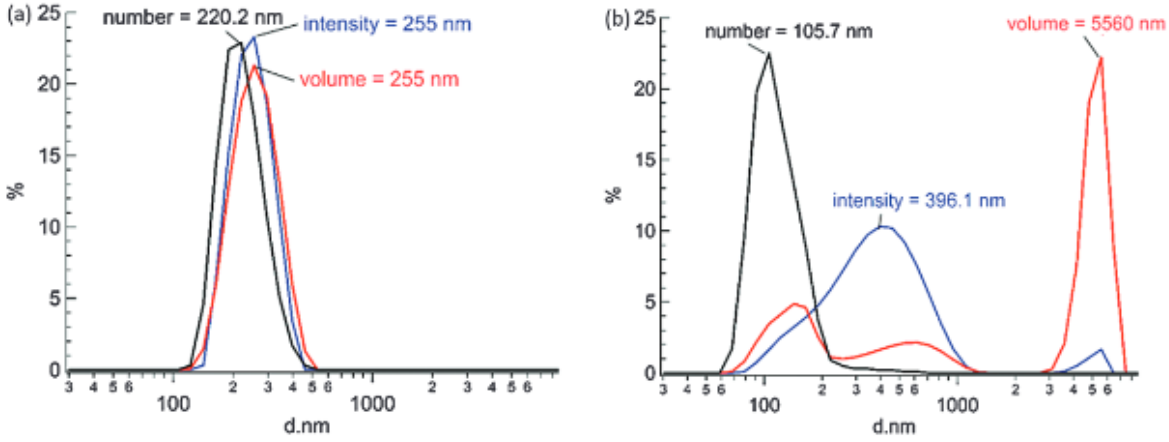

Figure 52. *The Tendency for aggregation causes the reported diameter to be inconsistent between distributions (Left) Low aggregating Silicon Nanoparticles (Right) High aggregating iron nanoparticles (Yeap et al., 2018).*

about 30nm. However, the DLSS reported a Z-average of over 300nm. In addition, the TEM images showed immense aggregates that could be misinterpreted as a single particle to the DLS (Yeap et al., 2018).

The intensity distribution reported was larger than what was expected for normal HDL. Rather than sizes under 60nm, the diameters were reported between 70nm to 120nm. The size by intensity for the empty and rHDL-AMN was larger than what was observed under the TEM. Instead, the number distribution was more reflective of the image particles. The reported ZP for the samples

suggests a high repulsion between particles, reducing the tendency for aggregation. On the other hand, the samples could be too concentrated, causing either the ZP or the diameter measurements to be reported larger than they are. Some optimization is still required to determine the effects of concentration on these characteristics. Ideally, all the distributions should line up. However, it has been shown that the tendency for aggregation can cause significant differences in the reported values from the DLS, as shown in Figure 52 (Yeap et al., 2018). The tendency for aggregation may skew data towards the larger values and show deviance between the different distributions.

While the rHDL-AMN are within the HDL range according to the number distribution and TEM images, it has yet to be determined what effects rHDL diameter has on the uptake of the rHDL. There may be benefits to producing larger or smaller particles that have yet to be observed, such as greater penetration or drug-carrying capacity. Reports of diameters between 30nm and 60nm appear optimal for endocytic uptake; however, this could potentially be more flexible with the rHDL due to the receptor-mediated transfer of the contents (Hoshyar et al., 2016). Further studies will be needed to determine if diameter corresponds with different biological effects.

Finally, the stability of the rHDL-AMN was showed that after 43 days, the particles retained their stability while stored under four degrees Celsius. Without filtering, the PDI values for rHDL-AMN did elevate, possibly due to aggregation and setline; however, they were still under 0.3. Filtering may have removed large aggregates, restoring the PDI values to what they were on Day 0. However, filtering was observed to reduce the concentration of α-Mangostin; therefore, if kept in solution for extended periods, filtering and remeasuring the drug concentration is recommended. It is still to be determined what the shelf life of the particle is after more extended periods.

Additionally, the rHDL-AMN would be lyophilized for extended periods and stored in colder environments. It has yet to be explored how storage under these conditions would affect the

particle. Finally, the behavior of the particles in serum and at body temperature will need to be determined in the future. Premature release of the drug due to instability could occur at higher temperatures; however, based on the cytotoxicity data, the particles appear to remain stable and not release the entirety of the cargo into the media after 48 hours.

The absorbance and fluorescence characterization of the free α-Mangostin was crucial for determining the encapsulation of α-Mangostin. Initial analysis of the PD-10 gravity column elutions revealed the pattern that a majority of the α-Mangostin appeared in the same fraction associated with the rHDL. Free α-Mangostin would immediately aggregate together and become immobilized within the PD-10 column; therefore, it would not appear in eluted fractions. If there is micellar entrapment of the α-Mangostin, then it would be expected that a more considerable variance in molecular weight and α-Mangostin would appear in the various fractions. The empty and rHDL-AMN particles had identical elution patterns; however, the characteristic excitation spectra of α-Mangostin were present with the rHDL-AMN. Together this suggests an association between the rHDL particles and the α-Mangostin

This current formulation and protocol's overall encapsulation efficiency is around 40%. However, further optimization and alterations to the chosen components of the rHDL are expected to reduce the amount of drug lost during the purification process. Dialysis and the PD-10 column should remove/reduce unbound drug and unincorporated micelles from the samples. Therefore, different ratios of lipids to ApoA1 and types of lipids could better accommodate the encapsulation process of the α-Mangostin; however, these will need to be determined in later studies. Ultimately, this encapsulation efficiency was enough to carry out the cytotoxicity portion of the study.

The Drug loading study used double the initial concentrations of the α-Mangostin to determine the maximum packing with this protocol. The PD-10 column helped process the samples and remove

unbound drugs faster than dialysis; however, this process produced less homogenous particles with an average PDI of 0.25 for rHDL-AMN using the standard formulation with an initial drug concentration of 0.5 mg/ml. The 1.0 mg/ml formulation produced a PDI above the recommended 0.3. Therefore, it was considered outside of the desired homogeneity. However, if dialysis was used instead, this could produce a more favorable PDI. Unexpectedly, the 1.0 mg/ml had a significantly smaller diameter than the 0.5 mg/ml formulation based on the number distribution according to the DLS. The particles were reported smaller than those produced by the 0.5mg/ml and empty formulations. It is possible that less aggregation and tighter packing of the α-Mangostin or minor particles. Information from the TEM could aid in determining the proper size of the particles. However, these particles were not imaged. Interestingly despite only changing the drug concentration, there was a similar encapsulation efficiency between those formulations. The higher drug concentrations could enhance some interactions between the rHDL components and the α-Mangostin, possibly causing more drug packing.

The steady-state anisotropy of the α-Mangostin associated with the rHDL was significantly higher than for the free drug. This change indicates inhibition of rotation, possibly caused by aggregation within the core of the rHDL. However, there is a lack of visible aggregation, and the unbound drug would be removed during dialysis and the PD-10 column. Therefore, it is most likely that the drug has entered the core of the rHDL, causing restriction in its movement. Disrupting the particles with DMSO caused the anisotropy to return to similar values to the free drug. The non-polar environment would encourage the release of the α-Mangostin as the particle possibly inverts to reduce the contact the phospholipids have with the DMSO.

Values for the FLT show a similarly drastic change between the free α-Mangostin and rHDL-AMN. The FLT decreased by more than half inside the particles while using DMSO resuspension

restored the FLT to a similar value to the free drug. Restoration of the FLT indicates a change in the drug's environment, possibly due to the packing of the drug causing homo-FRET or binding to a component of the rHDL. It may be possible to employ time-resolved anisotropy techniques to determine if homo-FRET is causing the decrease in the FLT (Teijeiro-Gonzalez et al., 2021). If Homo-FRET is observed, this can further suggest that tight packing of the α-Mangostin is occurring within the core of the rHDL (Bader et al., 2009). However, time-resolved anisotropy is often relegated to protein-based fluorophores. The anisotropy and FLT changes indicate that α-Mangostin is encapsulated within the rHDL.

The rHDL-AMN particles produced from this formulation are stable and relatively homogenous. In addition, the changes in the fluorescence properties and the appearance of the identical excitation spectra support that the α-Mangostin is within the rHDL. However, further optimization for the particles will need to be conducted in the future to reduce drug loss. The phenomena related to the reduction in the FLT may have some relationship with the difference in the drug packing. While not shown, it was observed that the emission of the 1.0 mg/ml formulation produced a lower intensity when compared to the 0.5 mg/ml sample. The FLT for the 1.0 mg/ml could shed additional light on the possibility of homo-FRET inducing these changes in the fluorescent properties.

The cytotoxic effects of the rHDL-AMN are retained as they continue to reduce the cell viability to the PCa and high expressors of the SR-B1. Cytotoxicity assays show that the rHDL-AMN behaved differently from the free drug. Under 24-hour incubation, the rHDL-AMN had virtually no effect on the DU145 cancer cell line. However, after 48 hours, there was a drastic decrease in the reported IC_{50}. This response was delayed when compared to the free drug. Where after 24 hours, extensive apoptosis was observed. Interestingly, the free drug values differed compared to

the IC_{50} reported by Johnson et al. The IC_{50} for the DU145 was 22 uM, while these experiments reported it closer to 3uM (Johnson et al., 2012). The number of cell passages could cause this stark contrast; however, the conditions of the cytotoxicity assay could have had a synergistic effect as the cells were under serum starvation for 48 hours. Serum starvation has been observed to reduce the expression of CDK4/6; therefore, introducing an inhibitor like α-Mangostin may induce enhanced apoptosis (Shin et al., 2008).

The PZ-HPV was chosen as a model to represent a low expression of SR-B1. It was expected that the rHDL would protect PZ-HPV from α-Mangostin if toxicity is observed. Previous studies using PZ-HPV have shown that the rHDL confers protection by restricting access to the drug payload such as valrubicin due to its low expression of the SR-B1 (Lacko et al., 2012). However, both the rHDL-AMN and the free α-Mangostin caused significant apoptosis. It has been reported that α-Mangostin is tolerable to normal cells, as seen in the paper by Johnson et al. In that experiment, the normal cell line was represented by HPreC, a primary human prostate epithelial cell line. No IC_{50} values were reported for HPreC; however, their experiment showed tolerance. However, PZ-HPV is an immortalized cell line; therefore, it may have been inappropriate to utilize this cell line. The PZ-HPV may already have some cell-cycle dysregulation that may enhance the susceptibility to the apoptotic effects of α-Mangostin. Furthermore, the cancer-specific cancer effects were first observed in primary monocytes rather than in an immortalized cell line (K. Matsumoto et al., 2003). Finally, these cells were under serum-starved conditions like the DU145 cells. Adding 5% of serum during treatments of the free drug on PZ-HPV more than tripled the IC_{50} values. Either the α-Mangostin was binding to the serum's components, or the serum's presence allowed enough CDK4 to maintain cellular division (Shin et al., 2008).

The cytotoxicity of rHDL-AMN against low SR-B1 expressing cells did reveal some protection. The H9C2 and the LDL-A7 appeared to have resisted high dosages of the rHDL-AMN due to less SR-B1 on their surfaces. The LDL-A7 had a staggering resistance to the rHDL-AMN compared to the free α-Mangostin. These experiments show a relationship between the SR-B1 expression and the degree of cytotoxicity caused by the rHDL-AMN. Further repeats of these experiments will be conducted. Furthermore, the blocking of the SR-B1 may show protective effects against the high expressors of the SR-B1-like cancer cells. If a chemical or anti-body blocking agent is used, then the abrogation of the effects of the rHDL on the high expressors may be observed.

The effects of the rHDL-AMN fell below expectations, as it appeared not to enhance the cytotoxic effects against the DU145 nor confer protection against the PZ-HPV. Based on the literature, it was expected that the DU145 was to overexpress the SR-B1. However, JESS analysis showed a relatively low expression while the PZ-HPV expressed higher SR-B1 than the DU145. The expression profiles may have altered due to the age and passage number of the cells. This change explains the muted effects against the DU145 and the toxicity of the PZ-HPV. Nevertheless, the protective effects found on the low expressors suggest that the SR-B1 is key to toxicity caused by the rHDL-AMN.

The variance in the IC_{50} values led to a significant standard deviation for both the PZ-HPV and DU145 trials. Trials using different rHDL-AMN preparations produced different IC_{50} values. However, repeated trials using the same batch produced the same results. This inter-batch variation could be due to several different reasons. The concentration of the α-Mangostin in the rHDL-AMN was most likely imprecisely measured. Obtaining the concentration requires the removal of the scattering profile. Removal of this portion of the spectra needs to be more precise, or a different

wavelength should be chosen separately from the baseline. In addition, improper concentrations between samples could cause this variation.

Additionally, the total number of particles could differ between samples. Despite equimolar concentrations, the exact density of the particles could differ between samples causing different amounts of binding. This variable is a complex parameter to control as particle concentrations are often estimated to large magnitudes, such as the power of 14. Future experiments should determine the reliability of the concentration measurements produced by the DLS. Furthermore, these treatments could saturate the amount of expressed SR-B1, thus blunting the observed cytotoxicity as there is a bottleneck in the delivery of the drug.

It is assumed that the drug is evenly distributed between particles. Therefore, empty rHDL particles may remain within the rHDL-AMN solution and compete with the loaded particles. While the significance of these factors is unknown or, in this circumstance, trivial, future experiments may further elucidate if there is a relationship. Additionally, the saturation of the SR-B1 and competition between particles could pose another issue. The empty rHDL and rHDL-AMN carrying low and high concentrations of α-Mangostin could be competing for the limited amounts of receptor access. Then factoring in the turn-over rate for the SR-B1, these make direct comparisons between the free drug and the rHDL difficult.

Finally, using cell viability to measure the cytotoxicity of treatment poses limitations. Firstly, the IC50 reports the relative dosages to incur a 50% of inhibition. These values may be inconsistent depending on the cellular conditions, cell state, cell density, and cellular characteristics (He et al., 2016). Experiments using the free drug alone failed to reproduce the results from Johnson et al. as the α-Mangostin appeared more toxic than reported. However, a possibility is that serum starvation contributed to the enhanced cytotoxicity. It was apparent that the serum affected the IC_{50} values,

as shown in the experiment using varying FBS concentrations with the PZ-HPV cells. However, it is unclear if this had to do with CDK4 expression or if some serum component trapped the α-Mangostin. A more robust study could employ Propidium Iodide and Annexin V staining to show the degree of cells undergoing specifically apoptosis (Rieger et al., 2011). Therefore, more subtle effects of the delivery of the α-Mangostin can be recorded. In addition to staining, measuring the expression of activated CDK4 would give specific information on the physical state of the cells. Furthermore, α-Mangostin is not as potent as many other chemotherapeutic drugs; therefore, time may play a significant factor, especially in cells that do not rapidly divide; this may be why it is reported to be relatively non-toxic to primary cell lines.

Finally, the 2D model lacks the complex organization of different cells found in the body. Each cell theoretically has similar surface access to the treatment; therefore, even the free α-Mangostin may act as a potent inhibitor of cellular growth. More complex models, such as the implementation of 3D spheroids, can add more complex layers by reducing access to the treatment. Other models could include bioreactors that mimic how nutrients flow in the body, or co-cultures of high and low expressing SR-B1 cells could better distinguish the differences between the rHDL-AMN and the free drug. Restricting treatment access and the rHDL-AMN selectivity to high SR-B1 expressing cells cannot be demonstrated using these 2D cell cultures. Using animal models may provide the best results and highlight the qualities of the rHDL far better. Oral or systemic injections of the free α-Mangostin should show its limited distribution. Equimolar treatments using the rHDL-AMN and the free drug should better demonstrate the qualities of the rHDL.

This study ultimately established a protocol for encapsulating α-Mangostin and showed that the rHDL-AMN retained the cytotoxic effects of α-Mangostin. The particles produced show favorable physical characteristics such as small size, homogeneity, and stability. However, there is room for

more optimization to enhance the drug loading capability of the particles through changes in molar concentrations or types of lipids used in the formulation. Further studies will need to be conducted utilizing more complex models. 2D models can tell a limited amount of information about the behavior of a nanoparticle. Many of the benefits of the nanoparticle cannot be observed unless used in an in-vivo setting. The body is a complex system where cells have different access to treatments. 2D cultures typically have monolayers with equal access to treatment. Employment of a 3D model could describe the degree of tumor penetration the rHDL-AMN may have. With further studies, the rHDL-AMN may one day become a potent therapy for treating prostate cancer and any high SR-B1 expressing cancer. The cancer-selective α-Mangostin and the rHDL provide a unique combination with a dual targeting system. The rHDL allows the α-Mangostin to be delivered systemically and targets the high SR-B1 expressing cancer cells while protecting normal cells. The α-Mangostin induces apoptosis primarily in cancer cells; therefore, if there is off-target binding, it may not be potent enough to induce apoptosis. Eventually, this therapy may induce tumor regression without the expense of the patient's quality of life.

Bibliography

Aaron, L., Franco, O. E., & Hayward, S. W. (2016). Review of Prostate Anatomy and Embryology and the Etiology of Benign Prostatic Hyperplasia. *Urologic Clinics of North America*, *43*(3), 279-288. https://doi.org/10.1016/j.ucl.2016.04.012

ACS. (2022a). *American Cancer Society Recommendations for Prostate Cancer Early Detection*. https://www.cancer.org/cancer/prostate-cancer/detection-diagnosis-staging/acs-recommendations.html

ACS. (2022b). *Survival Rates for Prostate Cancer*. American Cancer Society https://cancerstatisticscenter.cancer.org/#!/cancer-site/Prostate

Adamczyk, P., Wolski, Z., Butkiewicz, R., Nussbeutel, J., & Drewa, T. (2014). Significance of atypical small acinar proliferation and extensive high-grade prostatic interaepithelial neoplasm in clinical practice. *Central European Journal of Urology*, *67*(2). https://doi.org/10.5173/ceju.2014.02.art4

Adhyam, M., & Gupta, A. K. (2012). A Review on the Clinical Utility of PSA in Cancer Prostate. *Indian Journal of Surgical Oncology*, *3*(2), 120-129. https://doi.org/10.1007/s13193-012-0142-6

Aizat, W. M., Ahmad-Hashim, F. H., & Syed Jaafar, S. N. (2019). Valorization of mangosteen, "The Queen of Fruits," and new advances in postharvest and in food and engineering applications: A review. *Journal of Advanced Research*, *20*, 61-70. https://doi.org/10.1016/j.jare.2019.05.005

Attarilar, S., Yang, J., Ebrahimi, M., Wang, Q., Liu, J., Tang, Y., & Yang, J. (2020). The Toxicity Phenomenon and the Related Occurrence in Metal and Metal Oxide Nanoparticles: A Brief Review From the Biomedical Perspective [Review]. *Frontiers in Bioengineering and Biotechnology*, *8*. https://doi.org/10.3389/fbioe.2020.00822

Aurilio, G., Cimadamore, A., Mazzucchelli, R., Lopez-Beltran, A., Verri, E., Scarpelli, M., Massari, F., Cheng, L., Santoni, M., & Montironi, R. (2020). Androgen Receptor Signaling Pathway in Prostate Cancer: From Genetics to Clinical Applications. *Cells*, *9*(12), 2653. https://doi.org/10.3390/cells9122653

Bader, A. N., Hofman, E. G., Voortman, J., Van Bergen En Henegouwen, P. M. P., & Gerritsen, H. C. (2009). Homo-FRET Imaging Enables Quantification of Protein Cluster Sizes with Subcellular Resolution. *Biophysical Journal*, *97*(9), 2613-2622. https://doi.org/10.1016/j.bpj.2009.07.059

Bengoechea-Alonso, M. T., & Ericsson, J. (2007). SREBP in signal transduction: cholesterol metabolism and beyond. *Current Opinion in Cell Biology*, *19*(2), 215-222. https://doi.org/https://doi.org/10.1016/j.ceb.2007.02.004

Berezin, M. Y., & Achilefu, S. (2010). Fluorescence Lifetime Measurements and Biological Imaging. *Chemical Reviews*, *110*(5), 2641-2684. https://doi.org/10.1021/cr900343z

Bolin, D. J., & Jonas, A. (1994). Binding of lecithin:cholesterol acyltransferase to reconstituted high density lipoproteins is affected by their lipid but not apolipoprotein composition. *Journal of Biological Chemistry*, *269*(10), 7429-7434. https://doi.org/10.1016/s0021-9258(17)37303-9

Brody, T. O. M. (1999). 6 - LIPIDS. In T. O. M. Brody (Ed.), *Nutritional Biochemistry (Second Edition)* (pp. 311-378). Academic Press. https://doi.org/https://doi.org/10.1016/B978-012134836-6/50009-3

Brooke, G. N., Parker, M. G., & Bevan, C. L. (2008). Mechanisms of androgen receptor activation in advanced prostate cancer: differential co-activator recruitment and gene expression. *Oncogene*, *27*(21), 2941-2950. https://doi.org/10.1038/sj.onc.1210955

Bumbaca, B., & Li, W. (2018). Taxane resistance in castration-resistant prostate cancer: mechanisms and therapeutic strategies. *Acta pharmaceutica Sinica. B*, *8*(4), 518-529. https://doi.org/10.1016/j.apsb.2018.04.007

Cai, C., Chen, S., Ng, P., Bubley, G. J., Nelson, P. S., Mostaghel, E. A., Marck, B., Matsumoto, A. M., Simon, N. I., Wang, H., Chen, S., & Balk, S. P. (2011). Intratumoral De Novo Steroid Synthesis Activates Androgen Receptor in Castration-Resistant Prostate Cancer and Is Upregulated by Treatment with CYP17A1 Inhibitors. *Cancer Research*, *71*(20), 6503-6513. https://doi.org/10.1158/0008-5472.can-11-0532

Cai, Q., Chen, Y., Zhang, D., Pan, J., Xie, Z., Xu, C., Li, S., Zhang, X., Gao, Y., Hou, J., Guo, X., Zhou, X., Zhang, B., Ma, F., Zhang, W., Lin, G., Xin, Z., Niu, Y., & Wang, Y. (2020). Estimates of over-time trends in incidence and mortality of prostate cancer from 1990 to 2030. *Translational Andrology and Urology*, *9*(2), 196-209. https://doi.org/10.21037/tau.2020.02.21

CDC. (2020). *Prostate Cancer Statistics*. Center for Disease Control and Prevention. https://www.cdc.gov/cancer/prostate/statistics/index.htm#:~:text=Aside%20from%20non%2Dmelanoma%20skin,races%20and%20Hispanic%20origin%20populations.

Chao, A. C., Hsu, Y.-L., Liu, C.-K., & Kuo, P.-L. (2011). α-Mangostin, a Dietary Xanthone, Induces Autophagic Cell Death by Activating the AMP-Activated Protein Kinase Pathway in Glioblastoma Cells. *Journal of Agricultural and Food Chemistry*, *59*(5), 2086-2096. https://doi.org/10.1021/jf1042757

Chen, J., Li, L., Yang, Z., Luo, J., Yeh, S., & Chang, C. (2017). Androgen-deprivation therapy with enzalutamide enhances prostate cancer metastasis via decreasing the EPHB6 suppressor expression. *Cancer Lett*, *408*, 155-163. https://doi.org/10.1016/j.canlet.2017.08.014

Chen, X., Mangala, L. S., Mooberry, L., Bayraktar, E., Dasari, S. K., Ma, S., Ivan, C., Court, K. A., Rodriguez-Aguayo, C., Bayraktar, R., Raut, S., Sabnis, N., Kong, X., Yang, X., Lopez-Berestein, G., Lacko, A. G., & Sood, A. K. (2019). Identifying and targeting angiogenesis-related microRNAs in ovarian cancer. *Oncogene*, *38*(33), 6095-6108. https://doi.org/10.1038/s41388-019-0862-y

Chiang, J. (2014). Liver Physiology: MetaboLism and Detoxification. In (pp. 1770-1782). https://doi.org/10.1016/B978-0-12-386456-7.04202-7

Choi, C. H. J., Zuckerman, J. E., Webster, P., & Davis, M. E. (2011). Targeting kidney mesangium by nanoparticles of defined size. *Proceedings of the National Academy of Sciences*, *108*(16), 6656-6661. https://doi.org/10.1073/pnas.1103573108

Choi, S. M., & Kam, S. C. (2015). Metabolic effects of androgen deprivation therapy. *Korean Journal of Urology*, *56*(1), 12. https://doi.org/10.4111/kju.2015.56.1.12

Chughtai, B., Forde, J. C., Thomas, D. D. M., Laor, L., Hossack, T., Woo, H. H., Te, A. E., & Kaplan, S. A. (2016). Benign prostatic hyperplasia. *Nature Reviews Disease Primers*, *2*(1), 16031. https://doi.org/10.1038/nrdp.2016.31

Cohen, R. J., Shannon, B. A., Phillips, M., Moorin, R. E., Wheeler, T. M., & Garrett, K. L. (2008). Central zone carcinoma of the prostate gland: a distinct tumor type with poor prognostic features. *J Urol*, *179*(5), 1762-1767; discussion 1767. https://doi.org/10.1016/j.juro.2008.01.017

Copland. (1853). A CASE OF SCIRRHUS. OF THE PROSTATE GLAND, WITH A CORRESPONDING AFFECTION OF THE LYMPHATIC GLANDS IN THE LUMBAR REGION AND IN THE PELVIS. . *The Lancet*, *61*, 393-394. https://doi.org/ 10.1016/S0140-6736(02)68759-8

Cumming, H., & Rücker, C. (2017). Octanol–Water Partition Coefficient Measurement by a Simple ¹H NMR Method. *ACS Omega*, *2*(9), 6244-6249. https://doi.org/10.1021/acsomega.7b01102

Danaei, M., Dehghankhold, M., Ataei, S., Hasanzadeh Davarani, F., Javanmard, R., Dokhani, A., Khorasani, S., & Mozafari, M. (2018). Impact of Particle Size and Polydispersity Index on the Clinical Applications of Lipidic Nanocarrier Systems. *Pharmaceutics*, *10*(2), 57. https://doi.org/10.3390/pharmaceutics10020057

de Boussac, H., Pommier, A. J., Dufour, J., Trousson, A., Caira, F., Volle, D. H., Baron, S., & Lobaccaro, J.-M. A. (2013). LXR, prostate cancer and cholesterol: the Good, the Bad and the Ugly. *American journal of cancer research*, *3*(1), 58-69. https://pubmed.ncbi.nlm.nih.gov/23359865

https://www.ncbi.nlm.nih.gov/pmc/articles/PMC3555197/

de Brot, S., & Mongan, N. P. (2018). The Cell Cycle and Androgen Signaling Interactions in Prostate Cancer. In B. D. Robinson, J. M. Mosquera, J. Y. Ro, & M. Divatia (Eds.), *Precision Molecular*

Pathology of Prostate Cancer (pp. 381-404). Springer International Publishing. https://doi.org/10.1007/978-3-319-64096-9_22

Deka, R., Courtney, P. T., Parsons, J. K., Nelson, T. J., Nalawade, V., Luterstein, E., Cherry, D. R., Simpson, D. R., Mundt, A. J., Murphy, J. D., D'Amico, A. V., Kane, C. J., Martinez, M. E., & Rose, B. S. (2020). Association Between African American Race and Clinical Outcomes in Men Treated for Low-Risk Prostate Cancer With Active Surveillance. *JAMA*, *324*(17), 1747. https://doi.org/10.1001/jama.2020.17020

Di Sebastiano, K., & Mourtzakis, M. (2014). The Role of Dietary Fat throughout the Prostate Cancer Trajectory. *Nutrients*, *6*(12), 6095-6109. https://doi.org/10.3390/nu6126095

Didonato, J. A., Aulak, K., Huang, Y., Wagner, M., Gerstenecker, G., Topbas, C., Gogonea, V., Didonato, A. J., Tang, W. H. W., Mehl, R. A., Fox, P. L., Plow, E. F., Smith, J. D., Fisher, E. A., & Hazen, S. L. (2014). Site-specific Nitration of Apolipoprotein A-I at Tyrosine 166 Is Both Abundant within Human Atherosclerotic Plaque and Dysfunctional. *Journal of Biological Chemistry*, *289*(15), 10276-10292. https://doi.org/10.1074/jbc.m114.556506

Duff, J., & McEwan, I. J. (2005). Mutation of Histidine 874 in the Androgen Receptor Ligand-Binding Domain Leads to Promiscuous Ligand Activation and Altered p160 Coactivator Interactions. *Molecular Endocrinology*, *19*(12), 2943-2954. https://doi.org/10.1210/me.2005-0231

Dutt, S. S., & Gao, A. C. (2009). Molecular mechanisms of castration-resistant prostate cancer progression. *Future Oncology*, *5*(9), 1403-1413. https://doi.org/10.2217/fon.09.117

Eggersmann, T. K., Degenhardt, T., Gluz, O., Wuerstlein, R., & Harbeck, N. (2019). CDK4/6 Inhibitors Expand the Therapeutic Options in Breast Cancer: Palbociclib, Ribociclib and Abemaciclib. *BioDrugs*, *33*(2), 125-135. https://doi.org/10.1007/s40259-019-00337-6

Eid, W., Dauner, K., Courtney, K. C., Gagnon, A., Parks, R. J., Sorisky, A., & Zha, X. (2017). mTORC1 activates SREBP-2 by suppressing cholesterol trafficking to lysosomes in mammalian cells. *Proceedings of the National Academy of Sciences*, *114*(30), 7999-8004. https://doi.org/10.1073/pnas.1705304114

EXF. (2022). *Mangosteen*. Exotic Fruit Market.

Feng, Q., & He, B. (2019). Androgen Receptor Signaling in the Development of Castration-Resistant Prostate Cancer [Review]. *Frontiers in Oncology*, *9*. https://doi.org/10.3389/fonc.2019.00858

Feng, Z., Lu, X., Gan, L., Zhang, Q., & Lin, L. (2020). Xanthones, A Promising Anti-Inflammatory Scaffold: Structure, Activity, and Drug Likeness Analysis. *Molecules*, *25*(3), 598. https://doi.org/10.3390/molecules25030598

Freedland, S. J., & Aronson, W. J. (2004). Examining the relationship between obesity and prostate cancer. *Reviews in urology*, *6*(2), 73-81. https://pubmed.ncbi.nlm.nih.gov/16985580

https://www.ncbi.nlm.nih.gov/pmc/articles/PMC1550782/

Gao, Z., Hao, Y., Zheng, M., & Chen, Y. (2017). A fluorescent dye with large Stokes shift and high stability: synthesis and application to live cell imaging. *RSC Advances*, *7*(13), 7604-7609. https://doi.org/10.1039/c6ra27547h

Geybels, M. S., Fang, M., Wright, J. L., Qu, X., Bibikova, M., Klotzle, B., Fan, J.-B., Feng, Z., Ostrander, E. A., Nelson, P. S., & Stanford, J. L. (2017). PTEN loss is associated with prostate cancer recurrence and alterations in tumor DNA methylation profiles. *Oncotarget*, *8*(48), 84338-84348. https://doi.org/10.18632/oncotarget.20940

Gordon, J. A., Midha, A., Szeitz, A., Ghaffari, M., Adomat, H. H., Guo, Y., Klassen, T. L., Guns, E. S., Wasan, K. M., & Cox, M. E. (2016). Oral simvastatin administration delays castration-resistant progression and reduces intratumoral steroidogenesis of LNCaP prostate cancer xenografts. *Prostate Cancer and Prostatic Diseases*, *19*(1), 21-27. https://doi.org/10.1038/pcan.2015.37

Gordon, J. A., Noble, J. W., Midha, A., Derakhshan, F., Wang, G., Adomat, H. H., Tomlinson Guns, E. S., Lin, Y.-Y., Ren, S., Collins, C. C., Nelson, P. S., Morrissey, C., Wasan, K. M., & Cox, M. E. (2019). Upregulation of Scavenger Receptor B1 Is Required for Steroidogenic and Nonsteroidogenic Cholesterol Metabolism in Prostate Cancer. *Cancer Research*, *79*(13), 3320-3331. https://doi.org/10.1158/0008-5472.CAN-18-2529

Gradinaru, C. C., Marushchak, D. O., Samim, M., & Krull, U. J. (2010). Fluorescence anisotropy: from single molecules to live cells. *The Analyst*, *135*(3), 452. https://doi.org/10.1039/b920242k

Gustavsen, G., Gullet, L., Cole, D., Lewine, N., & Bishoff, J. T. (2020). Economic burden of illness associated with localized prostate cancer in the United States. *Future Oncology*, *16*(1), 4265-4277. https://doi.org/10.2217/fon-2019-0639

Gutierrez-Orozco, F., Chitchumroonchokchai, C., Lesinski, G. B., Suksamrarn, S., & Failla, M. L. (2013). alpha-Mangostin: anti-inflammatory activity and metabolism by human cells. *J Agric Food Chem*, *61*(16), 3891-3900. https://doi.org/10.1021/jf4004434

Hara, T., Miyazaki, J.-i., Araki, H., Yamaoka, M., Kanzaki, N., Kusaka, M., & Miyamoto, M. (2003). Novel Mutations of Androgen Receptor. *Cancer Research*, *63*(1), 149. http://cancerres.aacrjournals.org/content/63/1/149.abstract

He, Y., Zhu, Q., Chen, M., Huang, Q., Wang, W., Li, Q., Huang, Y., & Di, W. (2016). The changing 50% inhibitory concentration (IC50) of cisplatin: a pilot study on the artifacts of the MTT assay and the precise measurement of density-dependent chemoresistance in ovarian cancer. *Oncotarget*, *7*(43), 70803-70821. https://doi.org/10.18632/oncotarget.12223

Higano, C. S. (2003). Side effects of androgen deprivation therapy: monitoring and minimizing toxicity. *Urology*, *61*(2), 32-38. https://doi.org/10.1016/s0090-4295(02)02397-x

Hirano, H., Ide, H., Lu, Y., Inoue, Y., Okada, H., & Horie, S. (2020). Impact of Pretreatment Total Cholesterol Level Is Associated With Metastasis of Prostate Cancer. *American Journal of Men's Health*, *14*(2), 155798832091878. https://doi.org/10.1177/1557988320918788

Hoshyar, N., Gray, S., Han, H., & Bao, G. (2016). The effect of nanoparticle size on in vivo pharmacokinetics and cellular interaction. *Nanomedicine (London, England)*, *11*(6), 673-692. https://doi.org/10.2217/nnm.16.5

Hung, S. H., Shen, K. H., Wu, C. H., Liu, C. L., & Shih, Y. W. (2009). Alpha-mangostin suppresses PC-3 human prostate carcinoma cell metastasis by inhibiting matrix metalloproteinase-2/9 and urokinase-plasminogen expression through the JNK signaling pathway. *J Agric Food Chem*, *57*(4), 1291-1298. https://doi.org/10.1021/jf8032683

Iannitti, Palmieri, B., Capone, Gatti, A., & Cetta, F. (2010). Intracellular heavy metal nanoparticle storage: progressive accumulation within lymph nodes with transformation from chronic inflammation to malignancy. *International Journal of Nanomedicine*, 955. https://doi.org/10.2147/ijn.s14363

Ibrahim, U. K., Kamarrudin, N., Suzihaque, M. U. H., & Abd Hashib, S. (2017). Local Fruit Wastes as a Potential Source of Natural Antioxidant: An Overview. IOP Conference Series: Materials Science and Engineering,

Imamura, Y., & Sadar, M. D. (2016). Androgen receptor targeted therapies in castration-resistant prostate cancer: Bench to clinic. *International Journal of Urology*, *23*(8), 654-665. https://doi.org/10.1111/iju.13137

Imiołek, M. (2015). *Studies of nonlinear absorption of eosins using two photon induced fluorescence*. https://doi.org/10.13140/RG.2.1.2907.8245

Jamaspishvili, T., Berman, D. M., Ross, A. E., Scher, H. I., De Marzo, A. M., Squire, J. A., & Lotan, T. L. (2018). Clinical implications of PTEN loss in prostate cancer. *Nature Reviews Urology*, *15*(4), 222-234. https://doi.org/10.1038/nrurol.2018.9

Jameson, E. T. a. D. M. (2005). *Fluorescence Lifetime*. https://iss.com/resources/research/technical_notes/K2CH_FLT.html

Jamnagerwalla, J., Howard, L. E., Allott, E. H., Vidal, A. C., Moreira, D. M., Castro-Santamaria, R., Andriole, G. L., Freeman, M. R., & Freedland, S. J. (2018). Serum cholesterol and risk of high-grade prostate cancer: results from the REDUCE study. *Prostate Cancer and Prostatic Diseases*, *21*(2), 252-259. https://doi.org/10.1038/s41391-017-0030-9

JASCO. (2022, January 21, 2022). *Fluorescence depolarization measurement of liposome*. https://www.jasco-global.com/solutions/fluorescence-depolarization-measurement-of-liposome/

Jeon, J. C., Park, J., Park, S., Moon, K. H., Cheon, S. H., & Park, S. (2016). Hypercholesterolemia Is Associated with a Shorter Time to Castration-Resistant Prostate Cancer in Patients Who Have Undergone Androgen Deprivation Therapy. *The World Journal of Men's Health*, *34*(1), 28. https://doi.org/10.5534/wjmh.2016.34.1.28

Johnson, J. J., Petiwala, S. M., Syed, D. N., Rasmussen, J. T., Adhami, V. M., Siddiqui, I. A., Kohl, A. M., & Mukhtar, H. (2012). -Mangostin, a xanthone from mangosteen fruit, promotes cell cycle arrest in prostate cancer and decreases xenograft tumor growth. *Carcinogenesis*, *33*(2), 413-419. https://doi.org/10.1093/carcin/bgr291

Jung, S.-H., Shin, S., Kim, M. S., Baek, I.-P., Lee, J. Y., Lee, S. H., Kim, T.-M., Lee, S. H., & Chung, Y.-J. (2016). Genetic Progression of High Grade Prostatic Intraepithelial Neoplasia to Prostate Cancer. *European urology*, *69*(5), 823-830. https://doi.org/https://doi.org/10.1016/j.eururo.2015.10.031

Kalepu, S., & Nekkanti, V. (2015). Insoluble drug delivery strategies: review of recent advances and business prospects. *Acta Pharmaceutica Sinica B*, *5*(5), 442-453. https://doi.org/https://doi.org/10.1016/j.apsb.2015.07.003

Karlsson, H. L., Gustafsson, J., Cronholm, P., & Möller, L. (2009). Size-dependent toxicity of metal oxide particles—A comparison between nano- and micrometer size. *Toxicology Letters*, *188*(2), 112-118. https://doi.org/https://doi.org/10.1016/j.toxlet.2009.03.014

Kato, M., Banuelos, C. A., Imamura, Y., Leung, J. K., Caley, D. P., Wang, J., Mawji, N. R., & Sadar, M. D. (2016). Cotargeting Androgen Receptor Splice Variants and mTOR Signaling Pathway for the Treatment of Castration-Resistant Prostate Cancer. *Clinical Cancer Research*, *22*(11), 2744-2754. https://doi.org/10.1158/1078-0432.ccr-15-2119

Katori, A., Azuma, E., Ishimura, H., Kuramochi, K., & Tsubaki, K. (2015). Fluorescent Dyes with Directly Connected Xanthone and Xanthene Units. *The Journal of Organic Chemistry*, *80*(9), 4603-4610. https://doi.org/10.1021/acs.joc.5b00479

Keating, G. M. (2015). Enzalutamide: a review of its use in chemotherapy-naïve metastatic castration-resistant prostate cancer. *Drugs Aging*, *32*(3), 243-249. https://doi.org/10.1007/s40266-015-0248-y

Khaw, K. Y., Kumar, P., Yusof, S. R., Ramanathan, S., & Murugaiyah, V. (2020). Probing simple structural modification of α-mangostin on its cholinesterase inhibition and cytotoxicity. *Archiv der Pharmazie*, *353*(11), 2000156. https://doi.org/10.1002/ardp.202000156

Krycer, J. R., & Brown, A. J. (2013). Does changing androgen receptor status during prostate cancer development impact upon cholesterol homeostasis? *PLoS ONE*, *8*(1), e54007. https://doi.org/10.1371/journal.pone.0054007

Kumar, A., & Dixit, C. K. (2017). 3 - Methods for characterization of nanoparticles. In S. Nimesh, R. Chandra, & N. Gupta (Eds.), *Advances in Nanomedicine for the Delivery of Therapeutic Nucleic Acids* (pp. 43-58). Woodhead Publishing. https://doi.org/https://doi.org/10.1016/B978-0-08-100557-6.00003-1

Kürle, S., Schulte, K. W., & Homey, B. (2009). [Accumulation of tattoo pigment in sentinel lymph nodes]. *Hautarzt*, *60*(10), 781-783. https://doi.org/10.1007/s00105-009-1843-9 (Akkumulation von Tatoo-Pigment im Sentinellymphknoten.)

Kurniawan, Y. S., Priyangga, K. T. A., Jumina, Pranowo, H. D., Sholikhah, E. N., Zulkarnain, A. K., Fatimi, H. A., & Julianus, J. (2021). An Update on the Anticancer Activity of Xanthone Derivatives: A Review. *Pharmaceuticals*, *14*(11), 1144. https://doi.org/10.3390/ph14111144

Kwiterovich, P. O., Jr. (1998). The antiatherogenic role of high-density lipoprotein cholesterol. *Am J Cardiol*, *82*(9a), 13q-21q. https://doi.org/10.1016/s0002-9149(98)00808-x

Lacko, A., Sabnis, Nair, Israel, & McConathy. (2012). Enhanced solubility and functionality of valrubicin (AD-32) against cancer cells upon encapsulation into biocompatible nanoparticles. *International Journal of Nanomedicine*, 975. https://doi.org/10.2147/ijn.s28029

Lacko, A. G., Nair, M., Paranjape, S., Johnso, S., & McConathy, W. J. (2002). High density lipoprotein complexes as delivery vehicles for anticancer drugs. *Anticancer Res*, *22*(4), 2045-2049.

Lacko, A. G., Sabnis, N. A., Nagarajan, B., & McConathy, W. J. (2015). HDL as a drug and nucleic acid delivery vehicle. *Frontiers in Pharmacology*, *6*. https://doi.org/10.3389/fphar.2015.00247

Lee, D. K., Park, J. H., Kim, J. H., Lee, S. J., Jo, M. K., Gil, M. C., Song, K. H., & Park, J. W. (2010). Progression of Prostate Cancer Despite an Extremely Low Serum Level of Prostate-Specific Antigen. *Korean Journal of Urology*, *51*(5), 358. https://doi.org/10.4111/kju.2010.51.5.358

Li, L., Brunner, I., Han, A.-R., Hamburger, M., Kinghorn, A. D., Frye, R., & Butterweck, V. (2011). Pharmacokinetics of α-mangostin in rats after intravenous and oral application. *Molecular Nutrition & Food Research*, *55*(S1), S67-S74. https://doi.org/10.1002/mnfr.201000511

Li, P., Tian, W., & Ma, X. (2014). Alpha-mangostin inhibits intracellular fatty acid synthase and induces apoptosis in breast cancer cells. *Molecular Cancer*, *13*(1), 138. https://doi.org/10.1186/1476-4598-13-138

Liao, Y., Liu, Y., Xia, X., Shao, Z., Huang, C., He, J., Jiang, L., Tang, D., Liu, J., & Huang, H. (2020). Targeting GRP78-dependent AR-V7 protein degradation overcomes castration-resistance in prostate cancer therapy. *Theranostics*, *10*(8), 3366-3381. https://doi.org/10.7150/thno.41849

Lim, C.-Y., Davis, O. B., Shin, H. R., Zhang, J., Berdan, C. A., Jiang, X., Counihan, J. L., Ory, D. S., Nomura, D. K., & Zoncu, R. (2019). ER–lysosome contacts enable cholesterol sensing by mTORC1 and drive aberrant growth signalling in Niemann–Pick type C. *Nature Cell Biology*, *21*(10), 1206-1218. https://doi.org/10.1038/s41556-019-0391-5

Liu, C., Lou, W., Zhu, Y., Nadiminty, N., Schwartz, C. T., Evans, C. P., & Gao, A. C. (2014). Niclosamide Inhibits Androgen Receptor Variants Expression and Overcomes Enzalutamide Resistance in Castration-Resistant Prostate Cancer. *Clinical Cancer Research*, *20*(12), 3198-3210. https://doi.org/10.1158/1078-0432.ccr-13-3296

Longo, J., Mullen, P. J., Yu, R., van Leeuwen, J. E., Masoomian, M., Woon, D. T. S., Wang, Y., Chen, E. X., Hamilton, R. J., Sweet, J. M., van der Kwast, T. H., Fleshner, N. E., & Penn, L. Z. (2019). An actionable sterol-regulated feedback loop modulates statin sensitivity in prostate cancer. *Molecular Metabolism*, *25*, 119-130. https://doi.org/https://doi.org/10.1016/j.molmet.2019.04.003

Malvern. (2014). Dynamic Light Scattering : An Introduction in 30 Minutes.

Mateo, J., Boysen, G., Barbieri, C. E., Bryant, H. E., Castro, E., Nelson, P. S., Olmos, D., Pritchard, C. C., Rubin, M. A., & De Bono, J. S. (2017). DNA Repair in Prostate Cancer: Biology and Clinical Implications. *European urology*, *71*(3), 417-425. https://doi.org/10.1016/j.eururo.2016.08.037

Matsumoto, K., Akao, Y., Kobayashi, E., Ohguchi, K., Ito, T., Tanaka, T., Iinuma, M., & Nozawa, Y. (2003). Induction of Apoptosis by Xanthones from Mangosteen in Human Leukemia Cell Lines. *Journal of Natural Products*, *66*(8), 1124-1127. https://doi.org/10.1021/np020546u

Matsumoto, K., Akao, Y., Kobayashi, E., Ohguchi, K., Ito, T., Tanaka, T., Iinuma, M., & Nozawa, Y. (2003). Induction of apoptosis by xanthones from mangosteen in human leukemia cell lines. *J Nat Prod*, *66*(8), 1124-1127. https://doi.org/10.1021/np020546u

Matsumoto, K., Akao, Y., Ohguchi, K., Ito, T., Tanaka, T., Iinuma, M., & Nozawa, Y. (2005). Xanthones induce cell-cycle arrest and apoptosis in human colon cancer DLD-1 cells. *Bioorganic & Medicinal Chemistry*, *13*(21), 6064-6069. https://doi.org/https://doi.org/10.1016/j.bmc.2005.06.065

Matsumoto, K., Akao, Y., Yi, H., Ohguchi, K., Ito, T., Tanaka, T., Kobayashi, E., Iinuma, M., & Nozawa, Y. (2004). Preferential target is mitochondria in alpha-mangostin-induced apoptosis in human leukemia HL60 cells. *Bioorg Med Chem*, *12*(22), 5799-5806. https://doi.org/10.1016/j.bmc.2004.08.034

Meijer, D., Van Moorselaar, R. J. A., Vis, A. N., & Bijnsdorp, I. V. (2019). Prostate Cancer Development Is Not Affected by Statin Use in Patients with Elevated PSA Levels. *Cancers*, *11*(7), 953. https://doi.org/10.3390/cancers11070953

Mitchell, M. J., Billingsley, M. M., Haley, R. M., Wechsler, M. E., Peppas, N. A., & Langer, R. (2021). Engineering precision nanoparticles for drug delivery. *Nature Reviews Drug Discovery*, *20*(2), 101-124. https://doi.org/10.1038/s41573-020-0090-8

Miyake, H., Matsushita, Y., Watanabe, H., Tamura, K., Motoyama, D., Ito, T., Sugiyama, T., & Otsuka, A. (2019). Prognostic Significance of Time to Castration Resistance in Patients With Metastatic Castration-sensitive Prostate Cancer. *Anticancer Research*, *39*(3), 1391-1396. https://doi.org/10.21873/anticanres.13253

Mooberry, L. K., Sabnis, N. A., Panchoo, M., Nagarajan, B., & Lacko, A. G. (2016). Targeting the SR-B1 Receptor as a Gateway for Cancer Therapy and Imaging [Review]. *Frontiers in Pharmacology*, *7*(466). https://doi.org/10.3389/fphar.2016.00466

Naji, L., Randhawa, H., Sohani, Z., Dennis, B., Lautenbach, D., Kavanagh, O., Bawor, M., Banfield, L., & Profetto, J. (2018). Digital Rectal Examination for Prostate Cancer Screening in Primary Care: A Systematic Review and Meta-Analysis. *The Annals of Family Medicine*, *16*(2), 149-154. https://doi.org/10.1370/afm.2205

Narasimhan, S., Maheshwaran, S., Abu-Yousef, I., Majdalawieh, A., Rethavathi, J., Das, P., & Poltronieri, P. (2017). Anti-Bacterial and Anti-Fungal Activity of Xanthones Obtained via Semi-Synthetic Modification of α-Mangostin from Garcinia mangostana. *Molecules*, *22*(2), 275. https://doi.org/10.3390/molecules22020275

NCBI, N. C. f. B. I. (2022a). *Alpha-Mangostin* https://pubchem.ncbi.nlm.nih.gov/compound/alpha-Mangostin

NCBI, N. C. f. B. I. (2022b). *Curcumin (Compound)* https://pubchem.ncbi.nlm.nih.gov/compound/969516#section=UNII

Neckers, D. C., & Valdes-Aguilera, O. M. (1993). Photochemistry of the Xanthene Dyes. In *Advances in Photochemistry* (pp. 315-394). https://doi.org/https://doi.org/10.1002/9780470133491.ch4

NIH. (2022). *Cholesteryl oleate*. NIH. https://pubchem.ncbi.nlm.nih.gov/compound/Cholesteryl-oleate

Nur Husna, S. M., Tan, H.-T. T., Mohamud, R., Dyhl-Polk, A., & Wong, K. K. (2018). Inhibitors targeting CDK4/6, PARP and PI3K in breast cancer: a review. *Therapeutic Advances in Medical Oncology*, *10*, 175883591880850. https://doi.org/10.1177/1758835918808509

Oda, M. N., Hargreaves, P. L., Beckstead, J. A., Redmond, K. A., Van Antwerpen, R., & Ryan, R. O. (2006). Reconstituted high density lipoprotein enriched with the polyene antibiotic amphotericin B. *Journal of Lipid Research*, *47*(2), 260-267. https://doi.org/10.1194/jlr.d500033-jlr200

Oh WK, H. M., D'Amico AV, et al. (2003). *Biology of Prostate Cancer*. BC Decker. https://www.ncbi.nlm.nih.gov/books/NBK13217/

Onrust, S. V., & Lamb, H. M. (1999). Valrubicin. *Drugs Aging*, *15*(1), 69-75; discussion 76. https://doi.org/10.2165/00002512-199915010-00006

Ostojic, S., Vlugt, T. J. H., & Nienhuis, B. (2007). Universal anisotropy in force networks under shear. *Physical Review E*, *75*(3), 030301. https://doi.org/10.1103/PhysRevE.75.030301

Oxford. Anisotropic. In.

Paluga, M. (2022). *HYDRODYNAMIC DIAMETER*. Fritsch. https://www.fritsch-international.com/particle-sizing/fritsch-knowledge/hydrodynamic-diameter/
Park, K. (2013). Facing the Truth about Nanotechnology in Drug Delivery. *ACS Nano*, *7*(9), 7442-7447. https://doi.org/10.1021/nn404501g
Pate, K., & Safier, P. (2016). 12 - Chemical metrology methods for CMP quality. In S. Babu (Ed.), *Advances in Chemical Mechanical Planarization (CMP)* (pp. 299-325). Woodhead Publishing. https://doi.org/https://doi.org/10.1016/B978-0-08-100165-3.00012-7
Pedraza-Chaverri, J., Cárdenas-Rodríguez, N., Orozco-Ibarra, M., & Pérez-Rojas, J. M. (2008). Medicinal properties of mangosteen (Garcinia mangostana). *Food Chem Toxicol*, *46*(10), 3227-3239. https://doi.org/10.1016/j.fct.2008.07.024
Pelser, C., Mondul, A. M., Hollenbeck, A. R., & Park, Y. (2013). Dietary Fat, Fatty Acids, and Risk of Prostate Cancer in the NIH-AARP Diet and Health Study. *Cancer Epidemiology Biomarkers & Prevention*, *22*(4), 697-707. https://doi.org/10.1158/1055-9965.epi-12-1196-t
Penning, T. M. (2014). Androgen biosynthesis in castration-resistant prostate cancer. *Endocrine-related cancer*, *21*(4), T67-T78. https://doi.org/10.1530/ERC-14-0109
Prasad, S., Tyagi, A. K., & Aggarwal, B. B. (2014). Recent developments in delivery, bioavailability, absorption and metabolism of curcumin: the golden pigment from golden spice. *Cancer research and treatment*, *46*(1), 2-18. https://doi.org/10.4143/crt.2014.46.1.2
Pu, L., Yu, H., Du, J., Zhang, Y., & Chen, S. (2020). Hydrotalcite–PLGA composite nanoparticles for loading and delivery of danshensu. *RSC Advances*, *10*(37), 22010-22018. https://doi.org/10.1039/d0ra01593h
Raghuraman, H., & Chattopadhyay, A. (2007). Orientation and Dynamics of Melittin in Membranes of Varying Composition Utilizing NBD Fluorescence. *Biophysical Journal*, *92*(4), 1271-1283. https://doi.org/10.1529/biophysj.106.088690
Ramaiya, A., Li, G., Petiwala, S. M., & Johnson, J. J. (2012). Single dose oral pharmacokinetic profile of α-mangostin in mice. *Curr Drug Targets*, *13*(14), 1698-1704. https://doi.org/10.2174/138945012804545524
Randolph, G. J., & Miller, N. E. (2014). Lymphatic transport of high-density lipoproteins and chylomicrons. *Journal of Clinical Investigation*, *124*(3), 929-935. https://doi.org/10.1172/jci71610
Rapiti, E., Fioretta, G., Schaffar, R., Neyroud-Caspar, I., Verkooijen, H. M., Schmidlin, F., Miralbell, R., Zanetti, R., & Bouchardy, C. (2009). Impact of socioeconomic status on prostate cancer diagnosis, treatment, and prognosis. *Cancer*, *115*(23), 5556-5565. https://doi.org/10.1002/cncr.24607
Raut, S., Garud, A., Nagarajan, B., Sabnis, N., Remaley, A., Fudala, R., Gryczynski, I., Gryczynski, Z., Dzyuba, S. V., Borejdo, J., & Lacko, A. (2020). Probing the Assembly of HDL Mimetic, Drug Carrying Nanoparticles Using Intrinsic Fluorescence. *Journal of Pharmacology and Experimental Therapeutics*, *373*(1), 113-121. https://doi.org/10.1124/jpet.119.262899
Raymond, S. C. C. (2013). Prostate. https://radiopaedia.org/articles/26055
Remali, J., Sahidin, I., & Aizat, W. M. (2022). Xanthone Biosynthetic Pathway in Plants: A Review [Review]. *Frontiers in Plant Science*, *13*. https://doi.org/10.3389/fpls.2022.809497
Rieger, A. M., Nelson, K. L., Konowalchuk, J. D., & Barreda, D. R. (2011). Modified annexin V/propidium iodide apoptosis assay for accurate assessment of cell death. *Journal of visualized experiments : JoVE*(50), 2597. https://doi.org/10.3791/2597
Ritter, M. C., & Scanus, A. M. (1977). Role of apolipoprotein A-I in the structure of human serum high density lipoproteins. Reconstitution studies. *J Biol Chem*, *252*(4), 1208-1216.
Roehrborn, C. G., & Black, L. K. (2011). The economic burden of prostate cancer. *BJU International*, *108*(6), 806-813. https://doi.org/10.1111/j.1464-410x.2011.10365.x

Rye, K.-A., Hime, N. J., & Barter, P. J. (1995). The Influence of Cholesteryl Ester Transfer Protein on the Composition, Size, and Structure of Spherical, Reconstituted High Density Lipoproteins. *Journal of Biological Chemistry*, *270*(1), 189-196. https://doi.org/10.1074/jbc.270.1.189

Rye, K. A., & Barter, P. J. (1994). The influence of apolipoproteins on the structure and function of spheroidal, reconstituted high density lipoproteins. *J Biol Chem*, *269*(14), 10298-10303.

Salvador, C., Planas, J., Agreda, F., Placer, J., Trilla, E., Lopez, M. A., & Morote, J. (2013). Analysis of the lipid profile and atherogenic risk during androgen deprivation therapy in prostate cancer patients. *Urol Int*, *90*(1), 41-44. https://doi.org/10.1159/000342814

Samimi, S., Maghsoudnia, N., Eftekhari, R. B., & Dorkoosh, F. (2019). Chapter 3 - Lipid-Based Nanoparticles for Drug Delivery Systems. In S. S. Mohapatra, S. Ranjan, N. Dasgupta, R. K. Mishra, & S. Thomas (Eds.), *Characterization and Biology of Nanomaterials for Drug Delivery* (pp. 47-76). Elsevier. https://doi.org/https://doi.org/10.1016/B978-0-12-814031-4.00003-9

Sandhu, G. S., & Andriole, G. L. (2012). Overdiagnosis of prostate cancer. *Journal of the National Cancer Institute. Monographs*, *2012*(45), 146-151. https://doi.org/10.1093/jncimonographs/lgs031

Saraswathy, S. U. P., Lalitha, L. C. P., Rahim, S., Gopinath, C., Haleema, S., SarojiniAmma, S., & Aboul-Enein, H. Y. (2022). A Review on Synthetic and Pharmacological Potential of Compounds Isolated from Garcinia mangostana Linn. *Phytomedicine Plus*, *2*(2), 100253. https://doi.org/https://doi.org/10.1016/j.phyplu.2022.100253

Schmid, W. (1855). Ueber das Mangostin. *Annalen der Chemie und Pharmacie*, *93*(1), 83-88. https://doi.org/10.1002/jlac.18550930105

Shah, S., Chib, R., Raut, S., Bermudez, J., Sabnis, N., Duggal, D., Kimball, J. D., Lacko, A. G., Gryczynski, Z., & Gryczynski, I. (2016). Photophysical characterization of anticancer drug valrubicin in rHDL nanoparticles and its use as an imaging agent. *Journal of Photochemistry and Photobiology B: Biology*, *155*, 60-65. https://doi.org/10.1016/j.jphotobiol.2015.12.007

Shahzad, M. M., Mangala, L. S., Han, H. D., Lu, C., Bottsford-Miller, J., Nishimura, M., Mora, E. M., Lee, J. W., Stone, R. L., Pecot, C. V., Thanapprapasr, D., Roh, J. W., Gaur, P., Nair, M. P., Park, Y. Y., Sabnis, N., Deavers, M. T., Lee, J. S., Ellis, L. M., Lopez-Berestein, G., McConathy, W. J., Prokai, L., Lacko, A. G., & Sood, A. K. (2011). Targeted delivery of small interfering RNA using reconstituted high-density lipoprotein nanoparticles. *Neoplasia*, *13*(4), 309-319. https://doi.org/10.1593/neo.101372

Sharifi, N. (2005). Androgen Deprivation Therapy for Prostate Cancer. *JAMA*, *294*(2), 238. https://doi.org/10.1001/jama.294.2.238

Shin, J.-S., Hong, S.-W., Lee, S.-L., Kim, T.-H., Park, I.-C., An, S.-K., Lee, W.-K., Lim, J.-S., Kim, K.-I., Yang, Y., Lee, S.-S., Jin, D.-H., & Lee, M.-S. (2008). Serum starvation induces G1 arrest through suppression of skp2-CDK2 and CDK4 in SK-OV-3 cells. *International Journal of Oncology*. https://doi.org/10.3892/ijo.32.2.435

Simonsen, J. B., & Kromann, E. B. (2021). Pitfalls and opportunities in quantitative fluorescence-based nanomedicine studies – A commentary. *Journal of Controlled Release*, *335*, 660-667. https://doi.org/https://doi.org/10.1016/j.jconrel.2021.05.041

Suhling, K., Hirvonen, L. M., Levitt, J. A., Chung, P.-H., Tregidgo, C., Le Marois, A., Rusakov, D. A., Zheng, K., Ameer-Beg, S., Poland, S., Coelho, S., Henderson, R., & Krstajic, N. (2015). Fluorescence lifetime imaging (FLIM): Basic concepts and some recent developments. *Medical Photonics*, *27*, 3-40. https://doi.org/https://doi.org/10.1016/j.medpho.2014.12.001

Sundaram, B. M., Gopalakrishnan, C., Subramanian, S., Shankaranarayanan, D., & Kameswaran, L. (1983). Antimicrobial Activities of Garcinia mangostana. *Planta Med*, *48*(05), 59-60.

Swyer, G. (1942). The cholesterol content of normal and enlarged prostates. *Cancer Res*, 1-4.

Taitt, H. E. (2018). Global Trends and Prostate Cancer: A Review of Incidence, Detection, and Mortality as Influenced by Race, Ethnicity, and Geographic Location. *American Journal of Men's Health*, *12*(6), 1807-1823. https://doi.org/10.1177/1557988318798279

Tamada, S., Iguchi, T., Kato, M., Asakawa, J., Kita, K., Yasuda, S., Yamasaki, T., Matsuoka, Y., Yamaguchi, K., Matsumura, K., Go, I., Ohmachi, T., & Nakatani, T. (2018). Time to progression to castration-resistant prostate cancer after commencing combined androgen blockade for advanced hormone-sensitive prostate cancer. *Oncotarget*, *9*(97), 36966-36974. https://doi.org/10.18632/oncotarget.26426

Tan, M. H. (1980). HDL-cholesterol: the negative risk factor for coronary heart disease. *Ann Acad Med Singap*, *9*(4), 491-495.

Taylor, L. G., Canfield, S. E., & Du, X. L. (2009). Review of major adverse effects of androgen-deprivation therapy in men with prostate cancer. *Cancer*, *115*(11), 2388-2399. https://doi.org/10.1002/cncr.24283

Teijeiro-Gonzalez, Y., Crnjar, A., Beavil, A. J., Beavil, R. L., Nedbal, J., Le Marois, A., Molteni, C., & Suhling, K. (2021). Time-Resolved Fluorescence Anisotropy and Molecular Dynamics Analysis of a Novel GFP Homo-FRET Dimer. *Biophysical Journal*, *120*(2), 254-269. https://doi.org/10.1016/j.bpj.2020.11.2275

Thienger, P., & Rubin, M. A. (2021). Prostate cancer hijacks the microenvironment. *Nature Cell Biology*, *23*(1), 3-5. https://doi.org/10.1038/s41556-020-00616-3

Thompson, D. (2007). Michael Faraday's recognition of ruby gold: the birth of modern nanotechnology. *Gold Bulletin*, *40*(4), 267-269. https://doi.org/10.1007/bf03215598

Thompson, M. (2009). Chapter 16 - Thermodynamic and Kinetic Analysis of Bromodomain–Histone Interactions. In *Methods in Enzymology* (Vol. 466, pp. 383-407). Academic Press. https://doi.org/https://doi.org/10.1016/S0076-6879(09)66016-X

Tran, V. A., Thi Vo, T.-T., Nguyen, M.-N. T., Duy Dat, N., Doan, V.-D., Nguyen, T.-Q., Vu, Q. H., Le, V. T., & Tong, T. D. (2021). Novel α-Mangostin Derivatives from Mangosteen (Garcinia mangostana L.) Peel Extract with Antioxidant and Anticancer Potential. *Journal of Chemistry*, *2021*, 1-12. https://doi.org/10.1155/2021/9985604

Traughber, C. A., Opoku, E., Brubaker, G., Major, J., Lu, H., Lorkowski, S. W., Neumann, C., Hardaway, A., Chung, Y.-M., Gulshan, K., Sharifi, N., Brown, J. M., & Smith, J. D. (2020). Uptake of high-density lipoprotein by scavenger receptor class B type 1 is associated with prostate cancer proliferation and tumor progression in mice. *Journal of Biological Chemistry*, *295*(24), 8252-8261. https://doi.org/https://doi.org/10.1074/jbc.RA120.013694

TréGuier, M., Doucet, C., Moreau, M., Dachet, C., Thillet, J. L., Chapman, M. J., & Huby, T. (2004). Transcription Factor Sterol Regulatory Element Binding Protein 2 Regulates Scavenger Receptor Cla-1 Gene Expression. *Arteriosclerosis, Thrombosis, and Vascular Biology*, *24*(12), 2358-2364. https://doi.org/10.1161/01.atv.0000147896.69299.85

Ueda, T., Bruchovsky, N., & Sadar, M. D. (2002). Activation of the Androgen Receptor N-terminal Domain by Interleukin-6 via MAPK and STAT3 Signal Transduction Pathways. *Journal of Biological Chemistry*, *277*(9), 7076-7085. https://doi.org/10.1074/jbc.m108255200

Unni, E., Sun, S., Nan, B., McPhaul, M. J., Cheskis, B., Mancini, M. A., & Marcelli, M. (2004). Changes in Androgen Receptor Nongenotropic Signaling Correlate with Transition of LNCaP Cells to Androgen Independence. *Cancer Research*, *64*(19), 7156-7168. https://doi.org/10.1158/0008-5472.can-04-1121

Wang, Y., Xia, Z., Xu, J.-R., Wang, Y.-X., Hou, L.-N., Qiu, Y., & Chen, H.-Z. (2012). α-Mangostin, a polyphenolic xanthone derivative from mangosteen, attenuates β-amyloid oligomers-induced neurotoxicity by inhibiting amyloid aggregation. *Neuropharmacology*, *62*(2), 871-881. https://doi.org/10.1016/j.neuropharm.2011.09.016

Wathoni, N., Rusdin, A., Motoyama, K., Joni, I. M., Lesmana, R., & Muchtaridi, M. (2020). Nanoparticle Drug Delivery Systems for α-Mangostin . *Nanotechnology, Science and Applications*, *Volume 13*, 23-36. https://doi.org/10.2147/nsa.s243017

Weir, H. K., Thompson, T. D., Stewart, S. L., & White, M. C. (2021). Cancer Incidence Projections in the United States Between 2015 and 2050. *Preventing Chronic Disease*, *18*, E59. https://doi.org/10.5888/pcd18.210006

Wen, Y., Hu, M. C., Makino, K., Spohn, B., Bartholomeusz, G., Yan, D. H., & Hung, M. C. (2000). HER-2/neu promotes androgen-independent survival and growth of prostate cancer cells through the Akt pathway. *Cancer Res*, *60*(24), 6841-6845.

Wilhelm, S., Tavares, A. J., Dai, Q., Ohta, S., Audet, J., Dvorak, H. F., & Chan, W. C. W. (2016). Analysis of nanoparticle delivery to tumours. *Nature Reviews Materials*, *1*(5), 16014. https://doi.org/10.1038/natrevmats.2016.14

Williams, P., Ongsakul, M., Proudfoot, J., Croft, K., & Beilin, L. (1995). Mangostin Inhibits the Oxidative Modification of Human Low Density Lipoprotein. *Free Radical Research*, *23*(2), 175-184. https://doi.org/10.3109/10715769509064030

Wolfbeis, O. S. (2015). An overview of nanoparticles commonly used in fluorescent bioimaging. *Chemical Society Reviews*, *44*(14), 4743-4768. https://doi.org/10.1039/c4cs00392f

Wolny-Rokicka, E., Tukiendorf, A., Wydmański, J., Ostrowska, M., & Zembroń-Łacny, A. (2019). Lipid Status During Combined Treatment in Prostate Cancer Patients. *American Journal of Men's Health*, *13*(5), 155798831987648. https://doi.org/10.1177/1557988319876488

Wu, Y., Chhipa, R. R., Cheng, J., Zhang, H., Mohler, J. L., & Ip, C. (2010). Androgen receptor-mTOR crosstalk is regulated by testosterone availability: implication for prostate cancer cell survival. *Anticancer Research*, *30*(10), 3895-3901. https://pubmed.ncbi.nlm.nih.gov/21036700

https://www.ncbi.nlm.nih.gov/pmc/articles/PMC4355915/

Xie, Z., Sintara, M., Chang, T., & Ou, B. (2015). Daily consumption of a mangosteen-based drink improves in vivo antioxidant and anti-inflammatory biomarkers in healthy adults: a randomized, double-blind, placebo-controlled clinical trial. *Food Science & Nutrition*, *3*(4), 342-348. https://doi.org/10.1002/fsn3.225

Xu, L., Wang, X., Liu, Y., Yang, G., Falconer, R. J., & Zhao, C.-X. (2022). Lipid Nanoparticles for Drug Delivery. *Advanced NanoBiomed Research*, *2*(2), 2100109. https://doi.org/10.1002/anbr.202100109

Xu, Q., Ma, J., Lei, J., Duan, W., Sheng, L., Chen, X., Hu, A., Wang, Z., Wu, Z., Wu, E., Ma, Q., & Li, X. (2014). α-Mangostin suppresses the viability and epithelial-mesenchymal transition of pancreatic cancer cells by downregulating the PI3K/Akt pathway. *BioMed research international*, *2014*, 546353-546353. https://doi.org/10.1155/2014/546353

Yadav, S., Anbalagan, M., Baddoo, M., Chellamuthu, V. K., Mukhopadhyay, S., Woods, C., Jiang, W., Moroz, K., Flemington, E. K., & Makridakis, N. (2020). Somatic mutations in the DNA repairome in prostate cancers in African Americans and Caucasians. *Oncogene*, *39*(21), 4299-4311. https://doi.org/10.1038/s41388-020-1280-x

Yang, L., Xie, S., Jamaluddin, M. S., Altuwaijri, S., Ni, J., Kim, E., Chen, Y.-T., Hu, Y.-C., Wang, L., Chuang, K.-H., Wu, C.-T., & Chang, C. (2005). Induction of Androgen Receptor Expression by Phosphatidylinositol 3-Kinase/Akt Downstream Substrate, FOXO3a, and Their Roles in Apoptosis of LNCaP Prostate Cancer Cells. *Journal of Biological Chemistry*, *280*(39), 33558-33565. https://doi.org/10.1074/jbc.m504461200

Yates, P., & Stout, G. H. (1958). The Structure of Mangostin1. *Journal of the American Chemical Society*, *80*(7), 1691-1700. https://doi.org/10.1021/ja01540a046

Yeap, S. P., Lim, J., Ngang, H. P., Ooi, B. S., & Ahmad, A. L. (2018). Role of Particle–Particle Interaction Towards Effective Interpretation of Z-Average and Particle Size Distributions from Dynamic Light Scattering (DLS) Analysis. *Journal of Nanoscience and Nanotechnology*, *18*(10), 6957-6964. https://doi.org/10.1166/jnn.2018.15458

Young, J. M., Muscatello, D. J., & Ward, J. E. (2000). Are men with lower urinary tract symptoms at increased risk of prostate cancer? A systematic review and critique of the available evidence. *BJU International*, *85*(9), 1037-1048. https://doi.org/10.1046/j.1464-410x.2000.00659.x

Zacho, H. D., & Petersen, L. J. (2018). Bone Flare to Androgen Deprivation Therapy in Metastatic, Hormone-Sensitive Prostate Cancer on 68Ga-Prostate-Specific Membrane Antigen PET/CT. *Clin Nucl Med*, *43*(11), e404-e406. https://doi.org/10.1097/rlu.0000000000002273

Zhang, H., Li, X.-X., Yang, Y., Zhang, Y., Wang, H.-Y., & Zheng, X. F. S. (2018). Significance and mechanism of androgen receptor overexpression and androgen receptor/mechanistic target of rapamycin cross-talk in hepatocellular carcinoma. *Hepatology*, *67*(6), 2271-2286. https://doi.org/10.1002/hep.29715

Zhao, C., & Dahlman-Wright, K. (2010). Liver X receptor in cholesterol metabolism. *Journal of Endocrinology*, *204*(3), 233-240. https://doi.org/10.1677/joe-09-0271

Zhao, Y., Tang, G., Tang, Q., Zhang, J., Hou, Y., Cai, E., Liu, S., Lei, D., Zhang, L., & Wang, S. (2016). A Method of Effectively Improved α-Mangostin Bioavailability. *European Journal of Drug Metabolism and Pharmacokinetics*, *41*(5), 605-613. https://doi.org/10.1007/s13318-015-0283-4

Zhou, J., Liu, B., Geng, G., & Wu, J. H. (2010). Study of the impact of the T877A mutation on ligand-induced helix-12 positioning of the androgen receptor resulted in design and synthesis of novel antiandrogens. *Proteins: Structure, Function, and Bioinformatics*, *78*(3), 623-637. https://doi.org/10.1002/prot.22592

Zhou, M. (2018). High-grade prostatic intraepithelial neoplasia, PIN-like carcinoma, ductal carcinoma, and intraductal carcinoma of the prostate. *Modern Pathology*, *31*(S1), 71-79. https://doi.org/10.1038/modpathol.2017.138

Zhou, X., Chen, H., Wei, F., Zhao, Q., Su, Q., Lei, Y., Yin, M., Tian, X., Liu, Z., Yu, B., Bai, C., He, X., & Huang, Z. (2020). α-mangostin attenuates pristane-induced lupus nephritis by regulating Th17 differentiation. *International Journal of Rheumatic Diseases*, *23*(1), 74-83. https://doi.org/10.1111/1756-185x.13743

Zhu, X., Li, J., Ning, H., Yuan, Z., Zhong, Y., Wu, S., & Zeng, J.-Z. (2021). α-Mangostin Induces Apoptosis and Inhibits Metastasis of Breast Cancer Cells via Regulating RXRα-AKT Signaling Pathway [Original Research]. *Frontiers in Pharmacology*, *12*. https://doi.org/10.3389/fphar.2021.739658